

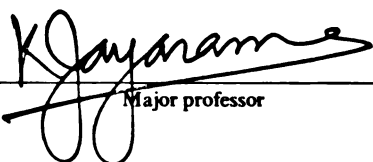
This is to certify that the
dissertation entitled
TWO-PHASE FLOW OF GAS BUBBLE SUSPENSIONS
IN POLYMER LIQUIDS

presented by

Kai Sun

has been accepted towards fulfillment
of the requirements for

Ph.D. degree in Chemical Engineering


Major professor

Date Feb. 16, 1983



RETURNING MATERIALS:
Place in book drop to
remove this checkout from
your record. FINES will
be charged if book is
returned after the date
stamped below.

--	--	--

TWO-PHASE FLOW OF GAS BUBBLE
SUSPENSIONS IN POLYMER LIQUIDS

BY
KAI SUN
A DISSERTATION

Submitted to
Michigan State University
in partial fulfillment of the requirements
for the degree of
DOCTOR OF PHILOSOPHY

Department of Chemical Engineering

1982

ABSTRACT

TWO-PHASE FLOW OF GAS BUBBLE SUSPENSIONS IN POLYMER LIQUIDS

By

Kai Sun

This study was undertaken to explain observed trends in apparent viscosity of gas bubble suspensions with viscoelastic media flowing through a duct. Experiments were run to study the two-phase structure developing in slow, isothermal flow of such suspensions in aqueous Separan solutions as well as a Newtonian corn syrup (as reference). Bubble growth is negligible under conditions of these experiments and the residence time is much smaller than the characteristic time for bubble rise. The variation of bubble volume fraction across a narrow gap between two plates, is recorded at two locations along the flow direction. This is done with a Cesium gamma radiation source focused on a region of area 0.012 cm^2 in the flow plane, and a Sodium iodide detector across the channel yielding a resolution of 0.01 over the range of void fraction investigated from 0.02 to 0.08. This measurement allows us to identify conditions which the flow may be described by a two phase model with a uniform bubbly core and a bubble free wall layer. A theoretical third order suspension model was derived for describing the bulk stress of a dilute homogeneous suspension inside the core region, using a second order model for the viscoelastic

medium. The bulk viscosity thus derived for the suspension has a shear-thinning factor which is related to the elasticity of the medium. Using this third order suspension model, in addition to data on core thickness, bubble concentration profile in the two-phase flow structure, the apparent viscosity can be computed. Such calculations indicate that the observed reduction in apparent viscosity for the two-phase flow may be attributed to a bubbly core which is more shear-thinning than the medium. This two-phase model predicts that the apparent viscosity decreases with increasing wall shear stress and with increasing bulk void fraction consistent with experimental observations.

To my parents
Ping Chang Sun
Y. H. Wong Sun
and
To my wife, Kathleen

ACKNOWLEDGMENTS

I would like to express my sincerely gratitude and appreciation to Dr. Krishnamurthy Jayaraman for his guidance and inspiration throughout the course of this work. I want to thank:

Dr. Bruce W. Wilkinson for his assistance with the gamma radiation gauge set-up.

Mr. Donald Child for his valuable suggestion on experimental design and construction.

Professors Charles A. Petty, Robert W. Little and Chang-Yi Wang for many helpful discussions.

Mr. Ekong A. Ekong and Ms. Eden Tan Dionne for their assistance in the experiment.

This work was supported in part by NSF Grant No. CP-8110752 and by the Division of Engineering Research of Michigan State University.

Lastly, I thank my parents for their encouragement and my wife for her patience and understanding.

TABLE OF CONTENTS

LIST OF TABLES.....	vi
LIST OF FIGURES.....	vii
NOMENCLATURE.....	xi

Chapter

1	INTRODUCTION.....	1
	1.A Dynamics of Bubble Growth	
	1.B Particle Motion in Viscoelastic Liquids	
	1.C Apparent Viscosity of Polymer Foams in Poiseuille Flow	
	1.D Suspension Rheology	
2	PROBLEM STATEMENT.....	23
	2.A Problem Statement.	
	2.B Flow Structure and Apparent Viscosity	
	2.C Objectives	
3	EXPERIMENTAL ARRANGEMENT AND MATERIALS.....	29
	3.A Apparatus	
	3.B Materials	
4	RADIATION GAUGE.....	59
	4.A Principles of Gamma Attenuation	
	4.B Instruments of Radiation Gauge	
5	VOID FRACTION PROFILES IN VISCOELASTIC FLUIDS...	82
	5.A Profiles in Corn Syrup	
	5.B Profiles in 2.5 wt Percent Separan Solution.	
	5.C Profiles in 3.5 wt Percent Separan Solution	
	5.D Correlation of Two-Phase Structure with Medium Properties	

Chapter

6	BULK RHEOLOGY OF DILUTE SUSPENSIONS IN VISCOELASTIC LIQUIDS.....	125
6.A	Introduction	
6.B	Microrheology	
6.C	Bulk Stress	
6.D	Third Order Model For Suspension	
6.E	Discussion	
7	PREDICTION OF APPARENT VISCOSITY IN TWO-PHASE FLOW.....	149
7.A	Third Order Suspension Model	
7.B	Power Law Suspension Model	
8	CONCLUSIONS AND RECOMMENDATION.....	156
8.A	Conclusion	
8.B	Recommendations	

APPENDICES

Appendix

A	SYMMETRY OF VOID FRACTION PROFILE WITH RESPECT TO FLOW AXIS.....	162
B	DATA ANALYSIS OF VOID FRACTION PROFILES.....	153
C	FLOW FIELD OF A SPHERICAL, NEWTONIAN DROP IN A SECOND ORDER FLUID.....	165
D	EVALUATION OF EXTRA STRESS TENSORS.....	170
E	COMPUTER PROGRAMS FOR RELATIVE VISCOSITY COMPUTATION.....	175

REFERENCES.....	179
-----------------	-----

LIST OF TABLES

Table		Page
3.1	PROPERTIES OF MEDIA.....	38
5.1	COMPARISON OF VOID FRACTION PROFILES.....	122

LIST OF FIGURES

Figure	Page
1.1 Schematic of Particle in Poiseuille Flow.....	12
1.2 Observed Trends of Apparent Viscosity.....	17
2.1 Two-Phase Flow Structure.....	25
3.1 Schematic of Flow Arrangement.....	30
3.2 Static Mixer.....	34
3.3 Transition Channel and Rectangular Channel.....	35
3.4 Viscosity of Corn Syrup.....	41
3.5 Viscosity and Primary Normal Stress Coefficient of 2.5 wt Percent Aqueous Separan Solution.....	42
3.6 Viscosity and Primary Normal Stress Coefficient of 3.5 wt Percent Aqueous Separan Solution.....	43
3.7 Sensitivity of Pressure Transducer.....	48
3.8 Photograph of Flowing Suspension at Entrance, 5 min. after startup.....	51
3.9 Photograph of Flowing Suspension at Entrance, 20 min. after startup.....	52
3.10 Photograph of Flowing Suspension at End of Channel, 5 min. after startup.....	53
3.11 Photograph of Flowing Suspension at End of Channel, 20 min. after startup.....	54
4.1 Schematic of Linear Attenuation Technique.....	62
4.2 Cesium Capsule.....	66
4.3 Calibration Curve for Radiation Counter.....	70

Figure		Page
4.4	Radiation Gauge Mounting.....	72
4.5	Linear Mass Attenuation Coefficients.....	75
4.6	Experimental Calibration for the Resolution of Radiation Gauge.....	79
5.1	Void Fraction Profile with Corn Syrup $\phi_b=.018$, $\langle V \rangle =.65$ cm/sec	85
5.2	Void Fraction Profile with Corn Syrup $\phi_b=.024$, $\langle V \rangle =.54$ cm/sec	86
5.3	Void Fraction Profile with Corn Syrup $\phi_b=.025$, $\langle V \rangle =.46$ cm/sec	87
5.4	Void Fraction Profile with Corn Syrup $\phi_b=.033$, $\langle V \rangle =.88$ cm/sec	88
5.5	Void Fraction Profile with Corn Syrup $\phi_b=.034$, $\langle V \rangle =.74$ cm/sec	89
5.6	Void Fraction Profile with Corn Syrup $\phi_b=.036$, $\langle V \rangle =.59$ cm/sec	90
5.7	Void Fraction Profile with Corn Syrup $\phi_b=.042$, $\langle V \rangle =.39$ cm/sec	91
5.8	Void Fraction Profile with Corn Syrup $\phi_b=.051$, $\langle V \rangle =.62$ cm/sec	92
5.9	Void Fraction Profile with Corn Syrup $\phi_b=.058$, $\langle V \rangle =.77$ cm/sec	93
5.10	Void Fraction Profile with 2.5 wt Percent Separan Solution, $\phi_b=.018$, $\langle V \rangle =.7$ cm/sec	95
5.11	Void Fraction Profile with 2.5 wt Percent Separan Solution, $\phi_b=.02$, $\langle V \rangle =.82$ cm/sec	96
5.12	Void Fraction Profile with 2.5 wt Percent Separan Solution, $\phi_b=.022$, $\langle V \rangle =.4$ cm/sec	97
5.13	Void Fraction Profile with 2.5 wt Percent Separan Solution, $\phi_b=.024$, $\langle V \rangle =.58$ cm/sec	98

Figure		Page
5.14	Void Fraction Profile with 2.5 wt Percent Separan Solution, $\phi_b=.025$, $\langle V \rangle=.54$ cm/sec	99
5.15	Void Fraction Profile with 2.5 wt Percent Separan Solution, $\phi_b=.032$, $\langle V \rangle=.78$ cm/sec	100
5.16	Void Fraction Profile with 2.5 wt Percent Separan Solution, $\phi_b=.032$, $\langle V \rangle=1.17$ cm/sec	101
5.17	Void Fraction Profile with 2.5 wt Percent Separan Solution, $\phi_b=.031$, $\langle V \rangle=1.18$ cm/sec	102
5.18	Void Fraction Profile with 2.5 wt Percent Separan Solution, $\phi_b=.034$, $\langle V \rangle=.81$ cm/sec	103
5.19	Void Fraction Profile with 2.5 wt Percent Separan Solution, $\phi_b=.035$, $\langle V \rangle=.6$ cm/sec	104
5.20	Void Fraction Profile with 2.5 wt Percent Separan Solution, $\phi_b=.077$, $\langle V \rangle=1.38$ cm/sec	105
5.21	Void Fraction Profile with 3.5 wt Percent Separan Solution, $\phi_b=.026$, $\langle V \rangle=.93$ cm/sec	108
5.22	Void Fraction Profile with 3.5 wt Percent Separan Solution, $\phi_b=.032$, $\langle V \rangle=.32$ cm/sec	109
5.23	Void Fraction Profile with 3.5 wt Percent Separan Solution, $\phi_b=.035$, $\langle V \rangle=.91$ cm/sec	110
5.24	Void Fraction Profile with 3.5 wt Percent Separan Solution, $\phi_b=.035$, $\langle V \rangle=1.5$ cm/sec	111
5.25	Void Fraction Profile with 3.5 wt Percent Separan Solution, $\phi_b=.04$, $\langle V \rangle=.82$ cm/sec	112
5.26	Void Fraction Profile with 3.5 wt Percent Separan Solution, $\phi_b=.043$, $\langle V \rangle=1.29$ cm/sec	113

Figure		Page
5.27	Void Fraction Profile with 3.5 wt Percent Separan Solution, $\phi_b=.045$, $\langle V \rangle=.71$ cm/sec	114
5.28	Void Fraction Profile with 3.5 wt Percent Separan Solution, $\phi_b=.049$, $\langle V \rangle=.5$ cm/sec	115
5.29	Void Fraction Profile with 3.5 wt Percent Separan Solution, $\phi_b=.05$, $\langle V \rangle=.4$ cm/sec	116
5.30	Void Fraction Profile with 3.5 wt Percent Separan Solution, $\phi_b=.05$, $\langle V \rangle=1.18$ cm/sec	117
5.31	Void Fraction Profile with 3.5 wt Percent Separan Solution, $\phi_b=.056$, $\langle V \rangle=.73$ cm/sec	118
5.32	Void Fraction Profile with 3.5 wt Percent Separan Solution, $\phi_b=.057$, $\langle V \rangle=.65$ cm/sec	119
6.1	Characteristic Dimension of Dilute Suspension in Simple Steady Shear.....	132
6.2	Relative Viscosity vs Shear Rate for Rigid Sphere Suspensions, $\phi=.02$	142
6.3	Relative Viscosity vs Shear Rate for Rigid Sphere Suspensions, $\phi=.05$	143
6.4	Relative Viscosity vs Shear Rate for Rigid Sphere Suspensions, $\phi=.07$	144
6.5	Relative Viscosity vs Shear Rate for Rigid Sphere Suspensions, $\phi=.1$	145
6.6	Relative Normal Stress Coefficient vs Volume Fraction for Rigid Sphere Suspensions in SCMC..	147
7.1	Apparent Viscosity Ratio vs Wall Shear Stress	152
7.2	Apparent Viscosity Ratio vs Volume Fraction	155

NOMENCLATURE

A	atomic mass number g/g-atom
$\underline{A}_1, \underline{A}_2$	dimensionless Rivlin-Erickson tensors of exterior fluid
a	bubble (or drop) radius, cm
B	number density of bubbles
b	parameter in equation (7.19)
b_{11}, b_{22}, b_{33}	normal stress components function of κ and ϵ , (equation (6.44))
C_i, C_i'	functions of ϵ , defined in Appendix C
d	interparticle distance
F	shear-thinning factor, function of κ and ϵ , (equation (6.44))
\tilde{F}_n	n th order hydrodynamic force
G	bulk rate of shear strain, sec^{-1}
g	acceleration due to gravity, cm/sec^2
H	length scale (over which suspension is undergoing a simple shear flow)
h	gap height, cm
I	radiation intensity
\underline{I}	unit tensor
\underline{J}_1	summation of surface integrals in equation
\underline{J}_2	summation of volume integrals in equation
K	power law parameter
$\underline{L}_1, \underline{L}_2$	Rivlin-Erickson tensors
l	linear dimension of an element volume V

m	parameter in equation (7.19)
No	Avagadro's number, atoms/g-atom
N	number of drops in an element volume V
N_1, N_2	primary and secondary normal stress difference, dyne/cm ²
\hat{n}	unit vector in the r direction
P	dimensional pressure
p	dimensionless pressure
Q	number of radiation counts
q	isotropic pressure
Re	Reynolds number, $\rho \langle v \rangle h / \eta$
Rep	particle Reynolds number, $\rho \langle v \rangle a / \eta$
\vec{r}	position vector
S	surface of single drop
S	recoverable shear ration, $N_1 / 2\tau$
T_n	nth order hydrodynamic torque
\underline{T}	bulk stress tensor
\underline{T}_E	extra stress tensor
\underline{t}	non-Newtonian part of stress tensor
tr	bubble rise time, sec
t	thickness, cm
\vec{U}	dimensional velocity vector
\vec{u}	dimensionless velocity vector
V	element volume
Vo	volume of single drop
v	axial velocity, cm/sec
W	channel width, cm

We	Weissenberg number, N_1/τ
w	width of channel wall, cm

Greek Letters

α	velocity gradient of simple shear flow
β	linear attenuation coefficient, cm^3/g
$\dot{\gamma}$	shear rate
ϵ	material parameter, $(\psi_{10} + \psi_{20})/\eta_0$
ζ	microscopic absorption cross section, cm^2/atom
η	viscosity, poise
θ	mass attenuation coefficient
κ	viscosity ratio of interior fluid to exterior fluid
λ	material parameter, $-\psi_{10}/2(\psi_{10} + \psi_{20})$
μ	linear absorption coefficient, cm^{-1}
ξ	ratio of inlet pressure and outlet pressure
Π	dimensionless stress tensor
ρ	density, g/cc
σ	surface tension, dynes/cm
$\underline{\sigma}$	stress tensor
$\underline{\tau}$	shear stress, $\text{dyne}^5/\text{cm}^2$
ϕ	volume fraction
ψ_1, ψ_2	primary and secondary normal stress coefficients of suspension, $\text{dyne-sec}^2/\text{cm}^2$
ψ_{10}, ψ_{20}	primary and secondary normal stress coefficients of medium fluid, $\text{dyne-sec}^2/\text{cm}^2$
Δc	bubble core thickness, cm
$d\Omega$	directed element of surface area

Subscripts

a	apparent
b	bulk
c	core
g	gas phase
i	initial value
l	liquid phase
r	reference
s	suspension
w	wall
0	zero-shear rate value or zeroth order terms (associate with tensor notations)
1	first order terms (associate with tensor notations)
10	zeroth order of Rivlin-Erickson tensor \underline{A}_1
11	first order of Rivlin-Erickson tensor \underline{A}_1
20	zeroth order of Rivlin-Erickson tensor \underline{A}_2
21	first order of Rivlin-Erickson tensor \underline{A}_2
∞	value at infinity

Superscripts

'	interior (of drop) quantities
T	transpose
~	fluctuation quantities

Miscellaneous Symbols

D/bt	material time derivative
∇	nabla operator
∇^2	Laplace operator

Miscellaneous Symbols

tr	trace
.	dot product
:	double dot product
x	cross product
O	order symbol
< >	average quantities

CHAPTER 1

INTRODUCTION

The rheology of filled polymer materials has become a subject of considerable scientific and technical interest because of the growing use of composite materials. Gas bubbles, fibers and rigid particles are added to polymer melts or polymer solutions to reduce the production cost, to reinforce the material strength or to facilitate material transport. Among filled polymer systems, polymer foams particularly exhibit unusual rheological behavior, such as a relative viscosity less than one even at low gas bubble concentrations and a yield stress at moderate concentrations. Polymer foams, suspension of gas bubbles in a polymer matrix, are commonly produced in thermoplastic extrusion, injection molding and polymer devolatilization processes. The gas may be injected directly into polymer melt in the extruder or it may be generated by decomposition of a chemical compound ("blowing agent") introduced into the polymer before extrusion. In polymer devolatilization, releasing the pressure on molten polymer containing dissolved monomer produces foams with five to ten percent by volume of monomer gas bubbles. The foam quality is determined by the distribution of bubbles ("closed cells") in the polymer. This is obviously affected by any crossflow migration of bubbles in flow of these suspensions. Furthermore, control of these

processes requires some knowledge of foam viscosity. The cell size and structure are functions of rheological properties of the polymer. With too high a polymer viscoelasticity, the bubbles are not able to grow and the optimum yield of gas is not achieved. On the other hand, if the polymer viscosity is too low, the bubbles will burst and leading to open cells.

The measurement of foam viscosity must be done in flow through a closed conduit, which is generally complicated by several factors, such as bubble rise, growth and migration transverse to the flow. Usually bubble migration proceeds much faster than the other two processes leading to a nonuniform suspension. The inhomogeneity of bubble concentration in the flow makes it even more complicated to predict the flow behavior. Bubble growth, bubble migration and bubble rise are all associated with the rheological properties of medium fluid and bubbles. To have a fundamental understanding of foam flow in viscoelastic liquids, we start with a study of dilute suspensions, where bubble interactions are not significant, and the modeling is less difficult. The study of dilute polymer foams is of significance for polymer devolatilization processes where monomer trapped in polymer during emulsion polymerization is removed by extrusion of the polymer melt into a vacuum. In general, the subject of bubbly suspension flow in non-Newtonian media involves three

areas - the dynamics of bubble growth, particle migration in non-Newtonian fluid and suspension rheology.

1.A Dynamics of Bubble Growth

Bubble growth upon pressure release is governed by the diffusivity and solubility of gas in the polymer and by the resultant pressure difference, interfacial tension and hydrodynamic resistance. Numerous theoretical studies have been reported on the growth or collapse of spherical bubble in inviscid, viscous and viscoelastic fluids. Street et al. (1971) investigate the bubble growth in a power law fluid associated with simultaneous momentum, mass and heat transfer with the assumption that gas concentration gradient is appreciable only in a thin film next to the bubble. The bubble growth rate is controlled by the diffusivity and concentration of blowing agent, viscosity and the extent of shear-thinning. With higher shear-thinning fluids, a higher initial growth rate is obtained. Yang and Yeh (1972) studied the heat-induced collapse of a spherical bubble in incompressible Power law and Bingham fluids. Their numerical solutions show that in the Bingham fluids, a decrease in the yield stress results in an increase in the collapse rate; a decrease in power law index n results in an increase in the collapse rate for power law fluids.

Bubble growth in a viscoelastic fluid was first studied theoretically by Street (1968), using an Oldroyd fluid

model, in which the fluid stress on the bubble surface is determined by the history of rate of strain. The driving force in this analysis is the pressure difference between the exterior and interior of gas bubble; diffusion effect and heat conduction are not included. The bubble growth rate predicted is faster initially and then slower compared to that in a Newtonian fluid, thus medium elasticity has a significant influence on the growth rate. In addition, Fogler and Goddard (1970) considered inertia effects on collapse of a bubble in a Maxwellian fluid at moderate and high Reynolds numbers. In a fluid with large relaxation times, they showed that bubble may either collapse or undergo oscillation about an equilibrium radius. Its conduct depends on whether the ratio of ambient pressure to the elastic modulus of Maxwellian fluid exceeds a critical value or not. The bubble collapse process in a fluid with moderate relaxation time experiences the same oscillation but only over a short period of time. At low Reynolds numbers, the viscous force dominates the elastic effect, the collapse rate becomes critically damped, and no oscillation is observed. Zana and Leal (1975) incorporated mass transfer into their study on diffusion-induced collapse of a bubble in an Oldroyd B type fluid, and examined in detail the roles of viscosity, relaxation time, retardation time, surface tension and Henry's law constant. The bubble collapse rate is significantly influenced by the viscosity - an order of

magnitude change in viscosity may triple the collapse rate. The introduction of fluid relaxation and retardation times causes the bubble collapse rate to initially overshoot its corresponding steady state value and then approaches a slower rate later. As the bubble becomes smaller, interfacial tension functions as an additional driving force besides pressure difference, therefore, it enhances the collapse rate. Experimentally, Zana and Leal (1978) investigated the dissolution of carbon dioxide gas bubble in four aqueous Separan solutions. The mass transfer rate was significantly enhanced as a result of viscoelasticity. Pearson and Middleman (1977, 1978) observed isothermal bubble collapse in polymer solutions to study the elongational rheology of viscoelastic liquids of moderate viscosity and high strain rate. Prud'homme and Bird (1977) derived dilatational properties of suspensions of gas bubbles in Newtonian fluid, second order fluid and Goddard-Miller fluid by comparing the equivalent stresses at boundaries of a compressible cell and a second cell containing a dilating bubble. They showed that dilatational properties can be determined from the rheological properties of continuous phase and volume fraction of gas phase.

1.B Particle Motions in Non-Newtonian Fluids

Bubble migration in non-Newtonian fluids may result from the gradient of normal stresses around the bubble,

inertia, deformation of bubble and hydrodynamic interactions between bubbles and boundaries. The elasticity of polymers plays a principal role among all the factors, in bubble migration and bubble rise in the non-Newtonian fluids. Particle motion in elastic fluids have been investigated, taking into account inertia effect (Caswell and Schwarz (1962)), wall effect Caswell (1962, 1970)), and far field hydrodynamic interaction between particles (Caswell (1977), Brunn (1977)). In general, the particle dynamics are solved by a regular perturbation expansion in the Weissenberg number starting with known results from a Newtonian medium. Nevertheless, this analytical approach is useful in determining the first order or second order correction due to elasticity if the medium fluid is represented by a so called Rivlin and Ericksen expansion (1955) or order fluids. The stress relation of these order fluids is given by:

$$\begin{aligned} \underline{T} = & \alpha_0 \underline{A}_1 + \alpha_1 \underline{A}_2 + \alpha_2 \underline{A}_1^2 + \alpha_3 \underline{A}_3 + \alpha_4 (\underline{A}_1 \cdot \underline{A}_2 + \underline{A}_2 \cdot \underline{A}_1) \\ & + \alpha_5 (\text{tr } \underline{A}_1^2) \underline{A}_1 + \text{higher terms} \end{aligned} \quad (1.1)$$

where the Rivlin-Ericksen tensors \underline{A}_n are defined by

$$\underline{A}_1 = \nabla \underline{U} + \nabla \underline{U}^T \quad (1.2)$$

$$\underline{A}_n = \frac{D \underline{A}_{n-1}}{D t} + \underline{A}_{n-1} \cdot \nabla \underline{U} + \nabla \underline{U}^T \cdot \underline{A}_{n-1} \quad (1.3)$$

For a simple shear flow, it can be shown that

$$\underline{A_n} = 0 \quad \text{for } n > 2 \quad (1.4)$$

and the three material functions can be related to α_i by

$$\tau_{12}(\dot{\gamma}) = (\alpha_0 + 2\alpha_5 \dot{\gamma}^2) \dot{\gamma} \quad (1.5)$$

$$N_1(\dot{\gamma}) = \tau_{11} - \tau_{22} = (2\alpha_2 + \alpha_1) \dot{\gamma}^2 \quad (1.6)$$

$$N_2(\dot{\gamma}) = \tau_{11} - \tau_{33} = \alpha_2 \dot{\gamma}^2 \quad (1.7)$$

there τ is the stress function, N_1, N_2 are normal stress functions of shear rate $\dot{\gamma}$ with flow direction denoted by 1 and the direction of velocity gradient denoted by 2. The Rivlin-Ericksen model is a polynomial expansion in velocity gradient so that the perturbation method can be applied to solve steady flow (rheologically slow flow) problems. The dashed-underlined terms, quadratic in the velocity gradients are referred to as the second order fluid model. The material functions in this model are invariant with strain rate. With all the terms that are cubic in the velocity gradient included, the relation is referred to as third order fluid model. This model is better in that it may be used to represent a shear-thinning fluid, with some elasticity. In general, these order fluids are not suitable for computations involving unsteady flow. The study of particle motion in non-Newtonian fluids can be discussed in two areas - unbounded and bounded flow.

Unbounded Flow

A study of the deviation from Stokes' law due to viscoelasticity in the unbounded quiescent fluid was first reported by Leslie and Tanner (1961) who evaluated the drag force on a sphere in an Oldroyd fluid, and formed the correction to $O(We^2)$. Giesekus (1962) solved for the simultaneous translation and rotation of a rigid sphere in a third order fluid, his result for the drag force is consistent with Leslie's result. Wagner and Slattery (1971) included the effect of inertia and particle deformation on particle shape in the analysis by considering a third order fluid drop in another third order medium. For the motion of a spherical drop in a second order fluid undergoing a steady shear flow, the velocity and pressure fields were derived by Peery (1966).

For particle-particle interaction, the hydrodynamic force and torque have to be solved by Oseen method or Green's function method apart from perturbation expansion. Brunn (1977) employed Oseen far field approximation for the particle-particle interaction in a homogeneous second order fluid to predict the relative orientation of spheres. Caswell (1977) used Green's function method, in which the force can be expressed by a single integral equation which contains information of governing equation and boundary conditions. The integral equation is manipulated and reduced to a series of auxiliary boundary value equations in an infinite domain, the interaction is $O(d^{-2})$, where d is the

distance between particles. For large d , the viscoelasticity induces repulsion or attraction between two spheres depending on the normal stress coefficients. For a slender axisymmetric rod-like particle in a simple shear flow, the non-Newtonian force and torque are evaluated by Leal (1975) using reciprocal theorem of Lorentz which allows the calculation of second order forces from the first order (Stokes) flow field. The force correction is found $O(We)$ rather than $O(We^2)$ as for sphere. The variation appears to be the characteristic of particle lacking of fore-and-aft symmetry. The motion of a slightly deformed sphere in the second order fluid was studied by Brunn (1979) using direct approach of solving the velocity and pressure fields in the fluid of $O(We)$.

Experimentally, Chhabra et al. (1979) employed a Boger fluid to examine the effect of fluid elasticity on the drag coefficient alone. For $0 \leq We \leq 0.1$, no significant deviation from Stoke's law is observed. For $We > .1$, the drag reduces continuously with increasing We and reaches an asymptotic reduction of 26% at $We > 0.7$.

Bounded Flow

The particle motion in the limit of finite boundaries is more important than in the unbounded flow, because all the experimental observations have to be performed in a closed conduit. The most significant case of the wall

effect is the induced particle crossflow migration in the Couette viscometers and in the Poiseuille flows. Caswell (1972) used Green's function method to obtain the first order wall effect, the correction is independent of the particle geometry and its surface boundary condition. Sigli and Coutanceau (1977) conducted experimental investigation of the effect of finite boundaries on a slow laminar isothermal flow of a viscoelastic fluid around a spherical obstacle. The drag reduction is enhanced by the wall effect and becomes even more significant as the elasticity of the fluid increases.

The observation of particle migration was first reported by Segré and Silberberg (1962). They found that rigid spheres in a unidirectional Newtonian flow migrate to an equilibrium position which is about .6 radius away from the wall at moderate Reynolds number. Later, Ho and Leal (1974) showed that in a Newtonian fluid, the occurrence of particle migration is strictly a result of inertia effect. The particle migration in Non-Newtonian fluids was observed by Karnis and Mason (1966), Gauthier et al. (1971 a, b) and Highgate and Whorlow (1969) and their results are summarized below. In the Couette flow of viscoelastic fluid, neutrally buoyant solid spheres migrate toward the cylinder wall but neutrally buoyant Newtonian drops migrate away from the wall to an equilibrium position in between. In the Poiseuille flow of viscoelastic fluids both spheres and drops migrate

away from the wall and settle at the flow axis. However, the particle migration precedes differently in pseudoplastic fluids, i.e. the spheres migrate toward the wall while drops migrate to an intermediate location in between the wall and flow axis in Poiseuille flow. Particle migration is governed by the equation of particle motion and by the reversibility condition of Saffman (1956). The reversibility condition means the particle motion is reversible regardless of time and flow direction. This property can be destroyed in the presence of inertia effect, wall effect, particle shape and normal stress.

Chan and Leal (1979) studied cross flow migration of a deformable second order fluid drop in a Poiseuille flow (Figure 1.1) of another second order fluid with the help of Lorentz reciprocal theorem. To take the bounding walls into account, the method of reflection was used with an asymptotic expansion for $a/h \ll 1$ where h is the gap of flow channel. The dimensional migration velocity for a Newtonian drop was derived as

$$\begin{aligned}
 U_s = & \left(\frac{\psi_1 + \psi_2}{\eta} \right) a^2 \left(\frac{\partial U}{\partial y} \right) \left(\frac{\partial^2 U}{\partial y^2} \right) \frac{1}{315(2+3K)^2(4+K)(1+K)^2} \left\{ (2560 + \right. \\
 & 10932K + 23252K^2 + 24606K^3 + 10995K^4 + 1575K^5) + E_1 \\
 & \left. (5920 + 27588K + 62341K^2 + 70626K^3 + 32940K^4 + 4725K^5) \right\} \\
 & - \frac{a^3 \eta}{0} \left(\frac{\partial U}{\partial y} \right) \left(\frac{\partial^2 U}{\partial y^2} \right) \frac{1}{(1+K)^2(2+3K)} \left\{ \frac{1}{42(2+3K)(4+K)} (13 - 36K \right. \\
 & \left. - 73K^2 - 24K^3) + \frac{10+11K}{105} (8 - K + 3K^2) \right\} \quad (1.8)
 \end{aligned}$$

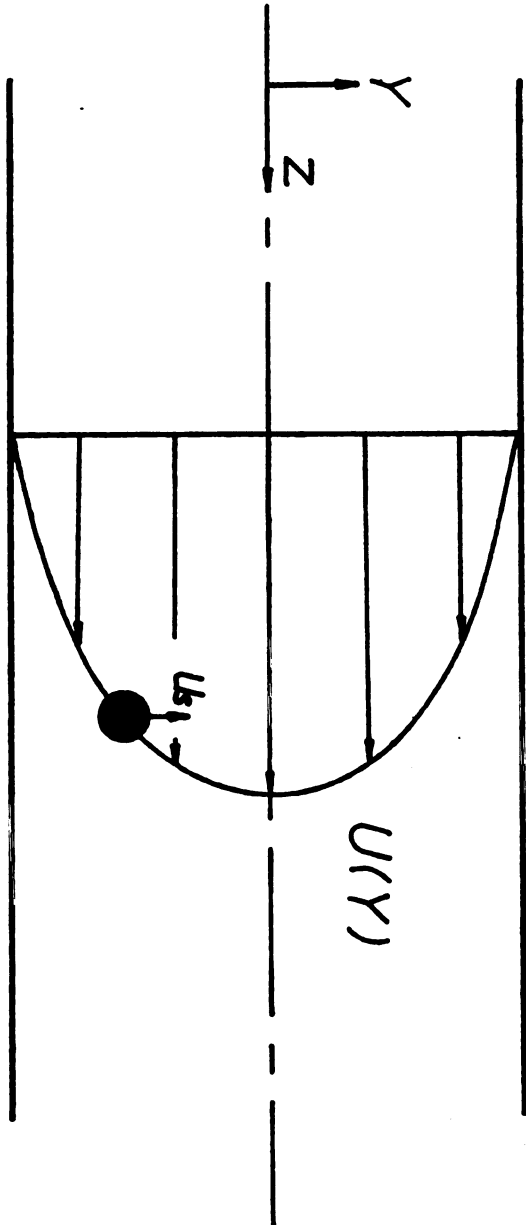


Figure 1.1 Schematic of Particle in Poiseuille Flow

where ψ_1 , ψ_2 are the primary and secondary normal stress coefficients, η is the medium viscosity, ϵ is the ratio of normal stress coefficients $-\psi_1/2(\psi_1+\psi_2)$, κ is the viscosity ratio of component fluids (interior to exterior), and σ is the interfacial tension. The first term in equation (1.8) is the elastic contribution and second term is the contribution due to the particle deformation. For an inviscid and spherical particle ($\kappa \rightarrow 0$), suspended in a second order fluid the migration velocity can be simplified to

$$U_s = - \frac{\sigma^2}{\eta} \left(\frac{\partial U}{\partial y} \right) \left(\frac{\partial^2 U}{\partial y^2} \right) \left[0.508 (\psi_1 + \psi_2) - 0.587 \psi_1 \right] \quad (1.9)$$

Note that the elastic term will be nonzero only if the curvature of the velocity profile — $\partial^2 U / \partial y^2$ is nonzero. Also with the direction shown in Figure 1.1, $\partial^2 U / \partial y^2 > 0$ and $\partial U / \partial y < 0$, so that U_s is toward the negative y direction, which means the particle migrates toward the centerline of the channel. For the two-dimensional Poiseuille flow, the quantitative prediction compares unsatisfactorily with available experimental data (Karnis and Mason (1962), Gauthier, et al.

(1971 a)). The calculated values of the fluid parameters of the same fluid were found to be inconsistent in different studies. This is due to the discrepancy between the second order fluid and strongly viscoelastic fluids used in the experiments. Qualitatively, the migration theory agrees

well with experimental observations. The effects of velocity profile and viscoelasticity on the migration rate and direction can be predicted.

Particle migration may be observed in Couette viscometers, with significant gap to radius ratio, where the velocity profile is nonlinear close to the wall (Highgate and Whorlow (1969, 1970)). Chan and Leal (1981) studied the migration of deformable droplet in such a Couette viscometer and their experimental data agree well with their theoretical calculations. However no theoretical arguments have been proposed to explain migration of particles towards the wall in pseudo-plastic fluids as observed by Gauthier et al. (1971 b). The velocity field in this medium around the sphere is symmetric as determined by the equation of particle motion and so from theories of Chan and Leal (1979), Brunn (1979), no migration should occur. At present it is concluded that the overall effect of shear-thinning on particle migration has not been fully defined.

In practical situations, one encounters multiparticles problems, so the model of single particle migration no longer holds. In the suspension system, our main concern is the void fraction profile rather than single particle motion. The development rate of the profile is related to particle migration. Therefore, we believe that further studies on the profile as a function of medium viscoelastic properties can lead us to a better understanding of two-phase flow structure.

Apparent Viscosity of Suspension in Poiseuille Flow

The flow in the continuous foam extrusion process is a Poiseuille flow which is complicated by several factors as discussed above. Due to the complexity of bubble growth and the nature of flow field inside the die, measurement in Poiseuille flow can no longer be taken as the shear viscosity but an apparent viscosity. The quality of the foam such as cell size, product density is commonly correlated with the apparent viscosity. Bigg and Preston (1976) studied the dependence of rheological properties of polymer foams on temperature, shear rate and their effects on foam density. The apparent viscosity of bubble suspension was less than that of pure polymer solutions and it became more shear-thinning. The critical pressure for initiating bubble growth was reported by Villamizar and Han (1978) in which temperature effect and shear rate effect are included. The axial pressure gradient is found nonlinear, the deviation from linearity being caused by a changing viscosity in the flow attributed to bubbles growth and migration. The morphology of bubble and apparent rheological characteristics of bubble suspensions were studied by Oyanagi and White (1978) and correlated with flow rate, blowing agent, die geometry and temperature. The extrudate swell of foamy polymer was found larger than the polymer melts without bubbles, the swell increasing with shear rate. The apparent viscosity

of polymer melts containing blowing agent is larger than that of polymer melt at low shear rate and increases with decreasing shear rate. As shear rate increases, a reduction in the apparent viscosity was observed, the upturn critical shear rate is a function of temperature and geometry of the die.

Prud'homme (1978) used electrolysis of water on a stainless steel grid located in the flow to generate spherical, hydrogen gas bubbles of 0.2 mm in diameter, up to 6 percent by volume in aqueous solutions of polyacrylamide. He observed the flow of these suspensions through glass tubes 0.635 cm and 0.953 cm in diameter at Reynolds numbers of order 10^{-2} and reported that in range of wall shear stresses between 16 N/m^2 and 32 N/m^2 , the radial distribution of bubbles in the duct was uniform with an increase in bubble concentration leading to lower flow rates. At wall stresses higher than 32 N/m^2 , the bubbles migrated away from the tube wall, and an increase in bubble concentration resulted in higher flow rates or reduction in apparent viscosity (Figure 1.2). However, no theoretical explanation was proposed to correlate these trends. We believe the reduction in the apparent viscosity at higher wall shear stress is associated with the change in the void fraction profile affected by bubble migration. It appears that the viscosity of central bubble rich region decreases which accounts for the reduction in the apparent viscosity.

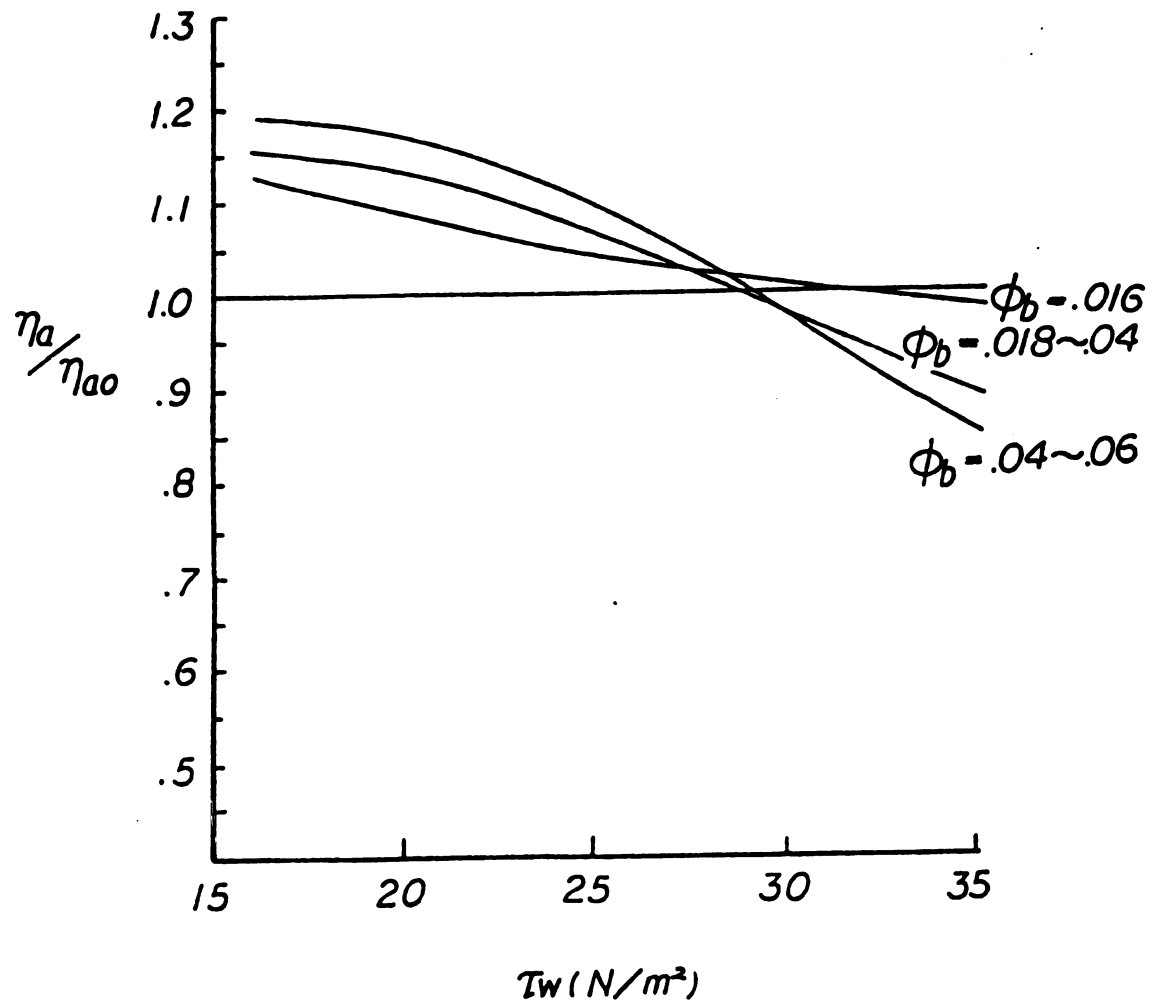


Figure 1.2 Observed Trends of Apparent Viscosity

In the above presentations, the experiments were conducted in such a way that bubble growth, bubble migration are not distinguishable. A more controlled flow experiment was studied by Prud'homme (1978), in which only bubble migration effect was considered.

Suspension Rheology

The rheology of suspensions may be described conveniently wherever possible by treating the suspension as a macroscopically homogeneous mixture with effective bulk properties. These bulk properties are determined by the averages over microrheological parameters with the consideration of particle interactions, particle spatial distribution and particle shape. Any of these factors can change the fluid behavior significantly. Review of Newtonian suspension rheology have been presented by Brenner (1972), Jeffrey and Acrivos (1976) and Schowalter (1978). Particle sizes in polymer foams range from 10^{-3} to 1 cm, therefore, forces other than hydrodynamic are negligible, i.e. Brownian force (Brenner (1967, 1974), electrical force (Russell (1976), Krieger and Eguiluz (1976)) and London-van der Waals forces (Hoffman (1972, 1974))). The bulk properties of suspension are influenced by the nature of particle-shape, elastic, viscous, inertia force, particle interaction. Three models have been proposed for evaluation the bulk stress of suspensions in Newtonian fluids:

(1) volume average method for dilute system (2) cell model

and (3) squeezing film model for concentrated system. The classical Einstein relation (1911) for effective viscosity of very dilute suspension is computed from the additional rate of energy dissipation engaged by the introduction of single sphere into a homogeneous shear flow. The energy dissipation approach is incapable for yielding a complete tensorial bulk stress, but only a scalar relative viscosity. In the dilute suspension, Batchelor (1970) showed that bulk stress can be calculated exactly by using a volume average procedure to relate the microscopic to macroscopic properties in the absence of Brownian motion and particle interactions. By the same token, suspensions were studied by other investigators, Goddard and Miller (1967) and Roscoe (1967) for elastic spheres, Schowalter et al. (1968) for deformable drops, Cox (1969) and Frankel and Acrivos (1970) for time-dependent deformable drops and shearing flow respectively, Batchelor (1971) for slender solid particles, Lin et al. (1970) for solid spheres under the influence of inertia effect. In all cases, the suspension exhibits non-zero normal stresses in the Newtonian medium. The Taylor result of viscosity is unaffected but to slender particles and inertia effect, additional corrections are related to the aspect ratio of particles and Reynolds number respectively. Barthes-Biesel and Acrivos (1973) pointed out that these dilute suspension theories are limited in the sense of

experimental measurement but are of great value of testing for phenomenological equations for non-Newtonian fluids.

Batchelor and Green (1972) took hydrodynamic interactions between particles into account by formulating the volume average scheme with probability density function. The contribution to the bulk stress was found to be where ϕ is the particle volume fraction. The probability density function is indeterminate in the simple shear flow, therefore the expression for the effective viscosity was calculated in an extensional flow. The difficulty of obtaining exact theory for concentrated suspension is inherent in the statistical problems, in which the mutual interactions of trajectory particles have to be considered. Choi and Schowalter (1975) used cell model with a deformable sphere in the center and imposed the far field boundary conditions around the cell to obtain a constitutive relation for the concentrated suspension. The drawbacks of the cell model is that the result depends on the shape of cell and boundary conditions and the particle interactions are not included explicitly. Frankel and Acrivos (1967) and Goddard (1977) adopted classical theory of hydrodynamic lubrication to study concentrated suspensions of rigid spheres and Hookean spheres respectively, by calculating the energy dissipated in the film between spheres. Without considering the statistical mechanics of the suspension, this analysis has the same weakness as the cell model.

Suspensions with a polymer continuous phase have particularly complex in bulk properties. Highgate and Whorlew (1970) measured the relative viscosity and normal stress difference of rigid sphere suspensions in different viscoelastic fluids with volume fraction up to 10%. The relative viscosity was found to increase with sphere concentration and decrease with shear rate until reaching an asymptotic value. The same trend was observed for normal stress difference. The correlation of results showed that if relative viscosity is defined as a ratio of viscosity of suspension to that of suspending fluid at the same shear stress, it is then a function of concentration only. Similar observation on the relative viscosity was reported by Kataoka, et al. (1978) at low shear rate region. The relation of relative viscosity can be affected by the particle size distribution. Han and King (1980) measured the bulk rheological properties of emulsions with various composition ratio of viscoelastic droplets in viscoelastic medium, Newtonian droplets in viscoelastic medium and Newtonian droplets in Newtonian medium. They observed maxima and minima in the bulk viscosity and normal stress difference at certain composition ratios for all the systems studied. These extrema are strongly influenced by shear rate and the state of both phases. This is no existing theory at present time to interpret the experimental results such as the ones above. In this study, we propose that if the elasticity of the medium

solution is taken into account, the nonlinear bulk properties of non-Newtonian suspension may be described adequately.

CHAPTER 2

PROBLEM STATEMENT

2.A Problem Statement

The problem addressed in this work is to explain and correlate observed trends in apparent viscosity for two phase flow through a duct of dilute gas bubble suspensions in viscoelastic fluids. Gauthier et al. (1972 a,b) first observed that phase segregation occurs in the Poiseuille flow of viscoelastic suspensions. At steady state there exist a uniform bubbly core and a bubble free layer next to the wall. A concentration distribution profile across the channel was computed by counting number of bubbles on a photographic plate. This technique is inadequate quantitatively since all bubbles in the entire domain unaccounted for in one dimensional photography. Further no rheological data was ascertained in his work. Prud'homme (1978) reported that there exists a threshold wall shear stress above which bubbles migrate from the wall. Beyond this threshold wall shear stress he noted that the apparent viscosity of the suspension in flow is lower than that of the liquid medium.

Quemada (1977) has discussed the use of observed concentration profiles and a relative viscosity relation to predict velocity profiles and flowrates for two-phase flow of suspensions in Newtonian liquids (such as blood) through tubes and slits. In particular, when Brownian diffusion is

negligible and concentration profile is rectangular with a uniform core and a wall layer, the relative viscosity relation for the suspension may be verified directly by measuring the flowrate. The concentration profiles used in this approach must be stationary. The same approach can be used in the two-phase flow of gas bubble suspensions in viscoelastic fluids with a study of bubble concentration profiles established in the flow. A discussion of the relation between wall shear stress and flow rate can illustrate our objectives cleaner.

2.B Flow Structure and Apparent Viscosity

A two-phase flow structure such as that shown in Figure 2.1, has been suggested by Gauthier and Prud'homme as a result of particle distribution in the viscoelastic liquids. The gap between two parallel plates consists of a bubbly of thickness Δ_c and uniform bubble volume fraction ϕ_c with a wall layer of bubble free liquid. The apparent viscosity may be defined for the entire flowing suspension between

$$\eta_a = \frac{\tau_w h}{6 \langle v \rangle} \quad (2.1)$$

where τ_w is the wall shear stress, h is the gap between plates and $\langle v \rangle$ is the average linear velocity which can be calculated from the volumetric flowrate. The wall shear stress can be obtained from the observed pressure gradient

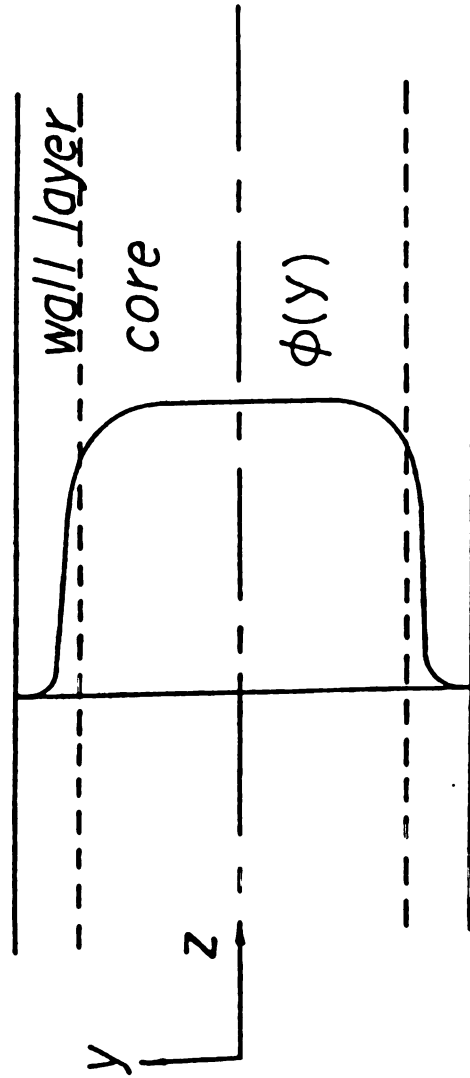


Figure 2.1 Two-phase Flow Structure

along the channel by assuming the gradient is linear and normal stress τ_{yy} is negligible. So that

$$\tau_w = \left(\frac{\Delta P}{L}\right) \frac{h}{2} \quad (2.2)$$

where $\Delta P/L$ is the pressure gradient. The velocity profiles in the two layers may be obtained from the equations of motion given as

$$\eta_c \frac{\partial v}{\partial y} = - \frac{2\tau_w y}{h} \quad 0 \leq y \leq \frac{\Delta c}{2} \quad (2.3)$$

$$\eta \frac{\partial v}{\partial y} = - \frac{2\tau_w y}{h} \quad \frac{\Delta c}{2} \leq y \leq \frac{h}{2} \quad (2.4)$$

where η_c is the effective shear viscosity of the bubbly core, η is the shear viscosity of the medium in the outer layers and y is the distance from flow axis. At present, there is no appropriate model to describe the bulk shear viscosity of bubble suspensions in viscoelastic fluids. However, the effective shear viscosity $\eta_c(\dot{\gamma}, c)$ is expected a function of the bubble concentration in the core as well as shear rate from the experimental evidence. A constitutive equation to describe the stress-strain relation of bubble suspension in viscoelastic liquids adequately, has to be sought to solve for the velocity profile. The relationship between the viscosity and shear rate is self-consistent if the dependence of viscosity on the concentration is known. Besides having the constitutive equation for the bubbly

core, the bubble concentration in the core and bubble-free layer thickness have to be measured along with wall shear stress to obtain the velocity profiles $U_1(y)$ and $U_2(y)$, which denote velocity in the two layers. The boundary conditions yet to be taken into consideration may be written as

$$U_1 = U_2 \quad \text{at} \quad y = \frac{4c}{2} \quad (2.5)$$

$$U_2 = 0 \quad \text{at} \quad y = \frac{4c}{2} \quad (2.6)$$

Thus, the average velocity $\langle U \rangle$ over the gap and the apparent viscosity may be computed for observed values of τ_w , ϕ_c and Δ_c to test the bulk stress relation for the core and to predict the trends for apparent viscosity.

2.C Objectives

The objectives of present study are:

- 1) to verify the existence of a stationary, uniform, bubbly core and a bubble-free wall layer in the viscoelastic two-phase flow.
- 2) to correlate the effect of viscoelasticity with the development of bubble concentration profiles.
- 3) to develop a bulk stress relation for dilute suspension of neutrally buoyant, uniform size, spherical Newtonian drops in viscoelastic liquid medium.
- 4) to test the bulk stress relation under conditions when the two-phase flow consists of a bubbly core and wall

layers.

- 5) to predict the trends for apparent viscosity from observed values of wall shear stress, core thickness and bubble concentration in the core.

To approach the first two objectives, we designed an experimental apparatus which allows us to obtain a slow steady unidirectional and isothermal flow through a slit. A radiation gauge was implemented to measure on-line density variations transverse to the flow. The experimental setup along with procedures for preparing gas bubble suspensions and for obtaining bubble concentration profiles are described in chapter three and four. The profiles measured with two different Separan solutions and Newtonian corn syrup as media are compared and effects of non-Newtonian behavior on the development of concentration profiles are correlated in chapter five. In chapter six, the classical volume average method is utilized to achieve a theoretical relation for the bulk stress of a dilute suspension of neutrally buoyant, spherical Newtonian drops in a second order fluid undergoing a simple shear flow. The effect of medium elasticity on the shear viscosity and normal stress coefficients is discussed. Finally, in chapter seven, with all the knowledge pursued, the predicted trends for apparent viscosity are examined in the light of data. An overall review on the present study and recommendation for future research in the polymeric two-phase flow are discussed in chapter eight.

CHAPTER 3

EXPERIMENTAL ARRANGEMENT AND MATERIALS

The bulk properties of gas bubble suspensions in viscoelastic fluids are dependent on temperature, viscoelasticity of medium fluids and bubble bulk concentration. In addition, the flow is complicated by bubble growth, bubble migration and bubble rise. This investigation focuses only on the effect of bubble migration on the bulk properties, and thus we limit ourselves to slow, isothermal, uniform size gas bubble suspensions in viscoelastic fluids. Based on these specifications, the apparatus and instrumentation were designed to permit on-line measurement of density variation along the flow. Solutions were chosen so that various fluid properties could be used to achieve low Reynolds numbers and significant migration effects. A new gas bubble generation method was introduced to yield uniform-size hydrogen gas bubbles at room temperature. The procedure for measuring flow rate and pressure gradient is described in this chapter. The calibration and procedures to obtain the two-dimensional bubble concentration profile are presented in the next chapter.

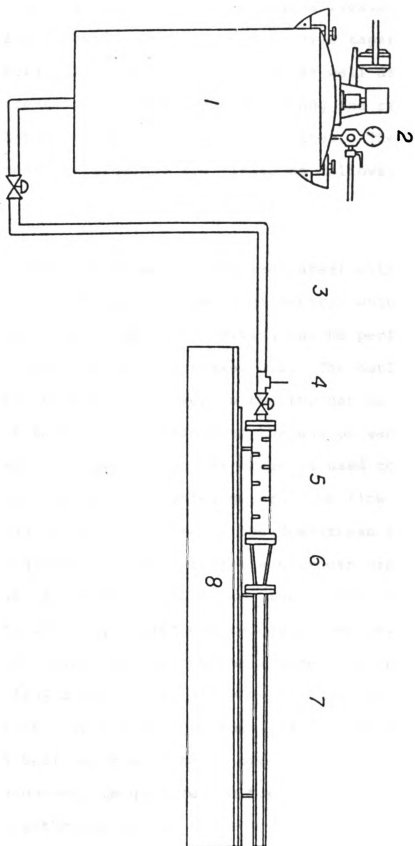
3.A Apparatus

A schematic of the flow arrangement is presented in Figure 3.1. The gas bubble suspension was forced out of a

Figure 3.1 Schematic of Flow Arrangement

The components are labeled with numbers.

- 1. Tank**
- 2. Pressure regulator**
- 3. Flexible tube**
- 4. Gas release needle**
- 5. Circular static mixer**
- 6. Transition channel**
- 7. Slit section**
- 8. Stand**



tank by compressed nitrogen, through a flexible hose, a ball valve and a static mixer, connected by a tapered transition to a rectangular channel. The flow as well as density measurements were carried out all along the rectangular channel by methods to be described later. The dimension and function of each device are listed as follows:

Tank

The tank is made of galvanized steel with a 55 liter capacity (72 cm high, 32 cm in diameter), which may be pressurized up to 30 psig. Mixing can be performed by a stirrer propelled by compressed air. The outlet of the tank is at the bottom, the cover on the top can be removed so that the tank can be cleaned at the end of each experiment. The pressure regulator on the cover is used to adjust the tank nitrogen pressure which governs the flow rate. At the beginning of each experiment, the downstream valve of the tank is always closed so that the nitrogen pressure inside the tank can be adjusted. Tygon tubing with 7/8" diameter connects this valve with gas releasing device. The flexibility of Tygon tube allows the movement of the flow channel in the flow direction to allow measurement of axial density variations. To ensure a uniform, small-size bubble suspension, a ball valve with small opening is installed to screen off the uneven, large sized bubbles. Bubbles larger than .4 to .6mm gathering behind the throttled valve are drawn out

by a syringe needle inserted vertically through a rubber stopper which is tightened in a tee tube into the piping ahead of the valve. This device also eliminates surges in the flow which might occur with occasional bursting of large bubbles. From here on, bubble suspensions enter the static mixer.

Flow Channel

The flow channel comprises three sections in sequence: a static mixer, a transition channel and a slit channel, all are made of plexiglass. The transparency of plexiglass allows good flow visualization. The static mixer (Figure 3.2) consists of a circular pipe, 30.5 cm long, 3.8 cm in diameter, within which are fixed a series of triangular elements arranging in a spiral fashion. These elements are aligned perpendicularly to the flow direction as suggested by Middleman (1977), to create a rotational flow and therefore achieve a radial mixing. The mixing destroys the inhomogeneity caused by bubble migration and leads to a homogeneous suspension before entering the slit section. The transition channel, 8.9 cm long, connecting the static mixer and slit channel, is built in the tapered shape to eliminate secondary flow near the entrance. The cross sectional area of these three sections are the same to retain a constant velocity. These individual flow compartments are bolted together and mounted on a horizontal stand with axial guides

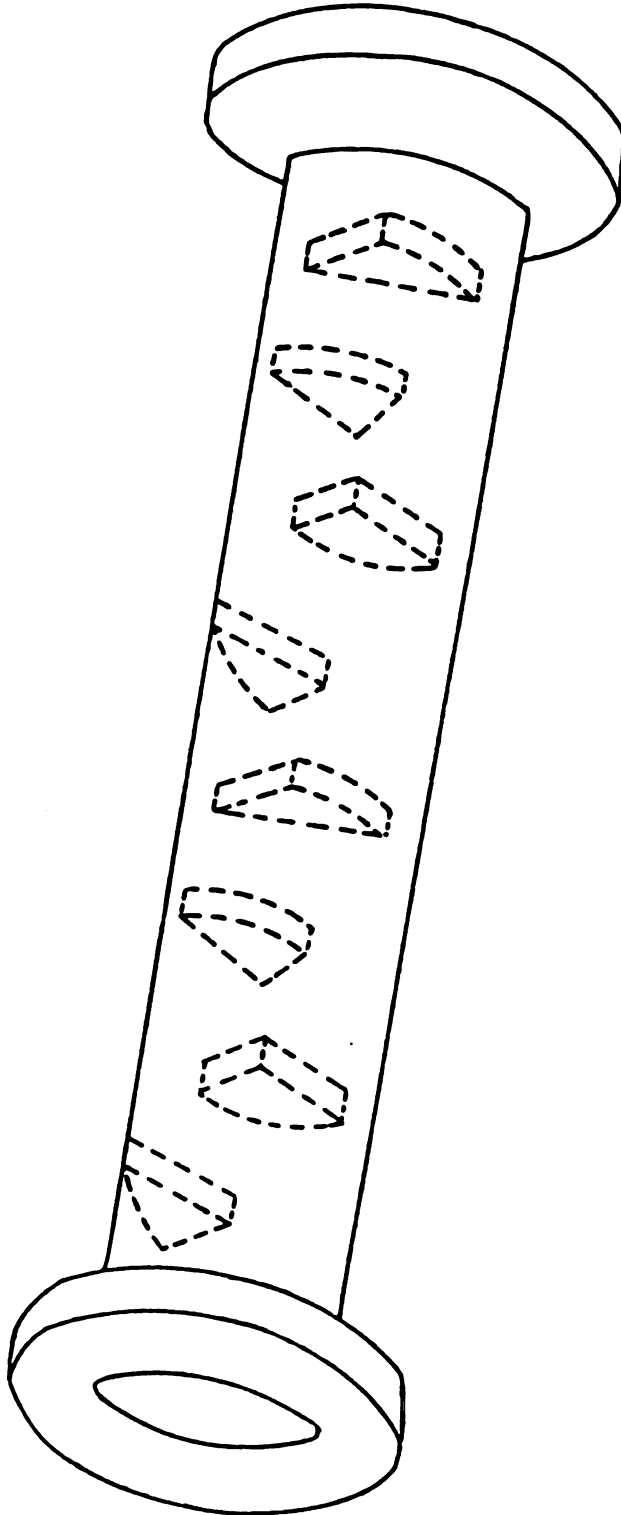


Figure 3.2 Static Mixer

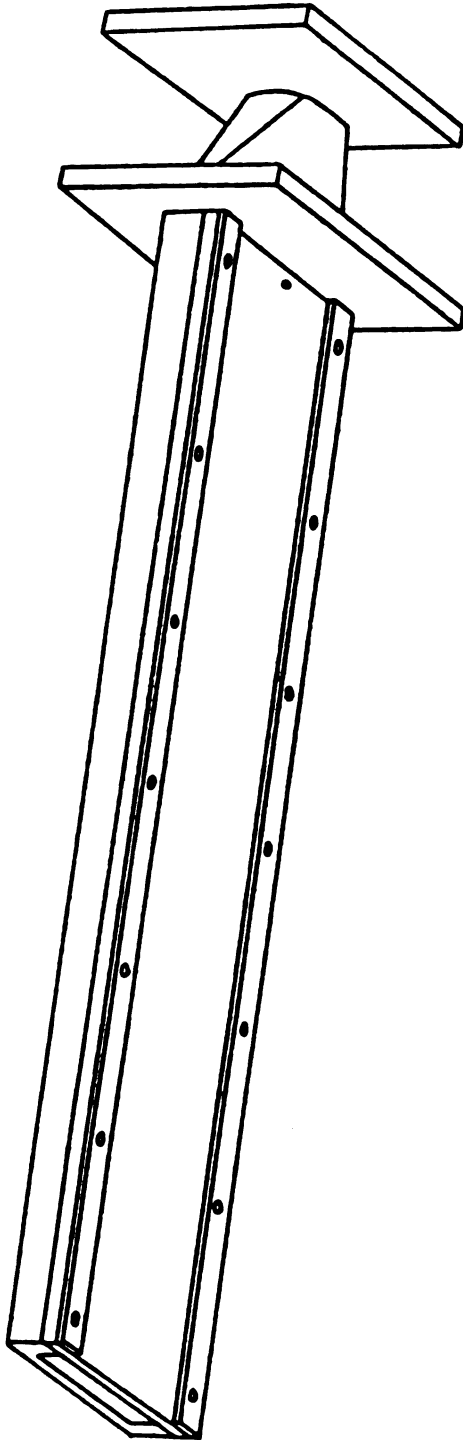


Figure 3.3 Transition Channel and Rectangular Channel

to allow longitudinal movement of the flow channel. They can also be taken apart for cleaning.

The two most commonly used flow channels for Poiseuille flow structure are circular tube and rectangular channel, the latter corresponds to parallel plates. From instrumental and photographic considerations, the rectangular channel offers a better geometry for two-phase flow study. It provides a uniform cross section, so that the distance which the gamma rays penetrate through the suspension is constant along the transverse direction. The flat walls eliminate optical distortion. This rectangular channel (Figure 3.3) is 63.5 cm long, .9 cm wide and 1.27 cm in height. The upper plate is fastened to a U shape open channel, which is removable for cleaning. The thickness of the top and bottom plates is .635 cm and the side walls are 2.03 cm. The channel can sustain pressure up to 25 psig. With aspect ratio (W/h) equal to 7, the flow inside the channel can be approximated as an ideal Poiseuille flow between parallel plates (cf. Middleman (1977)). The entrance length for the flow to be fully developed is .5 cm (cf. Middleman (1977)), which is 1% of channel length. The entrance effect is negligible. A pressure transducer is located 2.5 downstream from the entrance.

3.B Materials

The gas bubble suspensions were prepared in three different media - a Newtonian corn syrup, and two non-Newtonian

aqueous solutions of polyacrylamide (Separan AP-30) containing 2.5 and 3.5 weight percent respectively of the polymer. The viscosity η , the primary normal stress coefficient ψ_1 , and recoverable shear ratio, $S_R = \psi_1 \dot{\gamma} / \eta$ (all evaluated at a shear rate of 1 sec^{-1} for the Separan solutions), the density ρ and interfacial tension σ are listed in Table 3.1. The methods and procedures of preparing solutions as well as measuring these media properties are described in the following sections.

Corn Syrup:

Syrup is a well known Newtonian solution. Crystal syrup, a commercial product of A.E. Staley Manufacturing Co., Illinois, was used to prepare the Newtonian fluid. The contents in crystal syrup are water, corn syrup, sugar and citric acid. The viscosity of this commercial syrup is too low to eliminate the bubble rise. To obtain a higher viscosity, some water was boiled off. The color of the syrup changed from clear to brownish transparency. This was caused by the over-heating of carbons in the glucose. However, the heating process did not change the Newtonian behavior of the syrup.

Aqueous Separan Solutions

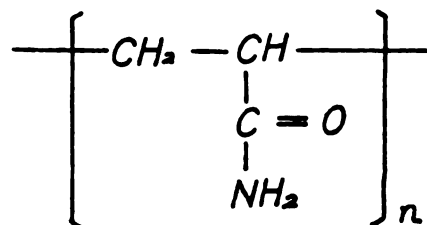
Separan AP 30 is a synthetic polyacrylamide, manufactured by Dow Chemical Co., with a weight average molecular

Table 3.1 Properties of Media

Medium	Density (g/cc)	Surface Tension (dynes/cm)	Viscosity (poise) *	Primary Normal	Recoverable Shear Ratio SR=N ₁ /2 *
				Stress Coefficient $\frac{\text{dyne-sec}^2}{\text{cm}^2}$	
Corn Syrup	1.414	60.6	285	0	0
2.5 wt % Separan Solution	1.006	40.4	368	140	0.19
3.5 wt % Separan Solution	1.008	44.7	1210	1540	0.64

*Evaluated at a shear rate of 1 sec⁻¹.

weight of 4×10^6 . This anionic polyacrylamide is water soluble, has the following structure



Separan AP-30 has good thermal stability below 210°C , and good resistance to shear degradation. Solid Separan polymer can be dissolved in water in all proportions. For organic solvents with high oxygen-to-carbon ratio, eg. glycerin, ethylene glycol can dissolve or swell the polymer. Solvents like ether, benzene, hexane, methanol and chloroform will not dissolve the polymer. The viscosity and normal stresses of Separan aqueous solutions are functions of temperature, concentration as well as pH value.

The manufacturer recommended way to make Separan aqueous solution is first soaking polymer powder in methanol to keep the polymer from agglomerating into gelatinous lumps and then adding water to the solution while stirring. With occasional mixing for three days, the polymer powder can dissolve in water completely in all proportions. 2.5 wt percent and 3.5 wt percent aqueous Separan solutions were prepared.

Viscosity, Normal Stress Measurements

The rheological properties of medium solutions were measured at room temperature with Weissenberg

Rheogoniometer, a simple cone and plate viscometer. The rheogoniometer can carry out steady shear flow measurement and oscillatory shear flow measurement. For this study, only steady shear flow material functions are required. The directly measured quantities from the rheogoniometer are not material functions but forces and torques on the cone and plate and angular velocity of the rotating plate. The viscosity can be obtained from the torque and angular velocity by

$$\eta = \frac{3\mathcal{T}}{2\pi R^3 \dot{\gamma}} \quad (3.1)$$

$$\dot{\gamma} = \frac{\omega_0}{\theta_0} \quad (3.2)$$

\mathcal{T} is the torque, R is the radius of the plate, ω_0 is the angular velocity and θ_0 is the angle between cone and plate. A cone angle of 0.5522° and a plate diameter of 7.5 cm are used in the measurement. The primary normal stress coefficient can be calculated from the force and angular velocity

$$\psi_1 = \frac{2\mathcal{F}}{\pi R^3 \dot{\gamma}} \quad (3.3)$$

The procedure for obtaining the primary normal stress is worth noticing in this study. The piezoelectric load cell (922F) and coupler (549) supplied by Sundstrand Data Control, Inc. which designed to sense the normal force on the plate for the dynamic measurement. In the shear flow

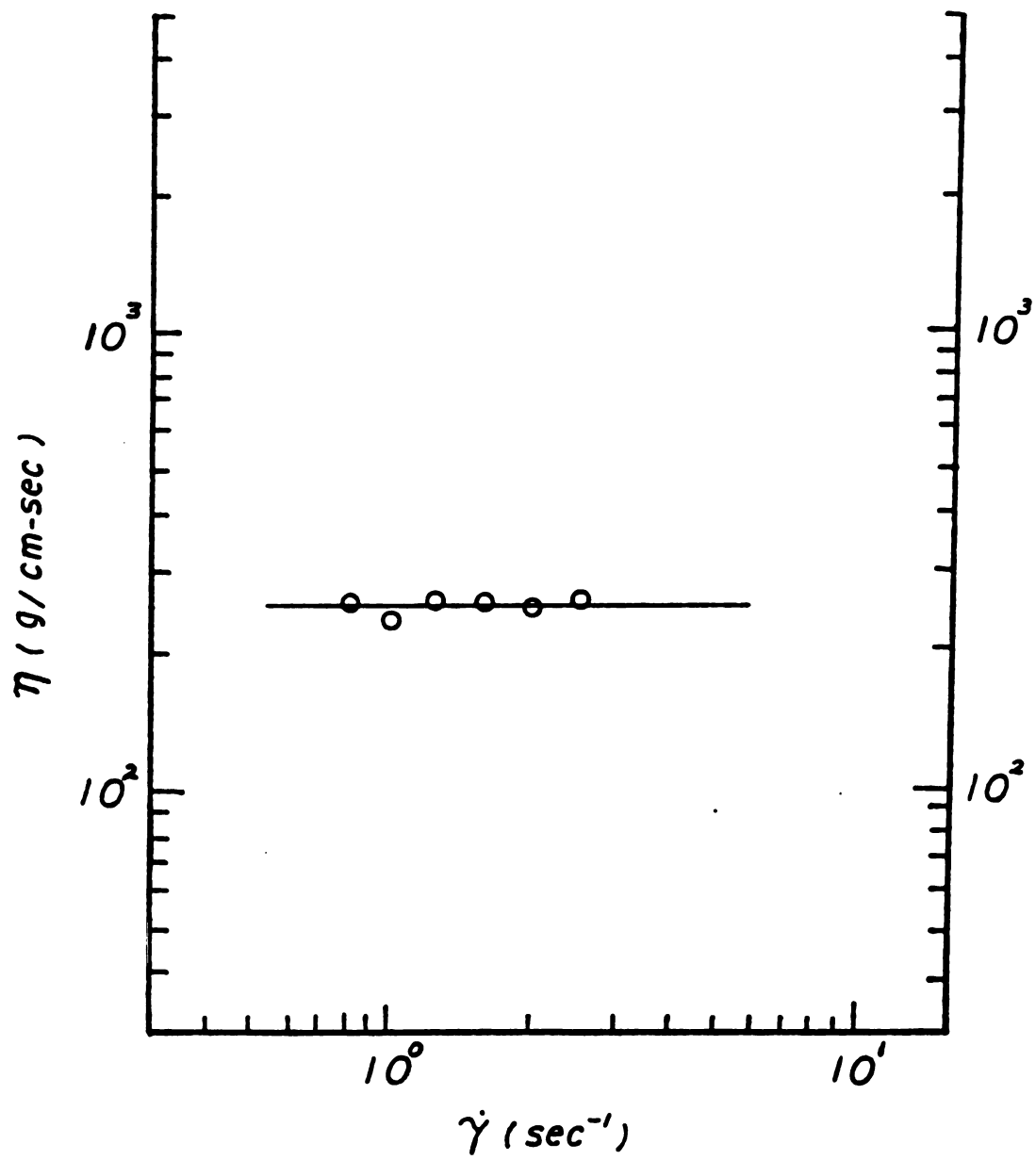


Figure 3.4 Viscosity of Corn Syrup Solution

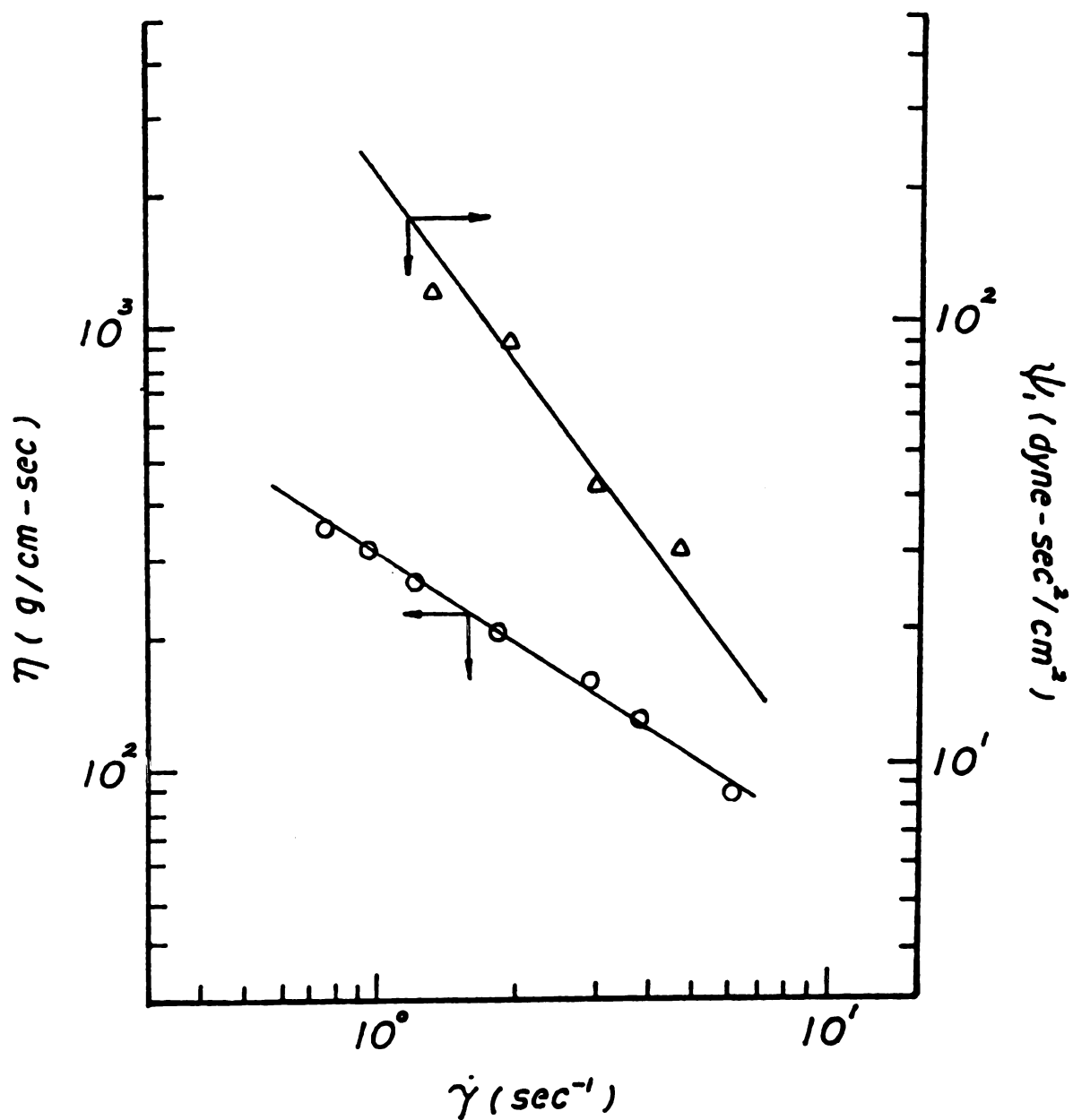


Figure 3.5

Viscosity and Primary Normal Stress
Coefficient of 2.5 wt Percent
Aqueous Separan Solution

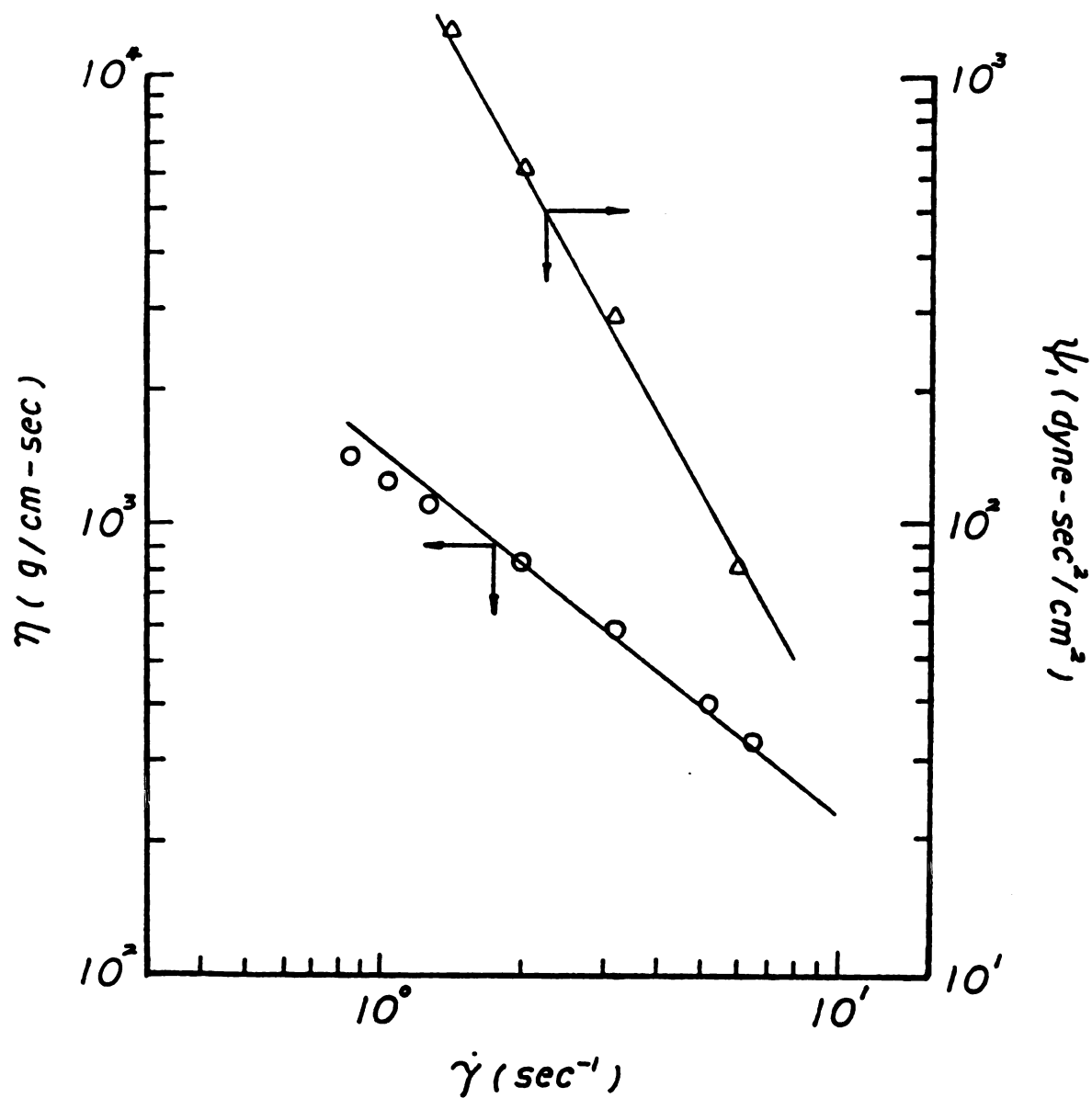


Figure 3.6

Viscosity and Primary Normal Stress
Coefficient of 3.5 wt Percent
Aqueous Separan Solution

experiment, the transient response was found too quick to catch visually. Therefore a storage oscilloscope was employed to record the voltage variation, which was then converted to the normal force. The instrumental inertia force was not corrected for our measurements. However, the results compare well with those of Chin et al. (1979). The variation of η and ψ , with shear rate is shown in Figures 3.4 to 3.6. The viscosities of Separan solution are shear-thinning and can be described by the power-law relation

$$\begin{aligned}\tau &= K \dot{\gamma}^n \\ \eta &= K \dot{\gamma}^{n-1}\end{aligned}\tag{3.4}$$

where K and n are 36.8 N.secⁿ/m², 0.346 for 2.5 wt percent Separan solution and 121 N.secⁿ/m², 0.225 for 3.5 wt percent Separan solution.

Surface Tension Measurement

The tensiometer used for the measurement of surface tension utilizes the du Nouy ring method. The force required for the rupture of a liquid film forming on a wire ring is correlated to the surface tension. It depends on the density of the liquid and dimensions of the ring. The surface tension can be calculated by the following relations.

$$\text{Surface Tension} \quad \sigma = S \times J \tag{3.5}$$

where S: scale reading when film ruptures, dyne/cm

J: factor converting scale reading to surface tension

$$\text{and } J = .725 + \frac{.01452B}{C^2(\rho - \rho_{air})} + .04534 - \frac{1.679}{R/r} \quad (3, 6)$$

where c: Circumference of ring, cm

ρ : density of solution, g/ml

ρ_{air} : density of air, g/ml

R: radius of ring, cm

r: radius of wire of ring, cm

A ring of radius, 0.637 cm, circumference, 4 cm and a wire of radius 0.015 cm was used in our measurement.

Density Measurement

The density was measured by a pycnometer which is made for viscous fluids. Its volume was calibrated with distilled water at room temperature. The void fraction of bubble suspension can be calculated from the following arguments.

The void fraction of gas in the suspension is defined

$$\begin{aligned} \phi &= V_g / (V_g + V_L) \\ &= (\rho_L - \rho) / (\rho_L - \rho_g) \end{aligned} \quad (3.7)$$

subscripts l, g refer to the continuous phase and dispersed phase. The density of gas is negligible compared to the medium solution. The void fraction can thus be calculated from the density by the relation.

$$\phi \simeq (\rho_L - \rho) / \rho_L \quad (3.8)$$

In our experiment, the bulk void fraction was measured from the suspension at the channel exit. This bulk void fraction represents the bulk void fraction throughout the channel only if bubble growth is negligible. By assuming the dispersed phase behaves like an ideal gas, the void fraction of gas at the inlet of channel is presented in term of the outlet quantities as

$$\begin{aligned} \phi_{inlet} &= \frac{\rho_L - \rho}{(\rho_L - \rho) + \beta(\rho - \rho_g)} \Big|_{outlet} \\ &= \frac{\rho_L - \rho}{(\rho_L - \rho) + \beta\rho} \Big|_{outlet} \end{aligned} \quad (3.9)$$

where $\beta = P_{inlet} / P_{outlet}$

In our experiment, the ratio β is close to 1. Therefore, the void fraction can be assumed constant throughout the channel. This is confirmed by photographic observations.

Pressure Measurement

The inlet pressure was measured by a piezoelectric pressure transducer (Model no. XTM-1-190-10) manufactured by Klute Semiconductor Co. This pressure transducer uses a metal diaphragm as a force collector with an integrated sensor as its sensing element. The allowable maximum torque to this transducer is 25 lb_f. The rated excitation pressure is 10 psig, but it can withstand pressure up to 30 psig. The measured pressure is signaled out as voltage, so a digital voltmeter was used to provide the reading. The sensitivity of the pressure transducer was calibrated by a well-adjusted pressure gauge. The calibration was done by correcting the transducer and pressure gauge to a tee which links to a nitrogen cylinder. By varying the nitrogen pressure, we obtained pressure readings from the gauge and voltage readings from the pressure transducer. The pressure vs voltage was plotted (Figure 3.7) and the calibration of the pressure transducer is 4.7 psi/mV. The transducer was mounted on the top channel plate flush with the flow. This eliminated the pressure hole error, which is commonly manifested in the gauge measurement for viscoelastic fluids.

Flow Rate Measurement

The volumetric flow rate was measured by timing the flow from the exit into 500 ml, 1000 ml cylinders with a

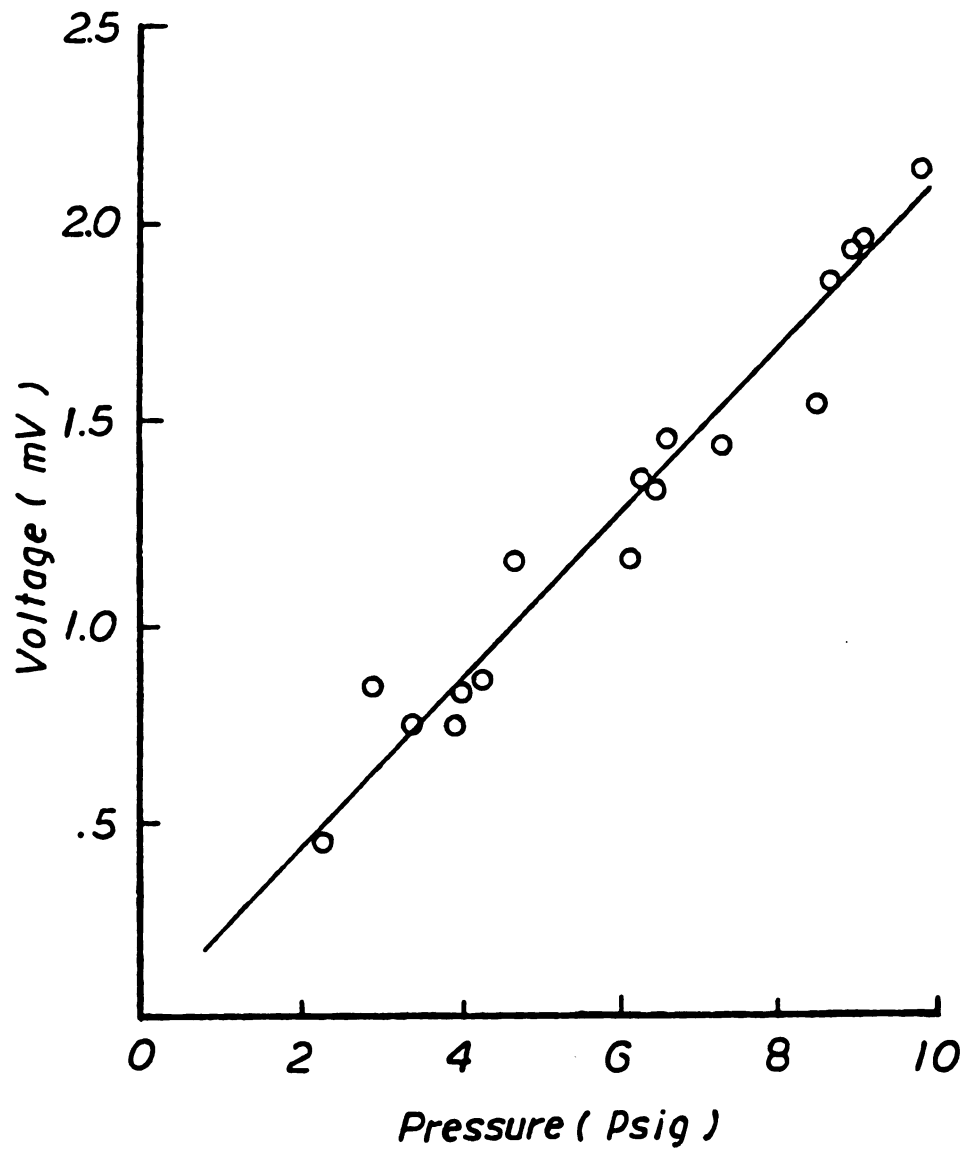


Figure 3.7 Sensitivity of Pressure Transducer

stop watch. Since the time to fill up the cylinders ranges from 20 seconds to 80 seconds, it is long enough to minimize the error. The measurement on the volume flow rate was recorded right after the collection, so that bubble rise and growth were minimized.

Bubble Generation Method

Gas bubbles were generated at room temperature without noticeable heat effects by using finely powdered sodium borohydride as chemical blowing agent. Sodium borohydride reacts with water to liberate hydrogen according to the reaction (Wade and Letendre (1980))



With borohydride, a chemical reaction occurs where in a proton (H^+) reacts with the hydride hydrogen (H^-) on the BH_4^- group to produce H_2 gas. This reaction is accelerated as the acidity of the system is increased; hence the yield of hydrogen gas per gram of hydride is less in basic Separan solution than in the corn syrup. At room temperature, hydrogen gas produced in corn syrup is about 800 cc/gram of NaBH_4 , and 50 cc/gram of NaBH_4 in Separan aqueous solutions. The water loss from the test solutions due to the hydrolysis reaction is 10^{-4} of the total volume of the solution. The residue, sodium metaborate is traceless in the solution, and

of negligible amount compared to the whole volume of solutions.

Bubble Size Measurement

Bubble size was determined from the photographs of the flowing bubble suspension. With a polarized filter on the close-up lens of a Canon F camera placed beneath the lower plate of the slit section and a light source above the top plate, no optical distortion was observed. Photographs of the flowing bubble suspension near the entrance and the end of the flow channel, 5 minutes and 20 minutes after startup of the flow are presented in Figure 3.8 to 3.11. The bubble suspension was prepared with 3.3 volume percent of bubbles in a 3.5 wt percent aqueous Separan solution; the average velocity during this run was 0.66 cm/sec, amounting to an average residence time in the channel section of 1.5 minutes. The dimension from left to right in each figure represents 2.6 cm along the flow direction. It may be seen from these Figures that bubbles are mostly 0.4 to 0.6 mm in diameter and that the bubble size distribution does not change significantly between the entrance and the end over the course of the experiment. This is true for all the media used in this study.

These photographs also indicate the formation of ordered aggregates of a few bubbles along the flow direction. This phenomenon has been reported by Michele et al.

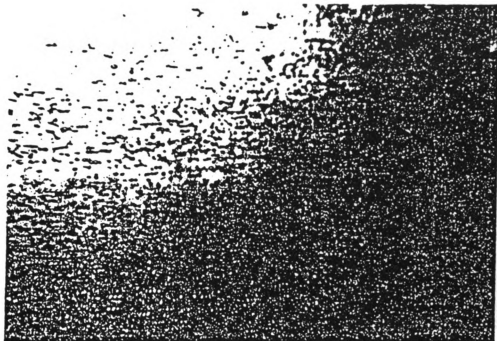


Figure 3.8 Photograph of Flowing Suspension at
Entrance, 5 min. After Startup



Figure 3.9 Photograph of Flowing Suspension at
Entrance, 20 min. After Startup

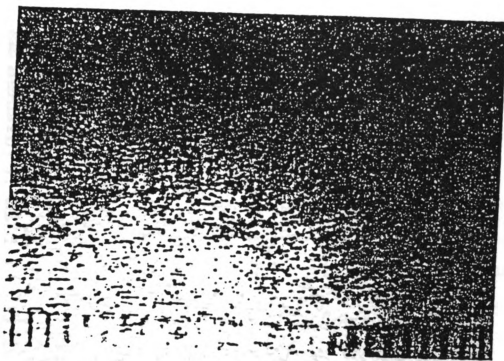


Figure 3.10

Photograph of Flowing Suspension at
End of Channel, 5 min. After Startup

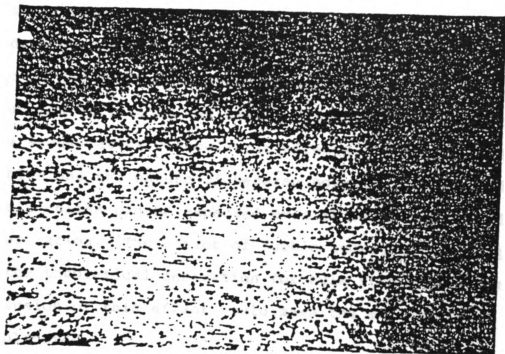


Figure 3.11 Photograph of Flowing Suspension at
End of Channel, 20 min. After Startup

(1977) who observed suspensions of glass spheres in different polymer liquids subject to laminar shear flows. Michele et al. report that aggregation is more noticeable in liquids with high recoverable shear ratios ($S_R \sim 10$). Polymer bridging between particles is widely recognized as the cause of this aggregation; the strength and number of such bridges depend not only on the elasticity of the liquid but also on the interaction between particle surface and polymer molecules (cf. Vader and Dekker, 1981). As a result of long term accumulative viscoelastic effects, deformation of bubbles and the nature of Separan polymer, the formation of bubble chains can be expected even at lower recoverable shear ratios. The effect of bubble aggregation is neglected in the theoretical derivation for bulk stress relation, the inclusion of this effect would make the analysis much more complicated.

Preparation of Gas Bubble Suspensions

Before dispersing the granular powder of sodium borohydride into the solution, air bubbles trapped in the process of preparing aqueous Separan solutions were eliminated by drawing a vacuum on the tank containing the solution; when this was achieved, the vacuum was released gradually to return the tank to atmospheric pressure. The correlation between hydrogen yield and amount of sodium borohydride was tested in the medium solutions, 800 cc/gm for corn syrup, 150 cc/gm

for Separan solutions. According to this estimated scale, sodium borohydride was weighed and mixed slowly into the solution at several points in the tank. The reaction was simultaneous once the powder contacted the solution, hydrogen gas bubbles formed immediately. A quick mixing was performed. Strenuous stirring must be avoided to prevent degradation of the polymer solutions. The mixture was then pressurized out of the tank into a container. The fluid was then mixed again to ensure a uniformly distributed bubble suspension. This mixture was poured into the tank and ready for the experiment. The bubble suspensions behave differently in corn syrup and Separan solutions, bubbles were segregated and stable in corn syrup but tended to grow and agglomerate in Separan solutions. Separan polymer is well known for its use in the flocculation of solid particles in suspension. This particular mechanism may account for the agglomeration of bubbles. The result is a suspension with mostly .4 to .6mm diameter bubbles and a few considerably bigger bubbles; the bigger bubbles were eliminated later with a syringe needle installed along the flow channel.

Procedure of Flow Experiment

The procedure for apparent viscosity measurement was carried out in the following sequence.

1. The bubble suspension was prepared in the solution and ensured that it was well mixed.

2. The tank was pressurized with nitrogen gas and the pressure inside the tank was adjusted with a regulator.
3. The valve was opened for the flow.
4. Data were collected once the flow was stabilized as indicated by the pressure transducer reading.
The voltage reading on the voltmeter was recorded for translation to pressure gradient later.
5. A graduated cylinder was placed at the channel exit to collect suspension flow; a timer was set to count simultaneously. When the cylinder was almost filled, it was removed from the flow and the timer stopped. The flow volume and time were recorded.
6. The density measurement was started right after the flow rate was taken.
7. The suspension discharge was collected in a pycnometer at the channel exit.
8. Nitrogen supply was turned off to stop the flow. The voltage reading was recorded as the reference of zero pressure.
9. The pycnometer was weighed to yield the bulk void fraction.
10. The residue fluid was discharged from the tank and the whole apparatus was washed with water to avoid the build up of corn syrup or polymers on the channel wall and tank wall.

The bubble generation from sodium borohydride offers an

isothermal flow, however the bulk void fraction (especially in Separan solutions) is not easy to control with different factors involved in the process. With this limitation, it is difficult to fix the bulk void fraction, so that the effect of shear stress can be studied alone. Another problem in the flow measurement is that the pressure gradient can not be fixed constant for different runs within the transducer sensitivity range. Efforts were made to provide systematic study on the trend of the apparent viscosity.

CHAPTER 4

RADIATION GAUGE

In the previous studies, two techniques, optical and photographic, were used to study the particle concentration distribution due to particle migration. Segre and Silberberg (1962) used an optical scanning device consisting of mutually perpendicular light beams, photoelectric transducers and electric counting circuits. The numbers of particles passing through the cross section of light beams were counted and registered. However, this device can not distinguish between the signal from the presence of a single particle in the cross section and the coincidental presence of two particles in the area. The photographic method used by Gauthier et al. (1971 b) discussed in Chapter 2 is doubtful for its accuracy. The radiation attenuation technique employed in this study has been recognized for its accuracy for void fraction measurements in the two-phase flow (Schrock (1969), Adams, et al. (1970)). A radiation gauge was implemented for measuring the axial and transverse void fractions in viscoelastic fluids. The most widely used radiation sources are gamma-rays and x-rays, both of which absorbed more strongly in denser phases than in lighter ones. X-rays are typically low energy photons which are easily absorbed more strongly by structural materials and human body. Gamma rays are more penetrating and are easily produced by a compact

radioisotope source.

4.A Principles of Gamma Attenuation

When a monoenergetic collimated beam of gamma rays with an initial intensity of I_i photons/cm²-sec passes through a homogeneous material with a thickness t , its intensity will be reduced to another level, I , according to an exponential law

$$\frac{I}{I_i} = \exp(-\mu t) \quad (4.1)$$

where μ is the linear absorption coefficient, cm⁻¹. This coefficient depends on the composition of the absorber and the energy of electromagnetic radiation. It is related to the absorber density by

$$\mu = \frac{N_0 \Sigma}{A} \rho \quad (4.2)$$

where N_0 is the Avogadro's Number, atoms/gm-atom,

A is the atomic mass number, gm/gm-atom,

Σ is the microscopic absorption cross section,
cm²/atom,

and ρ is the absorber density, gm/cc.

With a fixed x-ray source and apparatus geometry (i.e. sample mounting, cross section area of collimated beam), the

linear absorption coefficient, μ can be written as

$$\mu = \theta \rho \quad (4.3)$$

where θ is the mass attenuation coefficient and μ is a function of the nature of the absorber and the energy of the gamma photons. The exponential law of attenuation is then

$$\frac{I}{I_0} = \exp(-\theta \rho t) \quad (4.4)$$

In principle, the beam attenuation technique is simple. A selected radiation source is collimated to produce a unidirectional photon flux normal to the test section. The beam is attenuated in turn by a channel wall, the two-phase mixture and the other channel wall. The beam passes through the opposite collimators and then is measured by an appropriate detector (Figure 4.1). Applying equation (4.4) to this two-phase system, we obtain

$$\frac{I}{I_0} = \exp(-\theta_w \rho_w w) \exp(-\theta_s \rho_s W) \exp(-\theta_w \rho_w w) \quad (4.5)$$

in which subscripts w and s refer to the channel wall and two-phase fluid, respectively

If the two-phase fluid is a homogeneous mixture, its properties can be obtained by the additive relation

$$\theta_s \rho_s = \phi \theta_g \rho_g + (1 - \phi) \theta_L \rho_L \quad (4.6)$$

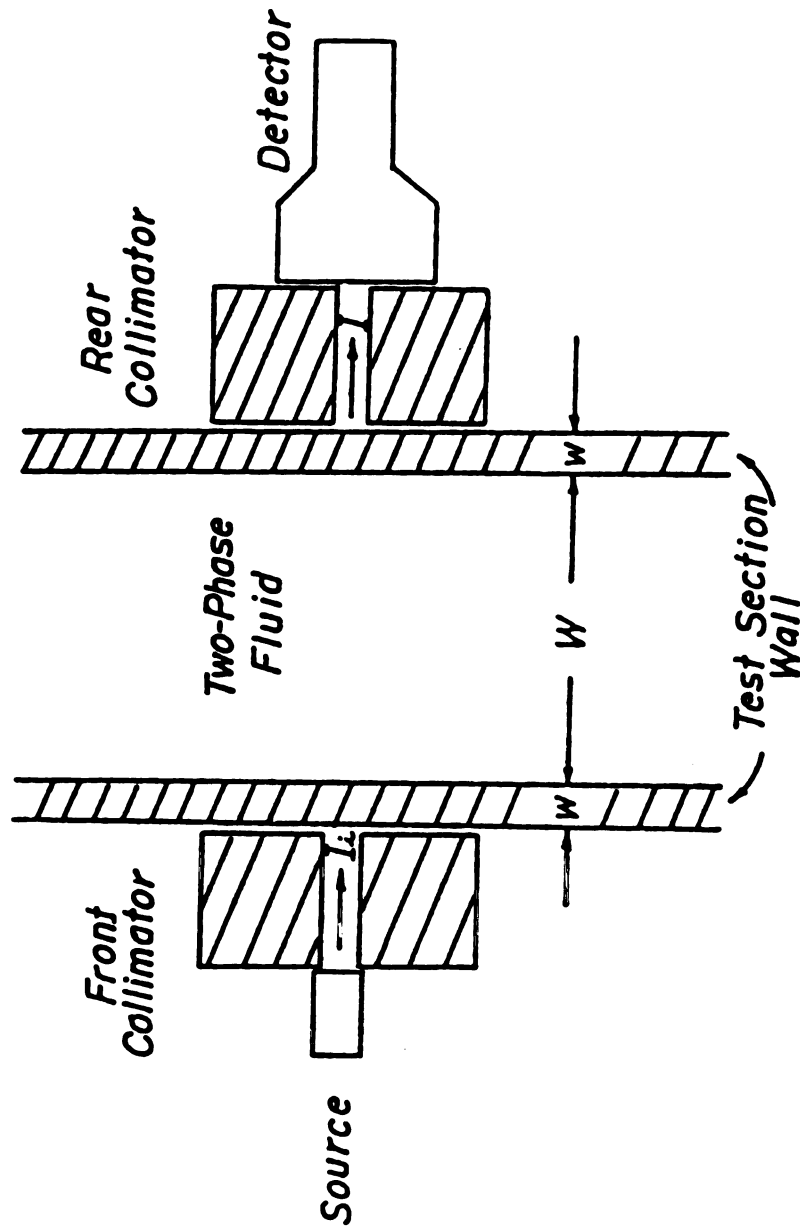


Figure 4.1 Schematic of Linear Attenuation Technique

where ϕ is the void fraction and the subscripts g and l refer to the gas phase and liquid phase respectively. The density of the gas phase is much lower than that of the liquid phase, so that the above relation can be simplified to

$$\theta_s \rho_s = (1 - \phi) \theta_l \rho_l \quad (4.7)$$

For a full channel with liquid phase only

$$\frac{I_l}{I_i} = \exp(-2\theta_w \rho_w w) \exp(-\theta_l \rho_l W) \quad (4.8)$$

From equation (4,5) and (4,8), we obtain

$$\rho_s = \frac{\theta_l \rho_l - \ln(I/I_l)/W}{\theta_s} \quad (4.9)$$

Combining equations (4,7) and (4,9) gives

$$\phi = \frac{1}{\theta_l \rho_l W} \ln\left(\frac{I}{I_l}\right) \quad (4.10)$$

The gas void fraction is determined using the above relation from the beam intensity, which is equivalent to the output signal from the detector; e.g. counts measured by a scaler. The mass attenuation coefficient of the fluid medium has to be calibrated before the experiment. The above equation is valid if the two-phase flow is homogeneous when the gas bubbles are not uniformly distributed. Several researchers

(Petrick and Swanson (1958), Hooker and Popper (1958)) showed that an uneven phase distribution can result in large errors in the void fraction measurement. In the current experiment, the cross-section area of the γ -ray beam is about 0.012 cm^2 , which covers an area of nine bubbles at most. Strictly speaking, the bubbles are uniformly distributed in this small area, thus, this error can be eliminated in the observation.

In our study, due to a stability problem of the radiation gauge (to be discussed in the next section), an altered relation was used to evaluate the density variation, rather than using equation (4,10). Equation (4,9) can be rewritten in a more general form

$$\theta_1 \rho_1 - \theta_2 \rho_2 = \frac{1}{W} \ln\left(\frac{I_2}{I_1}\right) \quad (4,11)$$

where 1 and 2 refer to two-phase fluids 1 and 2.

If continuous phases of these two fluids are the same, then

$\theta_1 = \theta_2$, so

$$\begin{aligned} \rho_1 - \rho_2 &= \frac{1}{\theta W} \ln\left(\frac{I_2}{I_1}\right) \\ &= \frac{1}{\beta} \ln\left(\frac{I_2}{I_1}\right) \end{aligned} \quad (4,12)$$

According to this relation, the relative density change depends on the relative detected radiation intensity and an attenuation coefficient.

4.B Instruments of Radiation Gauge

Gamma Source

Cesium 137, a stable gamma radiation source with an activity of 5 millicurie was used in this study. The half life of Cesium 137 is thirty years making its activity decay negligible during the experimental period. If a short half-life isotope is used, the system has to be calibrated frequently. It is sealed in a capsule (Figure 4,2), which has a circular shoulder making it possible to move it using a 15" long remote handle. It was placed in different sites during the experiment and was kept in a shielded container when it was not in use. The operator has to be well protected to handle the source, i.e., gloves, safety goggles are required. The radiation intensity is inversely proportional to the square of the distance, so that to handling the material from a distance avoids unnecessary exposure. A radiation detector was used frequently to check if there was radiation leakage from the storage container. Routine ring and a body film badges were worn and these films were processed every two weeks to determine the personal exposure.

Scintillator and Photomultiplier

The radiation detector consisted of a sodium iodide scintillator, a photomultiplier, and a counter. The principle of scintillation is to convert the energy of radiation

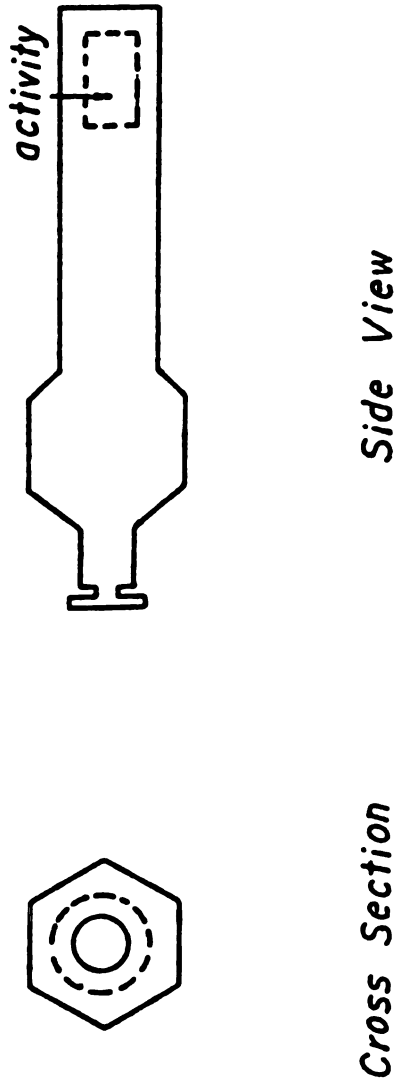


Figure 4.2 Cesium Capsule

rays into light photons so that they can be received by different means, such as image forming, light emission, etc. For gamma-ray measurement, a scintillator of sodium iodide activated with thallium was used. This has a very high photoelectronic detection efficiency due to the high density of NaI and high atomic number of iodine.

The detection mechanism in the scintillator is 1) absorption of gamma-rays energy 2) conversion of absorbed energy into luminescent emission 3) collection of photons on the photosensitive cathode, which is part of a photomultiplier. In the photomultiplier, electrons are accelerated by a high potential to the first dynode. There each electron produces several (n) secondary electrons. These secondary electrons are similarly accelerated to and increased n -fold at the second dynode and so on. With N dynodes the charge of the original photoelectron is amplified N^n times. This multiplication leads to a strong pulse output which is recorded by a counter. The NaI crystal was connected to the photo-sensitive face of multiplier tube with balsam cement to provide better optical contact at the interface. The multiplier was fixed in a light-tight aluminum enclosure which also serves as a reflector to assist in directing light to the photocathode. The sodium iodide crystal, which is very hygroscopic and sensitive to light, was wrapped with tape to protect against moisture and surrounding light sources. The manufacturer suggested that

the photomultiplier tube be shielded from magnetic fields, including the earth's field, to obtain its optimal performance. In the laboratory, very little background noise was received without the shield, so this protection was not utilized. A voltage stabilizer was connected to the photomultiplier high voltage source to prevent fluctuation in the bias voltage. The signal output from the photomultiplier is proportional to \sqrt{I} , so that $\pm 1\%$ of fluctuation in V_b corresponds to $\pm 7.5\%$ of error.

Counter

The pulse produced in the output capacitor of photomultiplier can be further amplified by an external electronic amplifier. The Mini-Scaler (Model MS-2) manufactured by Eberline Instrument Corp. provides a complete system consisting of a variable high voltage supply to the photomultiplier, a charge sensitive input amplifier with very high input sensitivity and noise rejection, a single channel pulse height analyzer which can be used as scintillation spectrometer, a scaler, a rate meter and a timer. The voltage supply is adjustable from 200 volts to 1500 volts. The single channel analyzer uses two discriminators - a pulse height discriminator and a pulse height window discriminator to select the pulses which fall in between the predetermined ranges which are adjusted by the threshold and window settings on the mini-scaler. The device allows true event

pulses to be differentiated from small amounts of noise and therefore results in a much more accurate measurement. The timer can preset the counting intervals from .1 minute to 50 minutes in a 1,2,5 sequence referenced to 60 Hz line frequency.

Calibration of Counter

The mini-scaler was calibrated with the sodium iodine scintillator and photomultiplier to optimize the performance of the radiation gauge. The following procedures were used to find the voltage, window width and threshold of the scaler to maximize the count rate.

1. H.V. adjust was turned to 0.00 and WINDOW IN-OUT was switched to IN.
2. Detector was exposed to gamma source Cs¹³⁷.
3. THRESHOLD was adjusted to 6.61. This corresponds to the 661 kev energy for Cs¹³⁷.
4. WINDOW was set to 25% of THRESHOLD, 1.65.
5. Counts vs high voltage was plotted (Figure 4.3a)
6. H.V. was adjusted for the peak reading.
7. To optimize window width, the curve of counts vs. window setting at THRESHOLD knob reading at 6.61 was plotted (Figure 4.3b). From the calibration curves, the optimal settings were found, 9.58 for H.V., 6.61 for THRESHOLD and 2.2 for WINDOW.

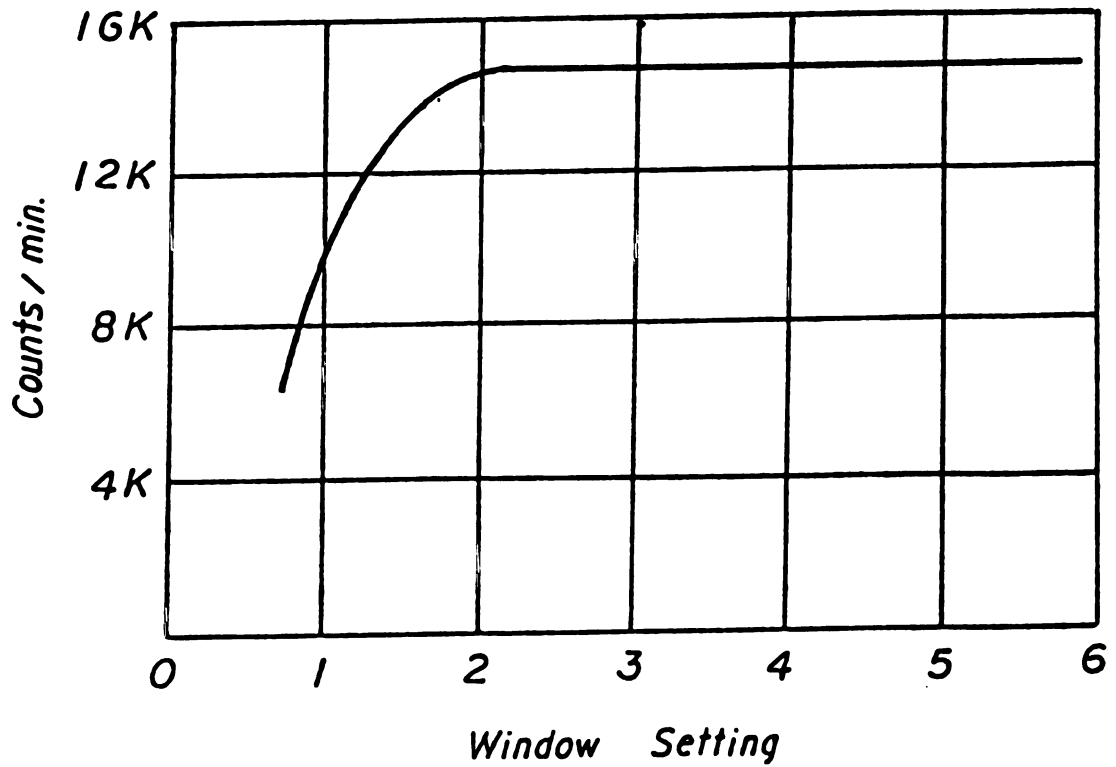
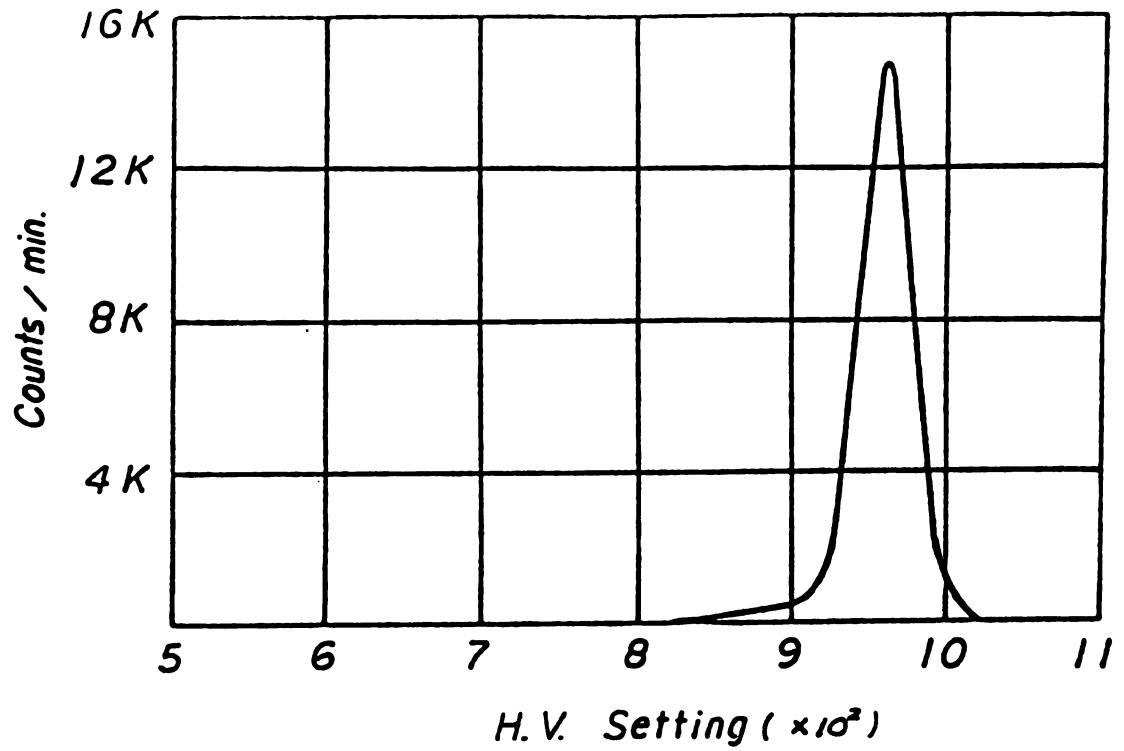


Figure 4.3 Calibration Curve for Radiation Counter

Radiation Gauge Arrangement

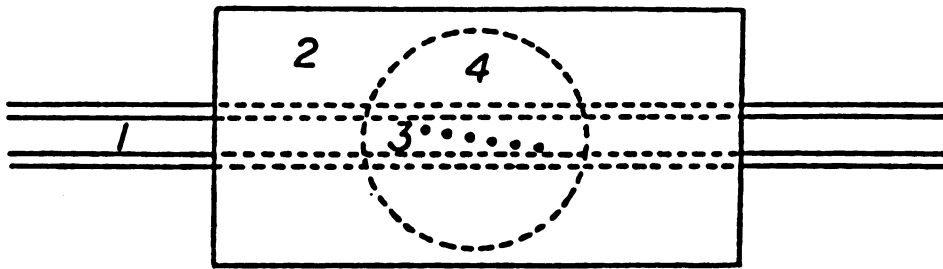
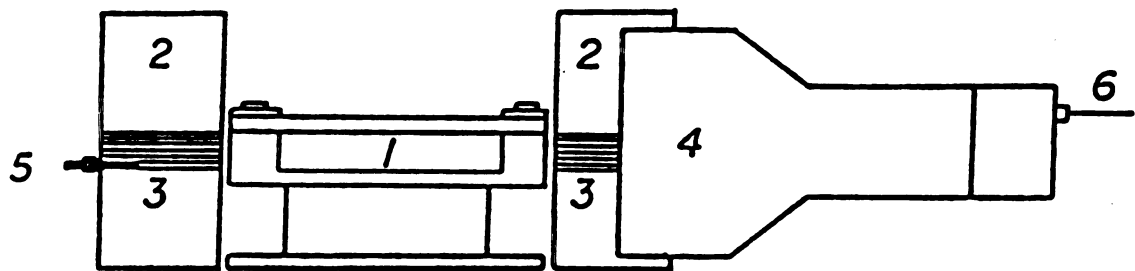
Figure 4.4 presents the side and end views of the radiation gauge used to make on-line density measurements in the test section. The gamma source, collimators (lead bricks) and the detector were rigidly fixed with respect to each other because the misalignment of the beam direction can cause a great error. Only one Cesium source was used in the experiment for various axial and transverse locations. The Cesium capsule was inserted successively into six holes drilled in a 10.16 cm thick shielding lead brick. Each hole has diameter .357 cm and was 2.54 cm long to accommodate the source. Inside the holes, channels of .12 cm diameter and 7.62 cm long were drilled so that the narrow collimated beams could be directed through these openings to penetrate the two-phase fluid. Four of these holes were positioned below the centerline at distances from the lower plate of .2 cm, .32 cm, .44 cm and .56 cm; the other two positioned above the centerline at distances of .28 cm and .4 cm from the upperplate and were used mainly to confirm the symmetry of the bubble concentration profile about the centerline (a case is shown in Appendix A). The detector was placed next to a 10.16 cm lead shielding brick, with drilled channels to collimate the beams reaching the detector. The locations of holes on either side were carefully aligned in order to avoid scattered beams reach the detector through other open channels.

FIGURE 4.4 Radiation Gauge Mounting

- a) Side View
- b) End View

The following numbers represent

- 1. Flow Channel
- 2. Lead Bricks
- 3. Gamma-ray Passes
- 4. Sodium Iodide Detector and Photomultiplier
- 5. Cesium Source
- 6. Signal to Counter

*a.**b.*

The difference in count rate due to the scattered γ -rays was found to be less than 2%. Therefore the effect of scattered rays was not included in the data analysis.

In between the source and detector, the flow channel was positioned on a wooden stand, 127 cm long, 12.7 cm wide and 14 cm high with guides on either side. The flow channel could be moved axially along guides on the stand to allow measurement of density at different axial locations. The channel movement in the axial direction does not affect the flow rate or entrance pressure.

Calibration of Gamma Attenuation

Equation (4,10) indicates that if density and mass attenuation coefficient of medium fluid (continuous phase) are known, the void fraction of the suspension can be calculated from the intensity ratio. Therefore, the mass attenuation coefficient has to be determined first from calibration. The coefficient differs from slot to slot, in which the γ -source was inserted, due to the difference in geometry of each slot. The flow channel was filled with corn syrup and Separan solutions in different compartments made of molding clay and then exposed the fluids to the source to calibrate their intensities and mass attenuation coefficients. The error in the reproducibility of intensity level was $\pm 10\%$ which was found due to the disturbance of moving the source. The count rate changed when the source was taken out of one

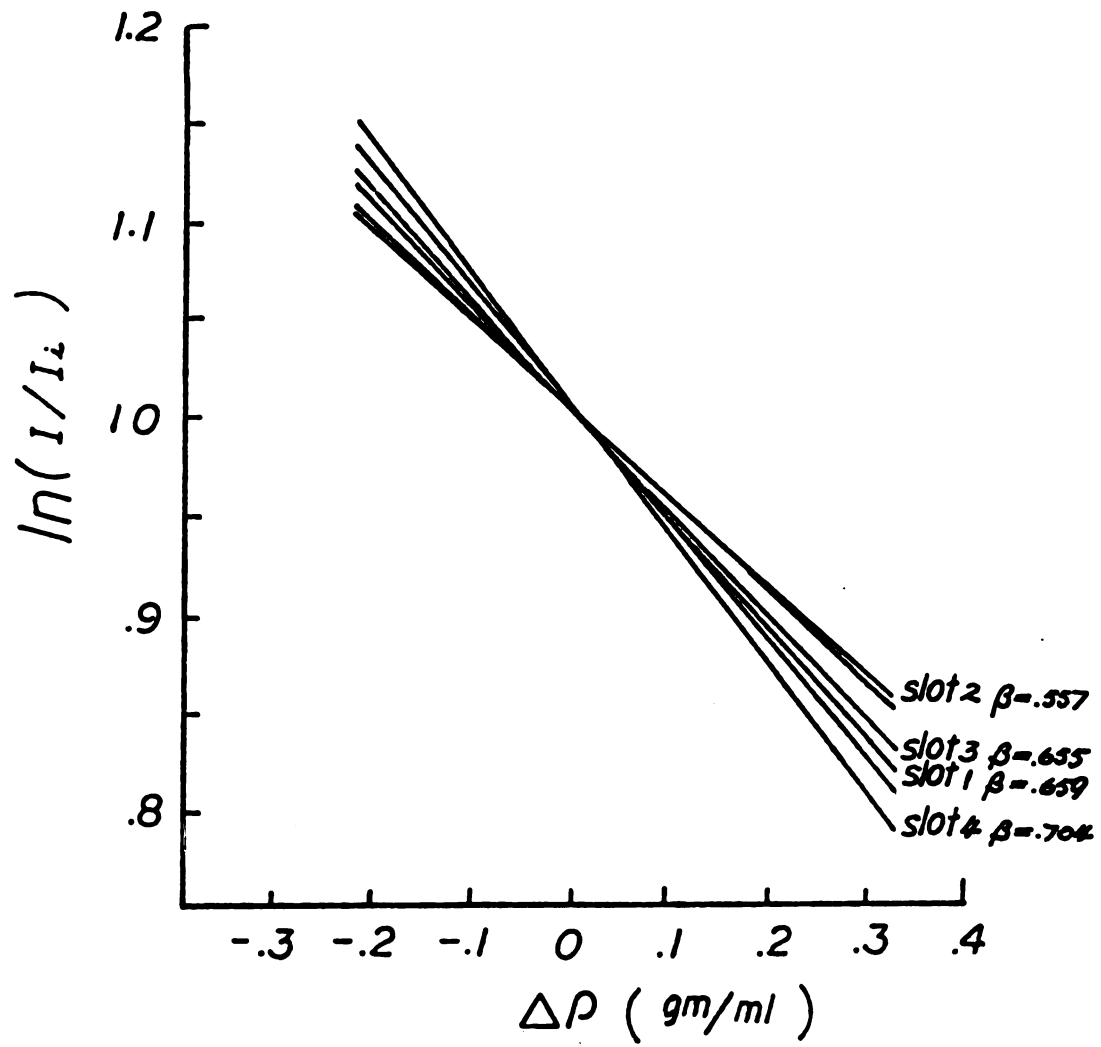


Figure 4.5 Linear Mass Attenuation
Coefficients

slot and then put back into the same slot. Therefore, the void fraction can not be calculated directly from relation (4,10) due to the inconsistent intensity. However, the relative density variation can be obtained by using relation (4,12), if the relative intensity ratio is reliable. In the system, the bubbles are uniformly distributed at the channel entrance, the void fraction then is identical to the bulk void fraction measured at the channel outlet. By fixing the radiation source in one location, the intensities were measured at the entrance and two axial locations. The intensity ratio of the downstream ones to the entrance one will be sufficient to determine the density variation. To search for the attenuation coefficient β , methanol-water mixture with densities in the range 0.9-1 g/cc, Separan solution and corn syrup were placed in cells made of molding clay. All these test solutions contain a great amount of water, so their mass attenuation coefficients are nearly the same, the slopes of Figure 4.5 show linear relations.

The attenuation coefficients ranged from 0.557 to 0.704 and were obtained for various slots. These coefficients were not affected by the movement of the source, even though the intensity changed.

Separan solution with density of 1 g/ml was chosen as the reference solution. The slope of each slot measured at different axial locations is consistent.

Discussion of Errors

In nature, all the high energy particles from radioisotope decay are random, associated with statistical fluctuations. The probability law indicates the uncertainty of the experimental observation of total number of counts, from an essentially infinite number of counts, is

$$\frac{\Delta Q}{Q} = \left(\frac{1}{Q} \right)^{\frac{1}{2}} \quad (4, 13)$$

When the total number of counts is small, the reliability of the result may be considerably different from the true value. One method to improve the accuracy of measurement is increasing the number of measurements. The detector background count is about 1% or 1.5% of the total count, it has to be subtracted out. If the background count is comparable to the same count, considerable error may be introduced. Counts should be recorded for enough time to obtain a resolution in density within one percent. In the experiment, twelve to sixteen measurements were taken with a mean value about 7500 ± 1000 counts/12 sec which varies with locations and fluids, $\pm .27\%$ to $.36\%$ error has to be considered. Since the density variation was calculated from the comparison between the measurements being made in the channel entrance and axial locations, therefore, the total error has to be doubled, $\pm .54\%$ to $.72\%$. The mass attenuation coef-

ficient was also determined from the radiation measurement, in which ten measurements were counted for each particular solution with a mean value of $17,500 \pm 2,000$ counts/24 sec., the statistical error lies from .23% to .25%. The propagation error is the sum of errors from these two independent measurements which is $\pm .77\%$ to $\pm .97\%$. The theoretical resolution of density detection is fairly satisfactory, by doubling number of measurements will reduce the error to $\pm .54\%$ or $\pm .69\%$, the improvement is insignificant compared to the efforts have to be put in. The resolution was also analyzed experimentally by sending corn syrup solution containing no bubbles through the flow channel and measuring the density profiles along the flow direction. The result (Figure 4.6) shows the fluctuation in density measurement is $\pm .01$ g/ml, which matches the theoretical prediction. The radiation attenuation method proves to be an effective means to detect the void fraction distribution in moving materials.

Procedure of Density Measurement

Density measurement consists of two portions, data collection and data analysis, the steps were conducted in the following sequence.

1. H.V. control, THRESHOLD, WINDOW WIDTH were adjusted to the calibrated setting to yield the optimal intensity level.

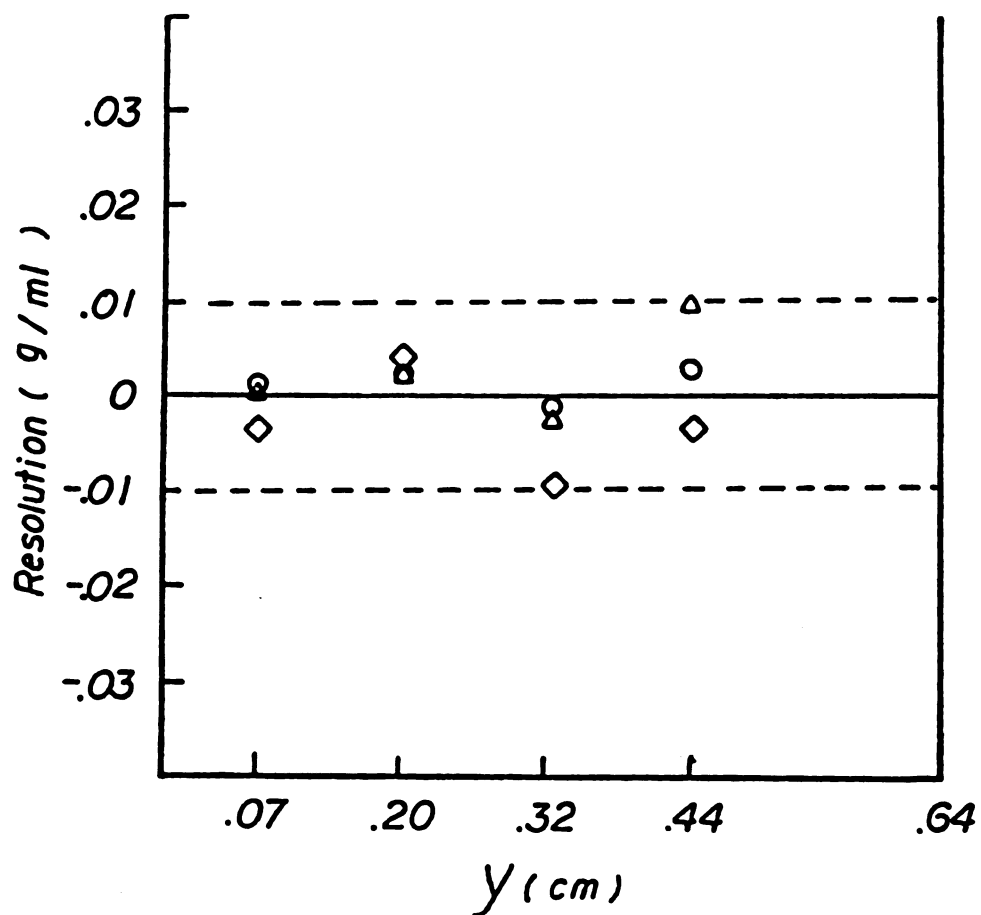


Figure 4.6 **Experimental Calibration for the Resolution of Radiation Gauge**

- 3 cm away from the entrance
- △ 22 cm away from the entrance
- ◇ 47 cm away from the entrance

2. Voltage supply to photomultiplier was turned on. Timer was set at 12 second position.
3. Background count was recorded to ensure that background "noise" was low.
4. Cesium 137 source was taken from its container and placed into the first hole.
5. Flow channel was adjusted such that the first axial location (3 cm away from the entrance) was exposed to gamma-rays.
6. Flow was started and steps for apparent viscosity measurement were carried out except the last one - measure the bulk density with pycnometer.
7. RESET-START bottom was pushed and counting started. Four to five count readings were recorded.
8. The channel was moved to a second and a third axial location, four to five count readings were recorded at each location.
9. The channel was moved back to its first location and the process repeated until twelve to sixteen readings were recorded for each location, so that data were collected evenly throughout the time span.
10. The source was shifted to the second hole and the steps from 5 to 9 were carried out. The process was repeated for the other holes.
11. The bulk density was measured and thus assumed this density represent a uniform transverse density at the

entrance (first axial location).

The group of collected counts often has some members deviating greatly from the mean. Thus the choice had to be made to keep or to reject there. These particular observations are not necessarily wrong but the deviations may have an significant influence on the mean value that is computed. Chauvenet established a criterion which considered the magnitude of deviation and number of observations made. The rejection of the datum is allowed if the datum lies outside the $(1 - \frac{1}{2Q}) \times 100\%$ confidence region, Q is the total number of observations. After screening questionable data, a new mean value is calculated, the criterion may be applied to the remaining data. One example is shown in Appendix B to demonstrate the procedures of obtaining axial and transverse void fractions.

CHAPTER 5

VOID FRACTION PROFILES IN VISCOELASTIC FLUIDS

Void fraction profiles observed in flowing gas bubble suspensions with corn syrup and aqueous Separan solutions as media are presented in this chapter, for a range of wall shear stresses and flow rates. The causes of bubble migration in non-Newtonian fluids undergoing plane Poiseuille flow are then discussed, along with conditions for a two-phase flow structure with a uniform core and a uniform wall layer.

Bubble rise and bubble growth are not significant in our study, as discussed in Chapter 3. The bubble rise time is 20 times longer than the maximum residence time and photographs taken at different axial locations and times show bubble sizes of 0.4 to 0.6 mm throughout. Void fraction profiles obtained with corn syrup, 2.5 wt percent and 3.5 wt percent aqueous Separan solutions are shown in Figure 5.1 to 5.32. In each figure, the profile at an axial location of 18 cm from the entrance, denoted by \circ is compared with that at 47 cm from the entrance, denoted as Δ . The coordinate y is the distance from the centerline of the channel. Since the profiles are symmetric, only half of the gap is plotted in these figures. Each density measurement in these figures represents the average over a region of diameter equal to a tenth of the gap dimension in the flow plane. The average

axial velocity, denoted by $\langle U \rangle$ and the bulk void fraction ϕ are specified in each figure.

5.A Profiles in Corn Syrup

Figures 5.1 to 5.9 show that in the Newtonian corn syrup, bubbles are uniformly distributed across the gap at both axial locations with different values of bulk void fraction and flow rate. The scatter of data about the bulk void fraction is due to the statistical error of radiation measurement. The applied wall shear stresses are above 32 N/m^2 , which is an empirical value reported by Prud'homme (1978), beyond which, he observed bubble migration. The data show that the "tubular pinch effect" due to inertia - observed by Segré et al. (1962) does not occur at Reynolds numbers considered here. The "tubular pinch effect" involves crossflow migration of suspended particles toward an equilibrium position at a distance of 0.6 radius from the flow axis at moderate or high Reynolds number (Ho and Leal (1974)). Reynolds numbers based on gap dimension ($Re_h = \rho \langle U \rangle h / \eta$) are of order 10^{-3} and bubble Reynolds numbers ($Re_p = \rho \langle U \rangle a / \eta$) are of order 10^{-4} , so that inertia effects are indeed negligible. The other factor which might cause crossflow migration of particles suspended in a Newtonian medium is shape distortion, the extent of which is governed by the capillary number τ/η and the ratio of viscosities η/η' , where η, η' are the viscosities of suspending medium and suspended par-

ticle, G is the average rate of strain, σ is the interfacial tension. When the capillary number is very small, the bubbles remain spherical irrespective of the viscosity ratio. The observation of uniform void fraction across the gap with corn syrup would suggest that there is very little shape distortion. This is confirmed by photographs taken of the flowing suspension in corn syrup. Also, the capillary number is found to be between 0.1 and 0.2 for all runs made with the corn syrup system. Bounded walls also cause crossflow migration, but this wall effect is negligible with the ratio of bubble diameter to slit dimension $2a/h=0.03 \ll 1$.

The properties presented in Table 3.1 for both polymer solutions indicate the Reynolds numbers as well as the capillary numbers are of comparable magnitudes for all three media so that the factors of inertia and viscous shape distortion of bubbles may be ruled out in all cases. Thus, any crossflow migration observed in the polymer solutions must be due to non-Newtonian effects - viz. the gradient of normal stresses around the bubble (cf. Chan and Lean (1979)) and pseudoplastic effect (cf. Gauthier, et al., (1971)). The interpretation of the data in the light of these two effects is discussed after presenting the trends in void fraction profiles with the polymer solutions.

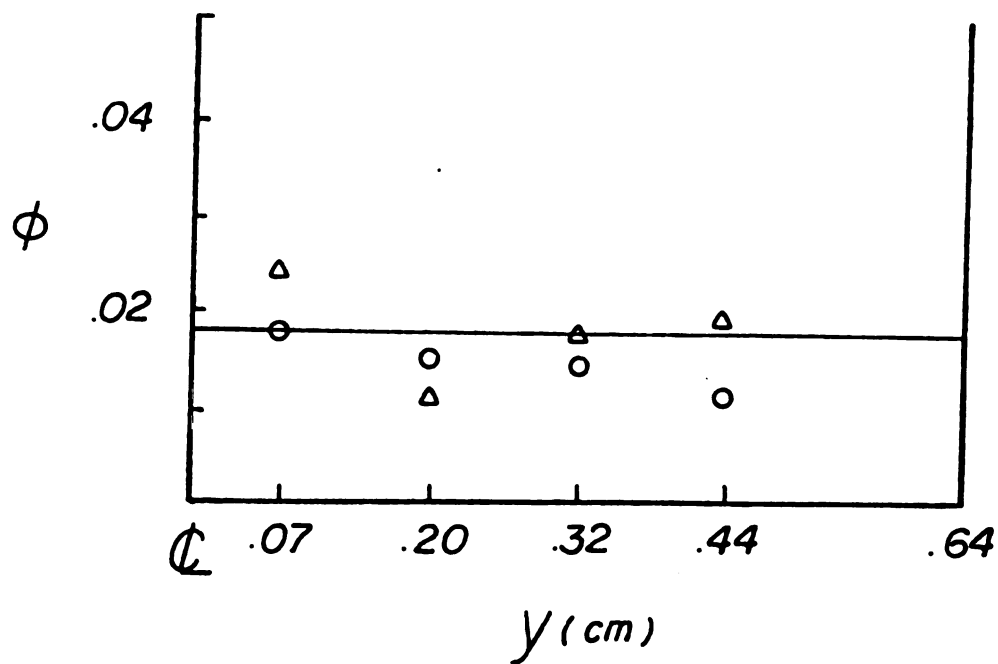


Figure 5.1 Void Fraction Profile With Corn Syrup

$$\phi_b = .018, \langle u \rangle = .65 \text{ cm/sec}$$

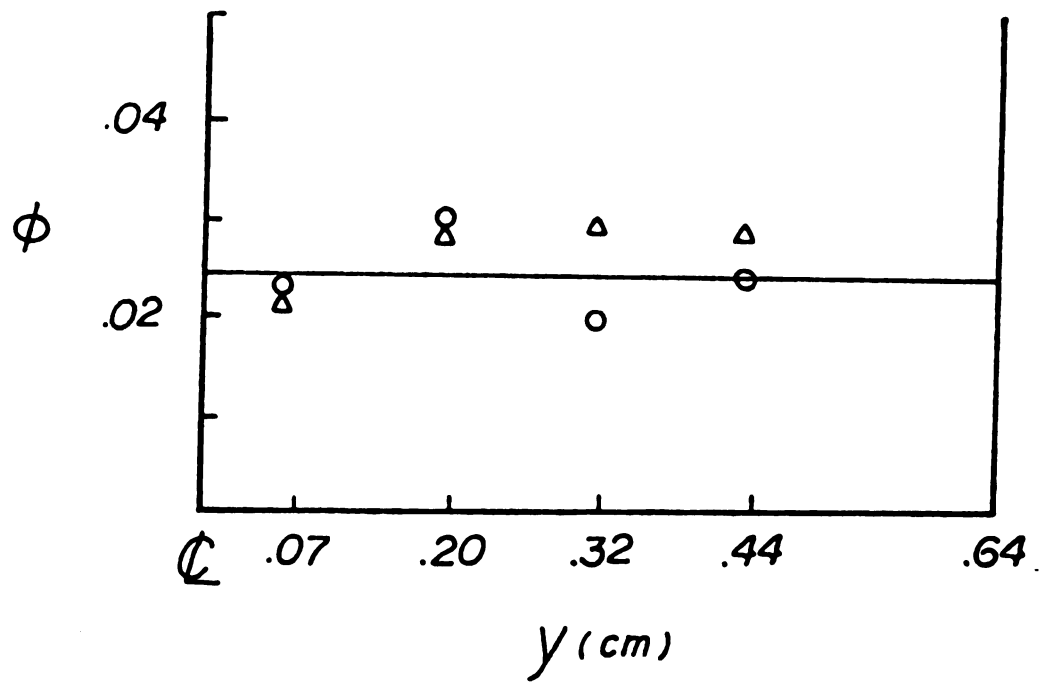


Figure 5.2 Void Fraction Profile With Corn Syrup

$$\phi_b = .024, \quad \langle U \rangle = .54 \text{ cm/sec}$$

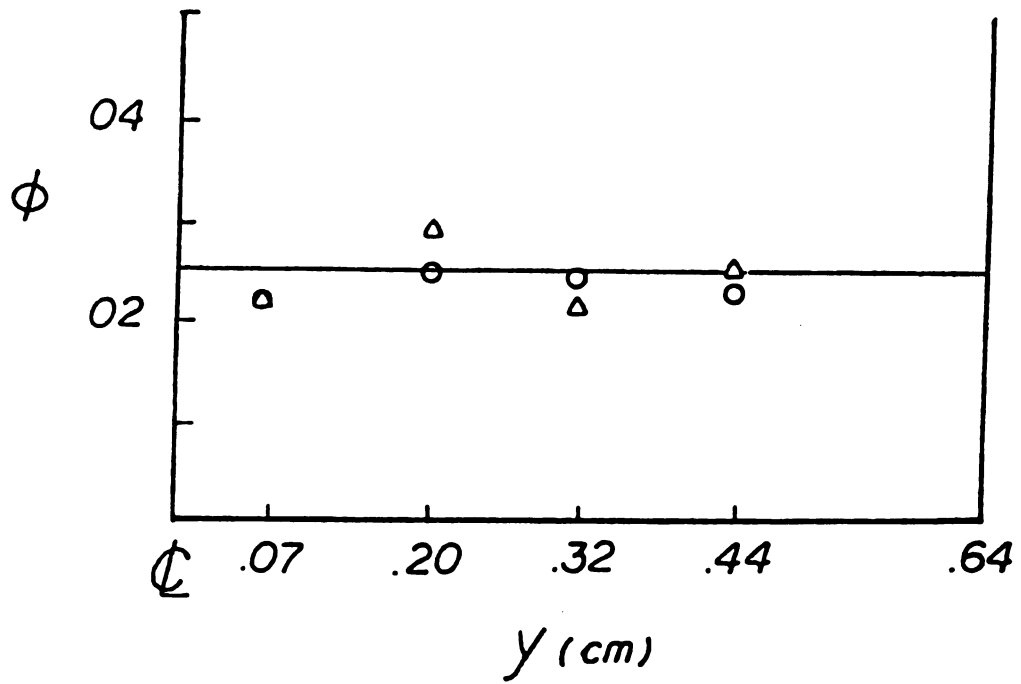


Figure 5.3 Void Fraction Profile With Corn Syrup

$$\phi_b = .025, \quad \langle u \rangle = .46 \text{ cm/sec}$$

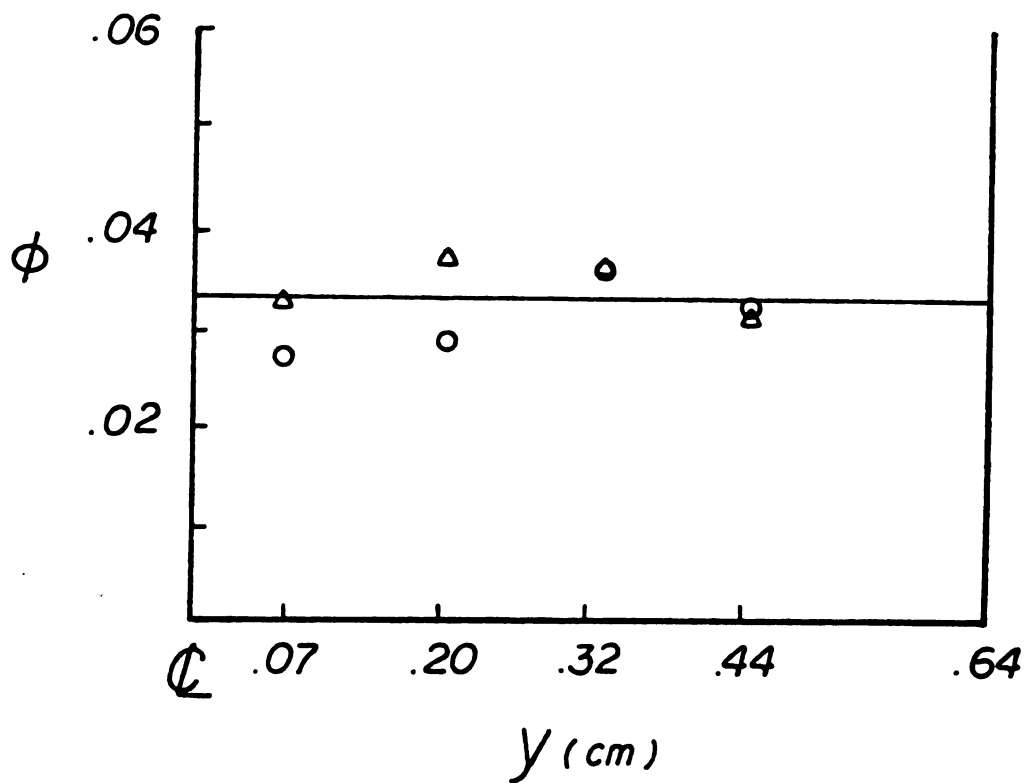


Figure 5.4 Void Fraction Profile With Corn Syrup

$$\phi_b = .033, \quad \langle v \rangle = .88 \text{ cm/sec}$$

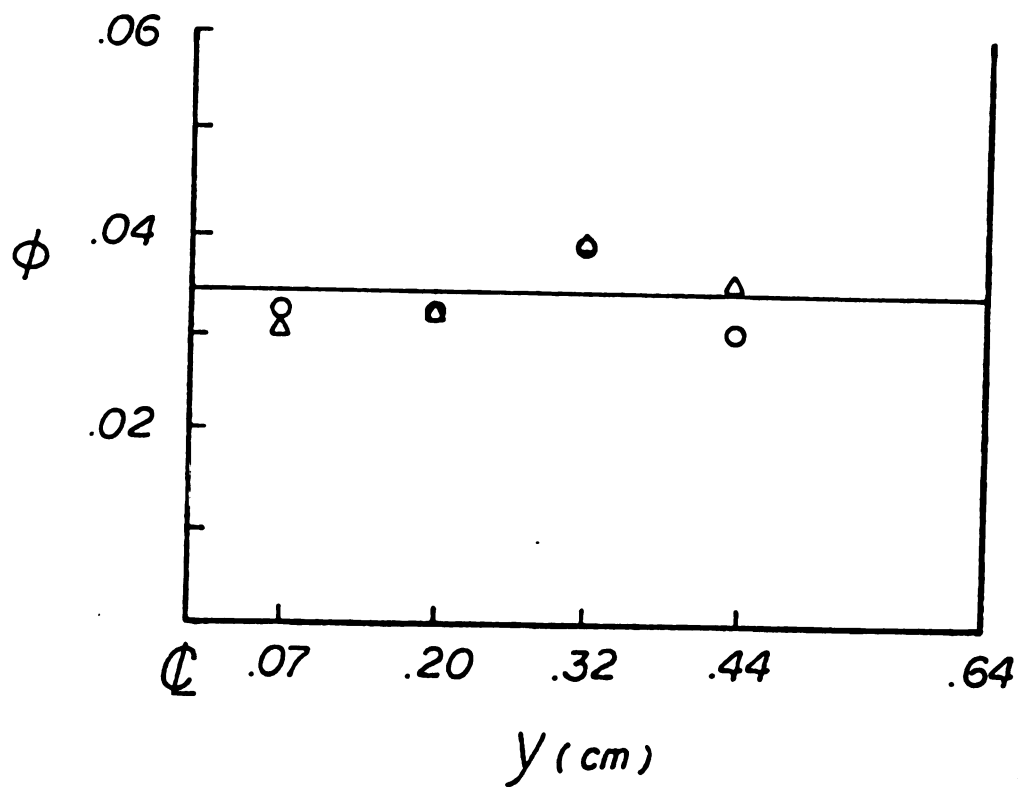


Figure 5.5 Void Fraction Profile With Corn Syrup

$$\phi_b = .034, \langle v \rangle = .74 \text{ cm/sec}$$

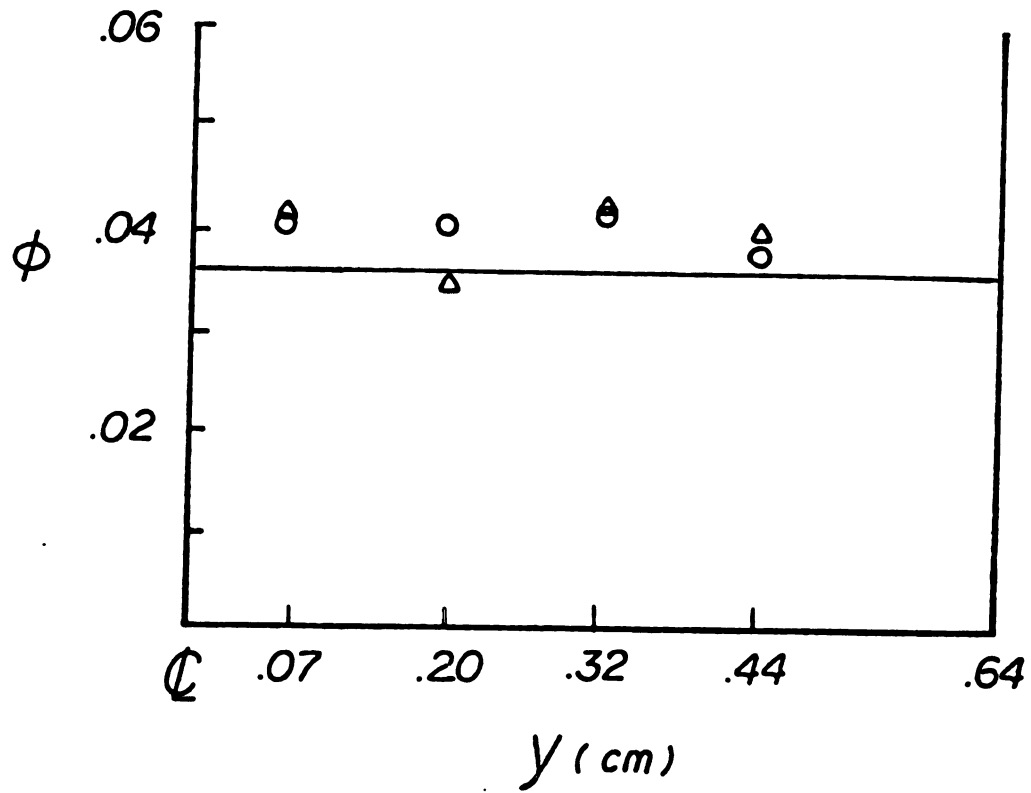


Figure 5.6 Void Fraction Profile With Corn Syrup

$$\phi_b = 0.036, \quad \langle U \rangle = 0.59 \text{ cm/sec}$$

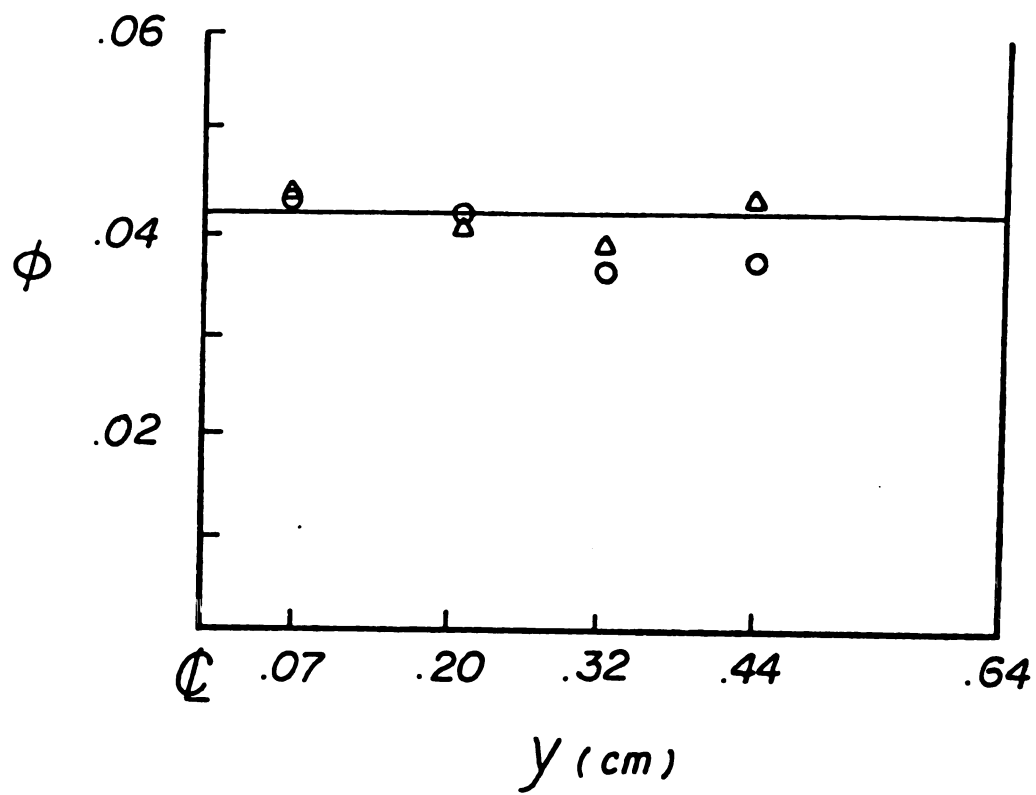


Figure 5.7 Void Fraction Profile With Corn Syrup

$$\phi_b = .042, \quad \langle u \rangle = .39 \text{ cm/sec}$$

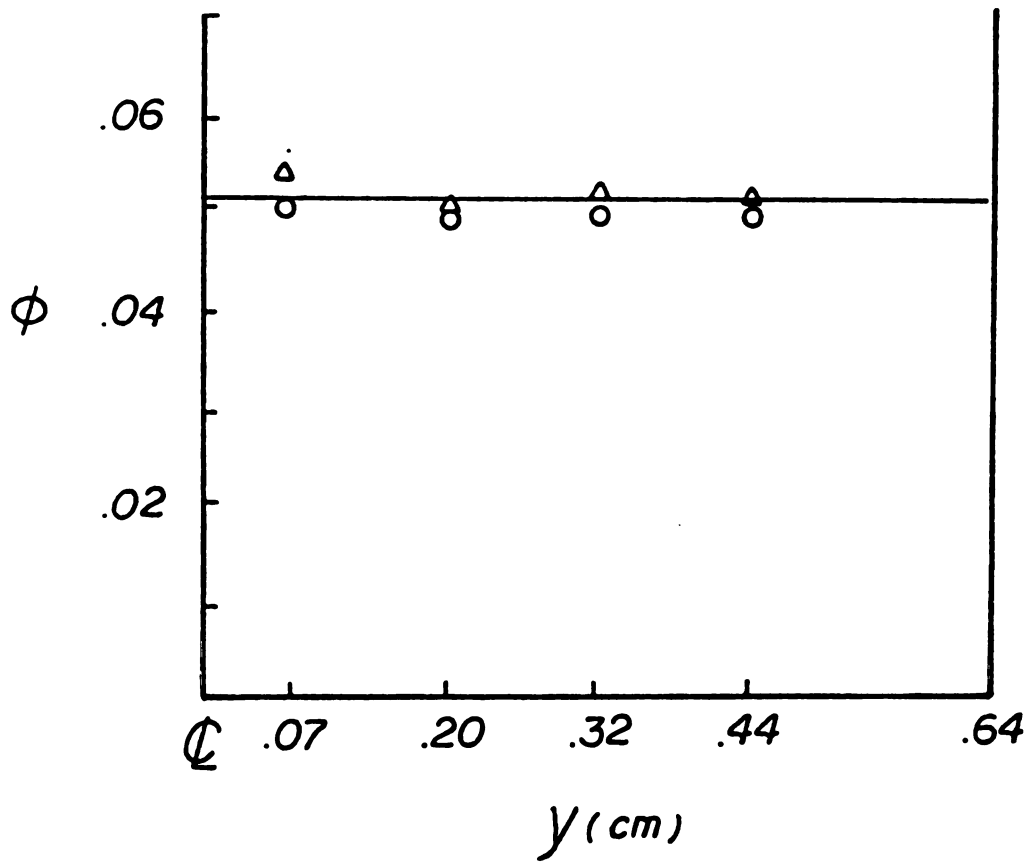


Figure 5.8 Void Fraction Profile With Corn Syrup

$$\phi_0 = .051, \quad \langle v \rangle = .62 \text{ cm/sec}$$

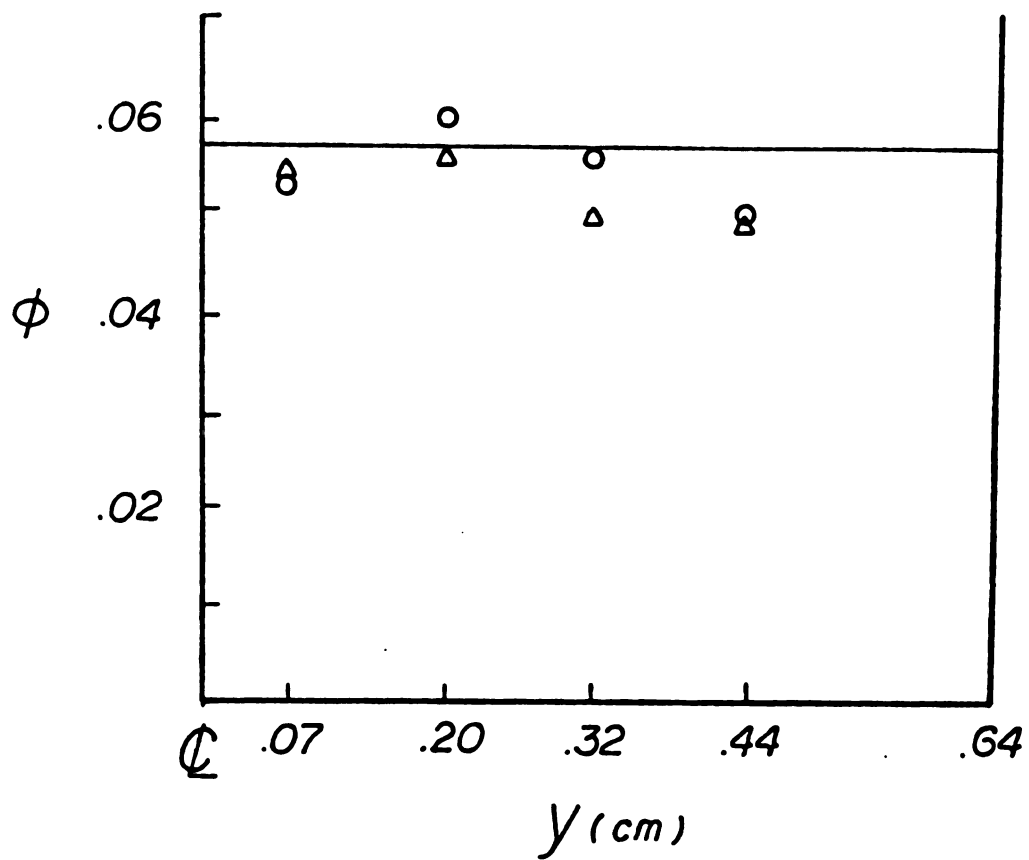


Figure 5.9 Void Fraction Profile With Corn Syrup

$$\phi_0 = .058, \quad \langle u \rangle = .77 \text{ cm/sec}$$

5.B Profiles in 2.5 wt. Percent Separan Solution

Void fraction profiles measured with the 2.5 wt. per-cent Separan solution are presented in Figures 5.10 to 5.20. The profiles indicate that bubble migration is toward the centerline of flow channel; the number of bubbles decreases next to the wall. The development of the void fraction profile is quicker at higher flow rates and higher void fractions. For instance, at an average linear velocity of 0.82 cm/sec and a bulk void fraction of 0.02 (Figure 5.11), the downstream profile is sharply peaked at the center while the upstream profile shows little change from the uniform bulk at entrance. As the bulk void fraction is increased to 0.032 with the same average linear velocity (Figure 5.15), both upstream and downstream profiles are seen to be peaked, the downstream one being sharper. With about the same void fraction $\phi_b = 0.034$ (Figure 5.18), the upstream profile is nearly uniform as the entrance profile, but downstream profile develops into one that may be presented by a uniform bubbly core and a bubble free wall layer. Similar trend can be observed in Figures 5.13, 5.14 and 5.19, where the average linear velocity is about .55 cm/sec. As void fraction increases from 0.024 to 0.035, the void fraction profile develops from a peaked one to one that may be presented by a uniform core at downstream locations. With the same void fraction, for instance, $\phi_b = 0.032$ (Figure 5.15), as the

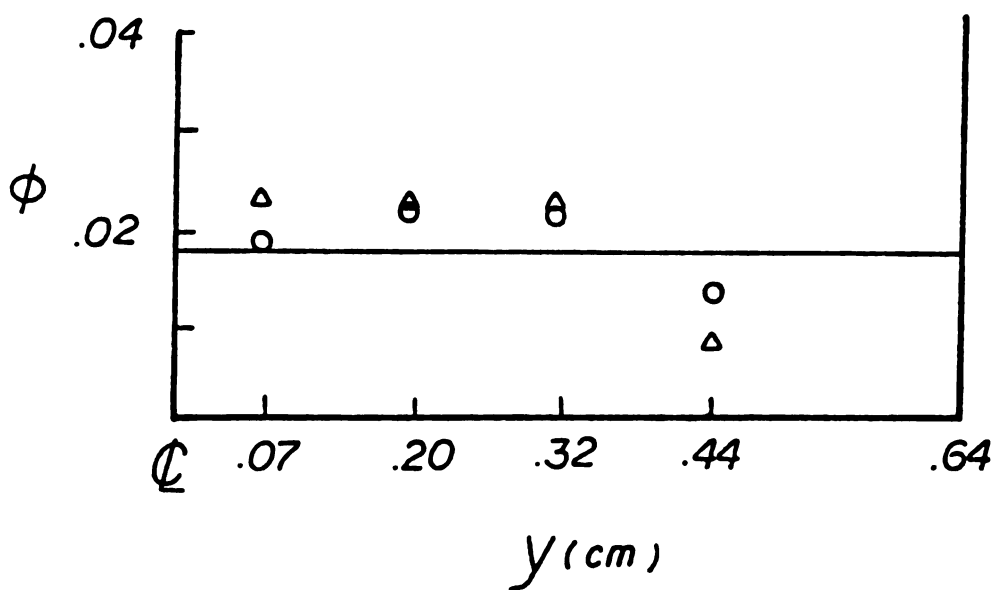


Figure 5.10 Void Fraction Profile With 2.5 wt Percent Separan Solution

$$\phi_0 = 0.018, \quad \langle v \rangle = 0.7 \text{ cm/sec}$$

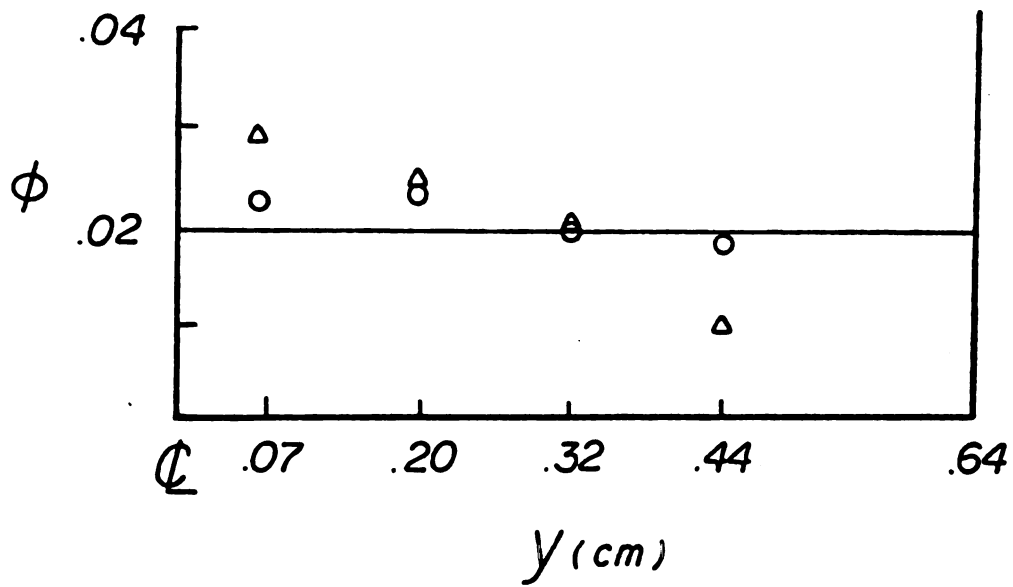


Figure 5.11 Void Fraction Profile With 2.5 wt Percent Separan Solution

$$\phi_b = .02, \quad \langle v \rangle = .82 \text{ cm/sec}$$

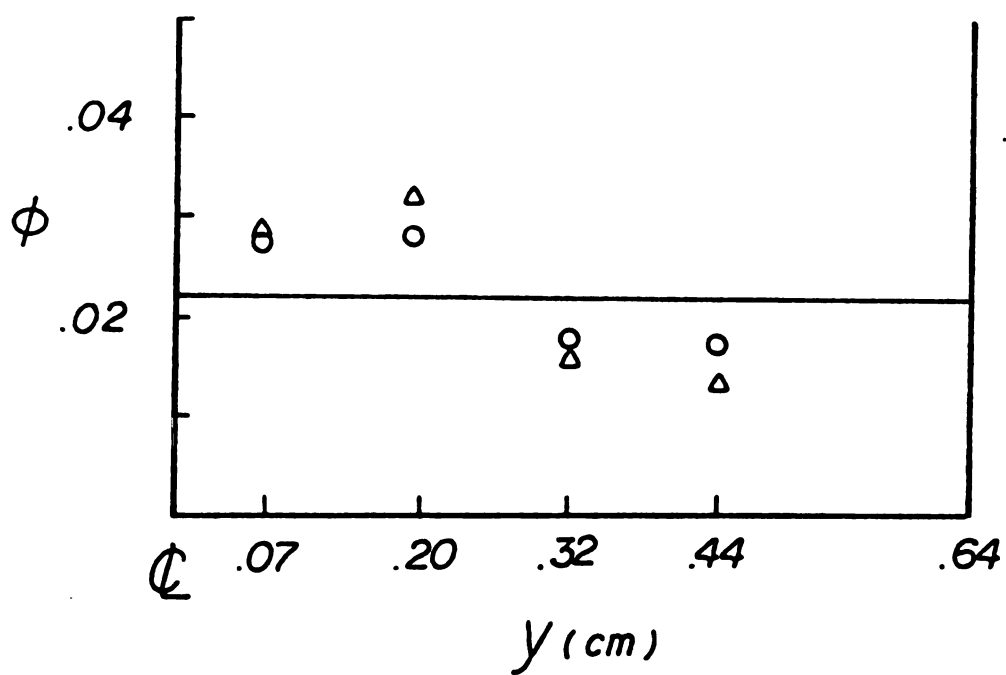


Figure 5.12 Void Fraction Profile With 2.5 wt Percent Separan Solution

$$\phi_b = .022, \quad \langle v \rangle = .4 \text{ cm/sec}$$

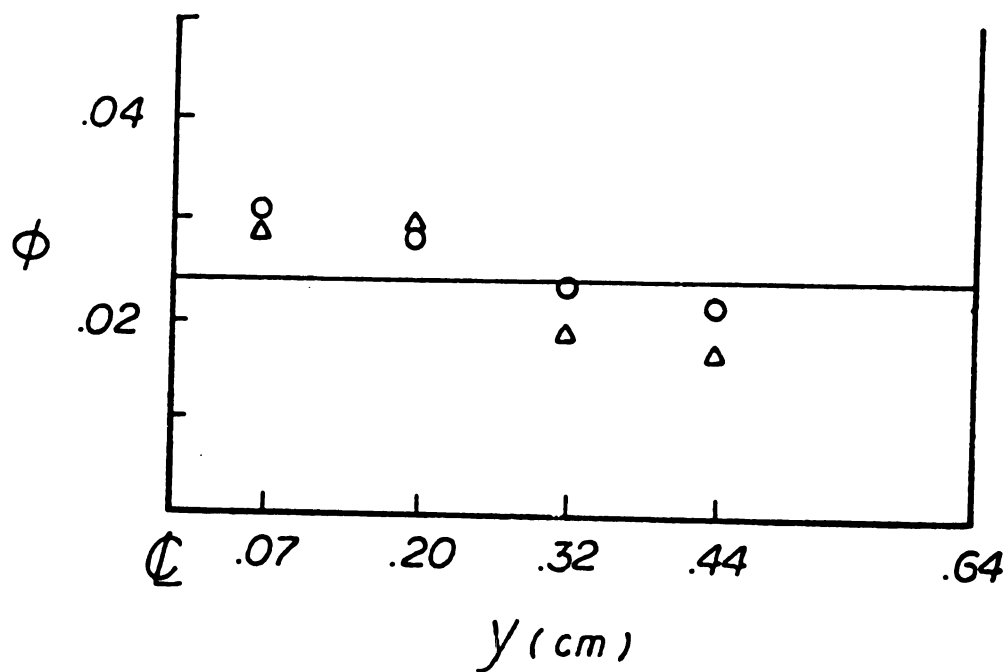


Figure 5.13 Void Fraction Profile With 2.5 wt Percent Separan Solution

$$\phi_b = .024, \quad \langle u \rangle = .58 \text{ cm/sec}$$

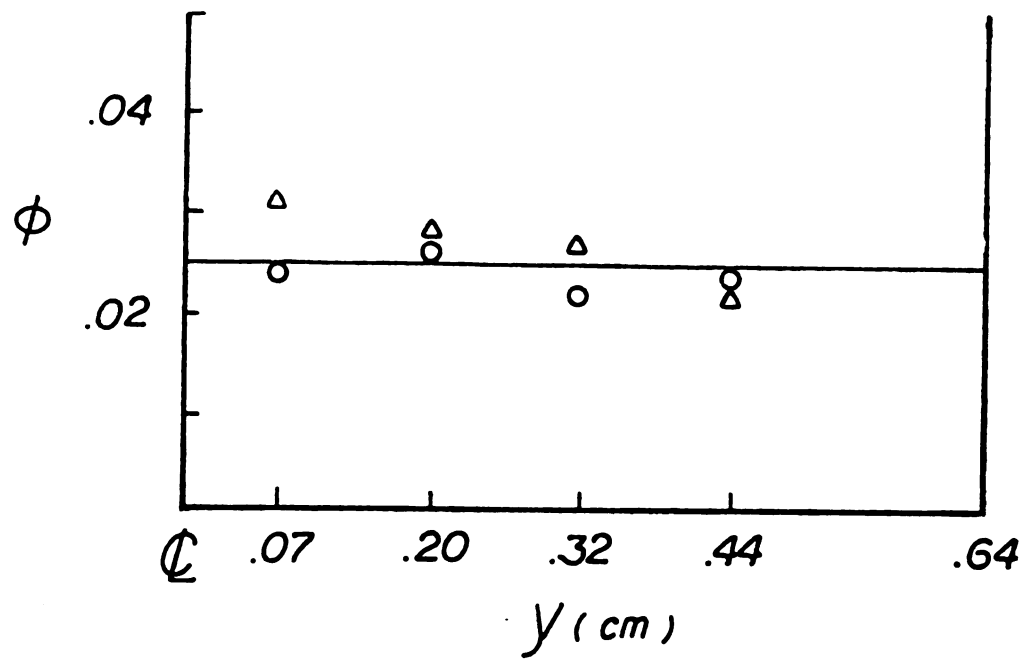


Figure 5.14 Void Fraction Profile With 2.5 wt Percent Separan Solution

$$\phi_0 = 0.025, \quad \langle v \rangle = 0.54 \text{ cm/sec}$$

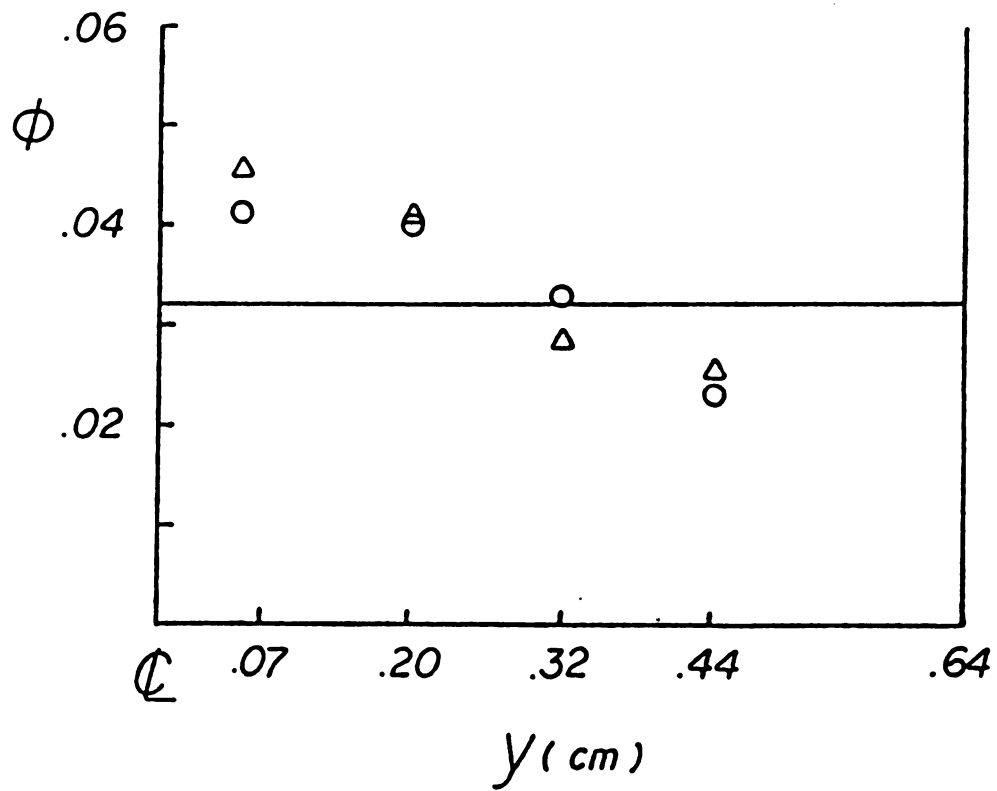


Figure 5.15

Void Fraction Profile With 2.5 wt
Percent Separan Solution

$$\phi_b = .032 \quad , \quad \langle U \rangle = .78 \text{ cm/sec}$$

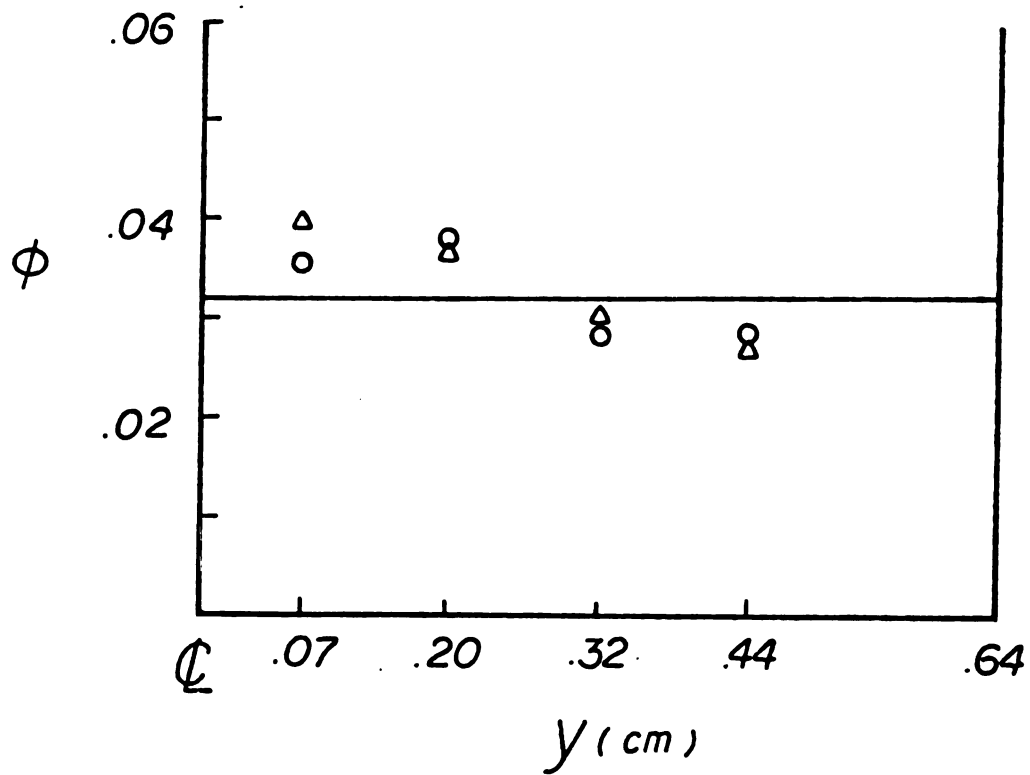


Figure 5.16 Void Fraction Profile With 2.5 wt Percent Separan Solution

$$\phi_b = 0.032, \quad \langle U \rangle = 1.17 \text{ cm/sec}$$

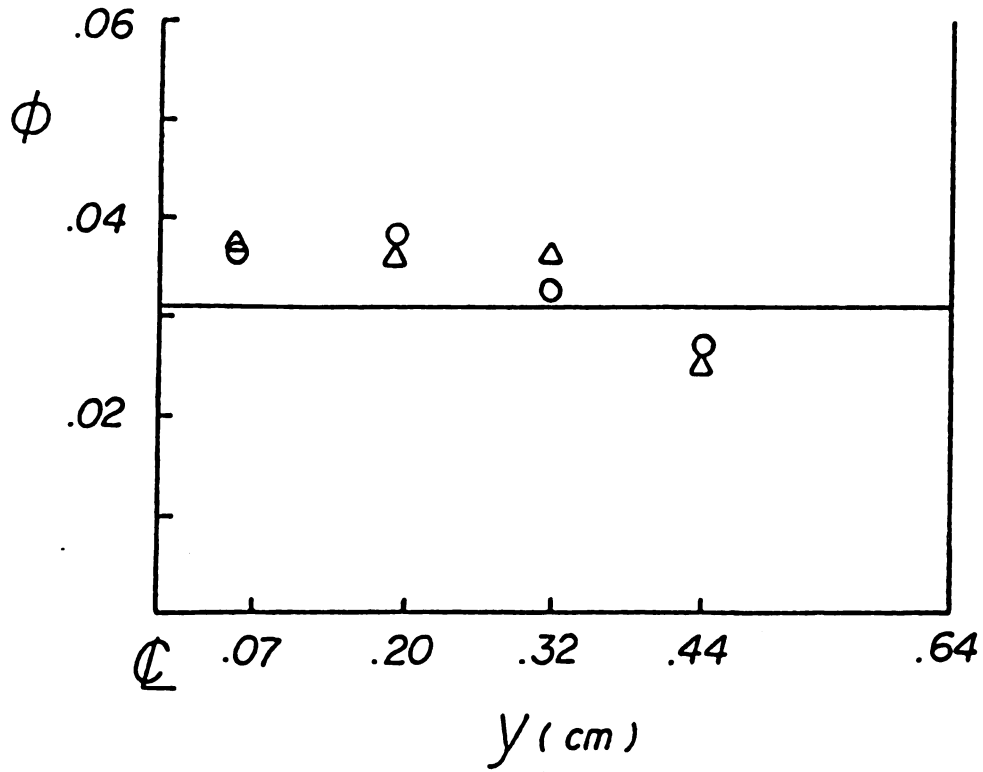


Figure 5.17 Void Fraction Profile With 2.5 wt Percent Separan Solution

$$\phi_b = .031 \quad \langle U \rangle = 1.18 \text{ cm/sec}$$

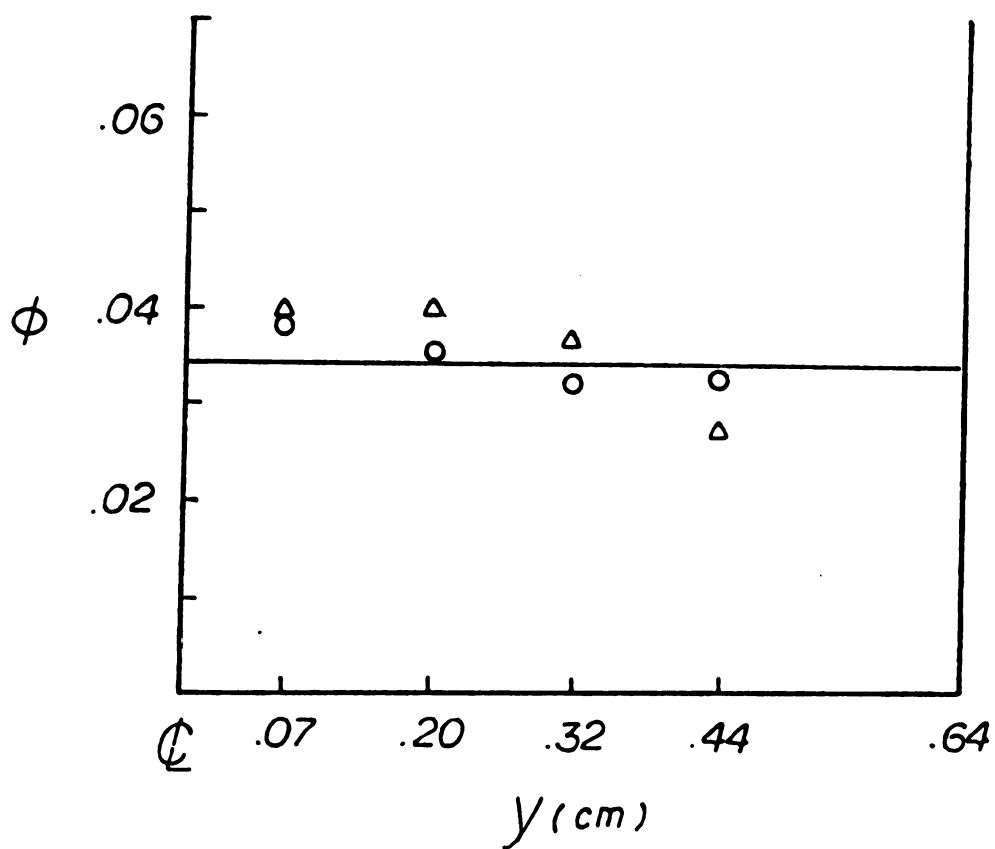


Figure 5.18 Void Fraction Profile With 2.5 wt Percent Separan Solution

$$\phi_b = .034 \quad \langle U \rangle = .81 \text{ cm/sec}$$

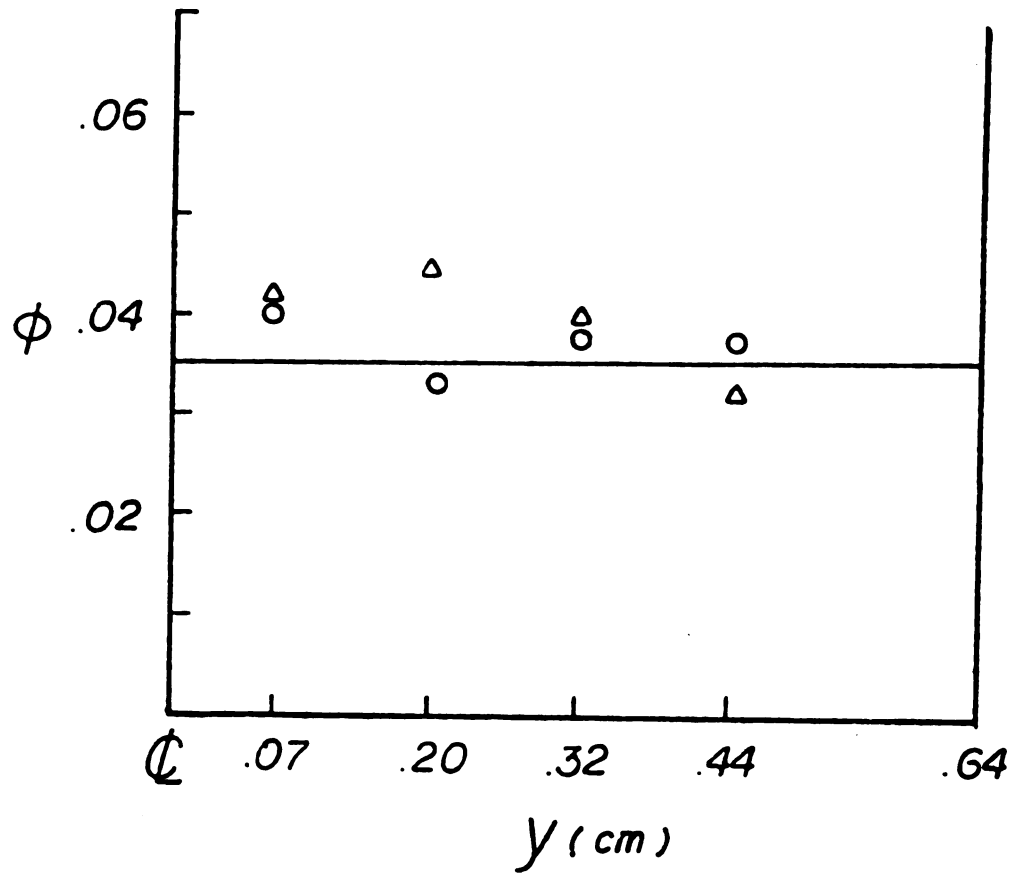


Figure 5.19 Void Fraction Profile With 2.5 wt Percent Separan Solution

$$\phi_b = .035, \quad \langle v \rangle = .6 \text{ cm/sec}$$

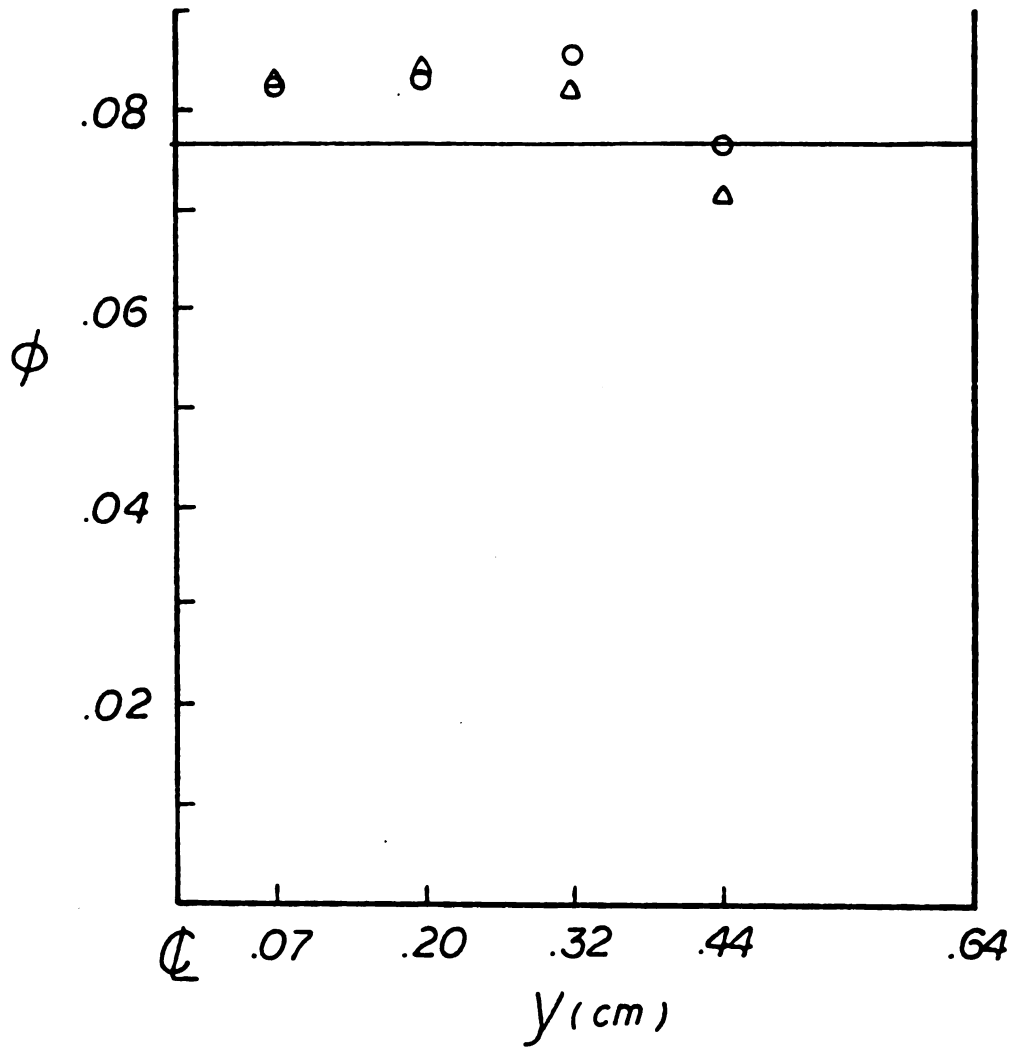


Figure 5.20 Void Fraction Profile With 2.5 wt Percent Separan Solution

$$\phi_b = .077, \quad \langle v \rangle = 1.38 \text{ cm/sec}$$

average linear velocity increases from 0.78 cm/sec to 1.18 cm/sec (Figures 5.16, 5.17), the void fraction at both axial locations develops into a uniform bubbly core and a wall layer. With high bulk void fraction and high flow rate, the uniform core develops much faster and is observed at both upstream and downstream locations (e.g. Figure 5.24). The reproducibility of void fraction profile is satisfactory (see Figures 5.13 and 5.14, Figures 5.16 and 5.17), the shapes are consistent within the experimental error.

5.C Profiles in 3.5 wt Percent Separan Solution

The void fraction profiles of bubble suspensions in 3.5 wt percent Separan solution are presented in Figures 5.21 to 5.32. In the case where the flow rate is very low (Figures 5.29 and 5.28), the bubble migration can still be observed, confirming that even very weak elastic forces can overcome the shear forces and contribute to crossflow migration towards the centerline of the channel. With the same void fraction, as the flow rate increases, the profile develops into a peak one or one with a uniform core. For instance, with bulk void fraction about 0.035, at average linear velocity 0.32 cm/sec (Figure 5.22), the profiles at upstream and downstream locations do not deviate from the uniform entrance profile much, the migration is very slow. As average linear velocity increases to 0.91 cm/sec (Figure 5.23), the upstream and downstream profiles become peaked, as the velocity in-

creases further to 1.5 cm/sec (Figure 5.24), both upstream and downstream profiles indicate core - annular flow. The core void fraction is increased in the downstream location compared to the upstream one, which means the core thickness is narrower with increasing flowrate. Similar trends can be observed in the cases of bulk void fraction of 0.043 (Figures 5.27 and 5.26), with increasing flow rate, the uniform core gets narrower at downstream location. With the same average linear velocity, the formation of uniform core is enhanced by the increasing bulk void fraction. For instance, with average linear velocity about 0.8 cm/sec (Figure 5.23), at bulk void fraction of 0.026. (Figure 5.21), the profile of upstream shows little change from the uniform bulk at entrance, the profile of downstream is peaked. As bulk void fraction increases to 0.035 (Figure 5.23), profiles at both upstream and downstream locations are peaked. As bulk void fraction increases further to 0.056 (Figure 5.31), the profiles at upstream and downstream locations are both uniform near the centerline. The downstream profile is narrower than the upstream one. With similar bulk void fraction and flow rate, the bubble migration effect in 3.5 wt percent Separan solution is more significant than that in 2.5 wt percent Separan solution (cf. Figures 5.16 and 5.23). The core thickness is narrower in the 3.5 wt percent Separan solution (Figure 5.26) than that of 2.5 wt percent Separan solution (Figure 5.17). The void fraction profiles develop

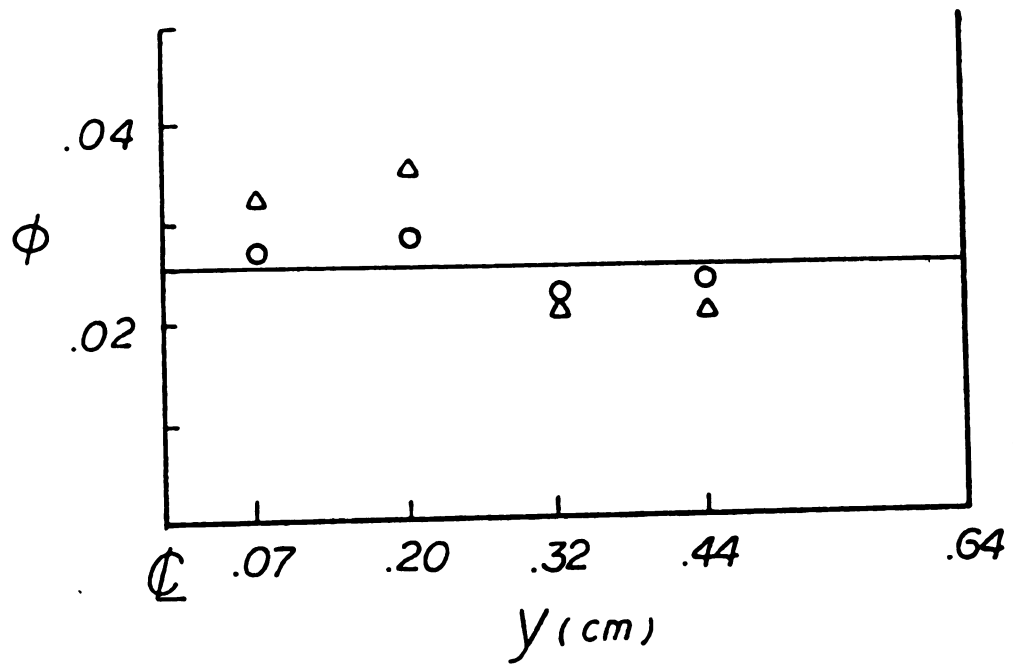


Figure 5.21 Void Fraction Profile With 3.5 wt Percent Separan Solution

$$\phi_b = .026, \quad \langle v \rangle = .93 \text{ cm/sec}$$

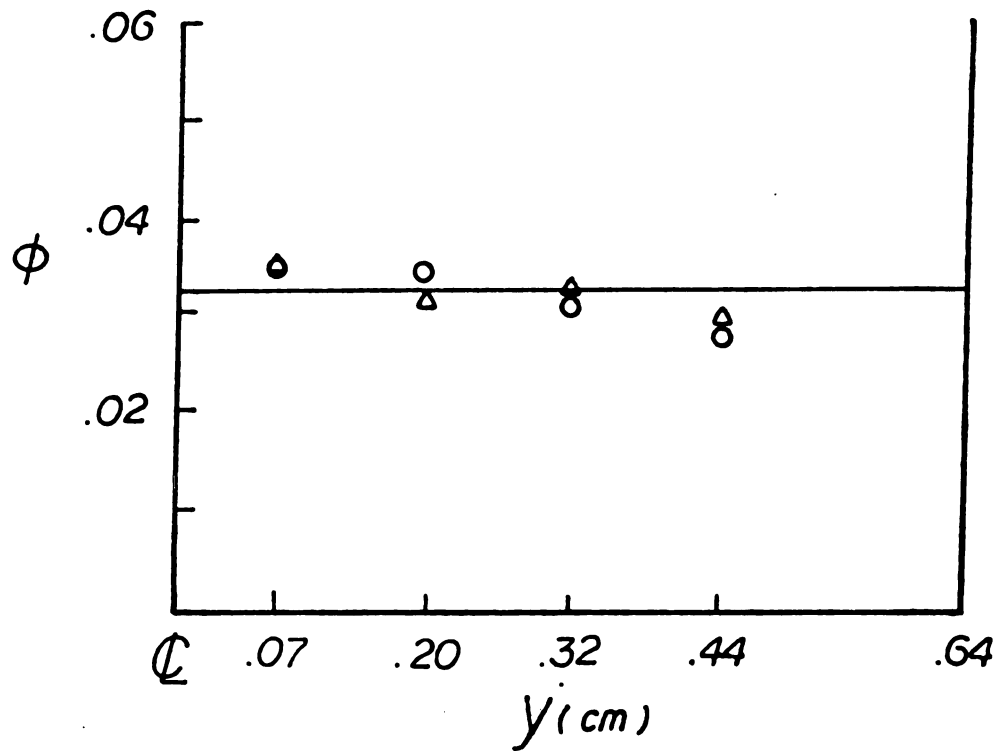


Figure 5.22 Void Fraction Profile With 3.5 wt Percent Separan Solution

$$\phi_b = .032, \quad \langle u \rangle = .32 \text{ cm/sec}$$

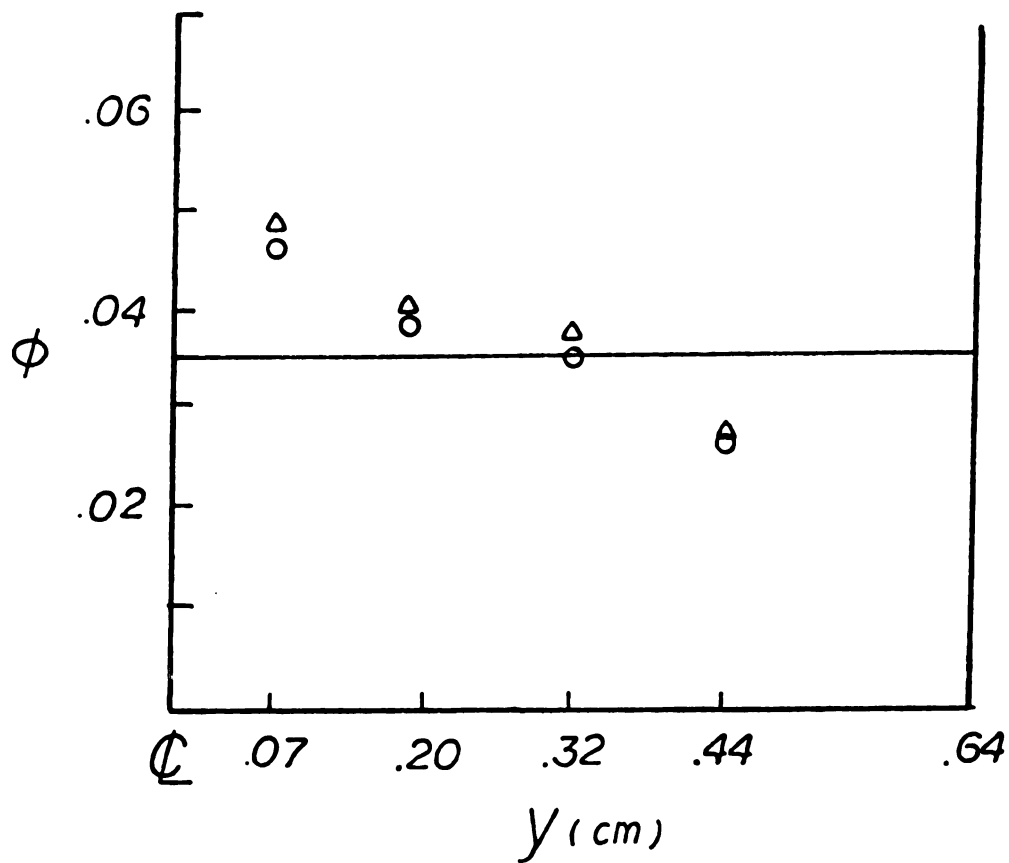


Figure 5.23 Void Fraction Profile With 3.5 wt Percent Separan Solution

$$\phi_b = 0.035, \quad \langle v \rangle = 0.91 \text{ cm/sec}$$

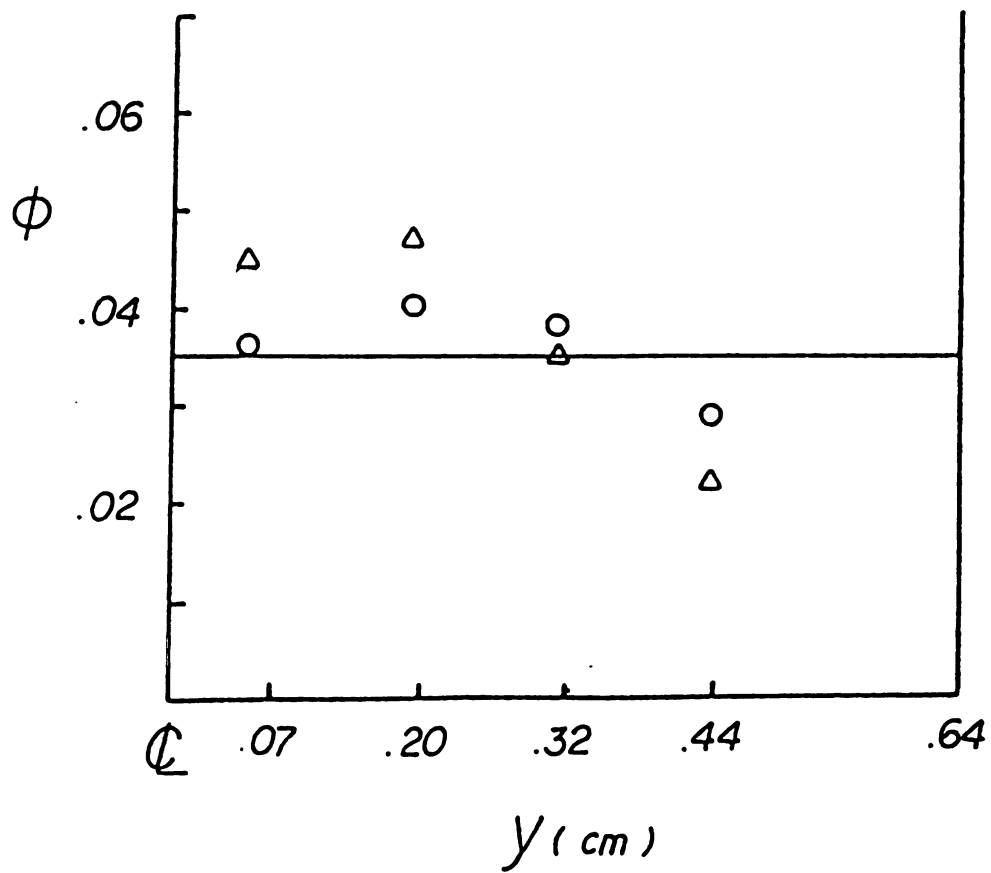


Figure 5.24 Void Fraction Profile With 3.5 wt Percent Separan Solution

$$\phi_b = .035, \quad \langle U \rangle = 1.5 \text{ cm/sec}$$

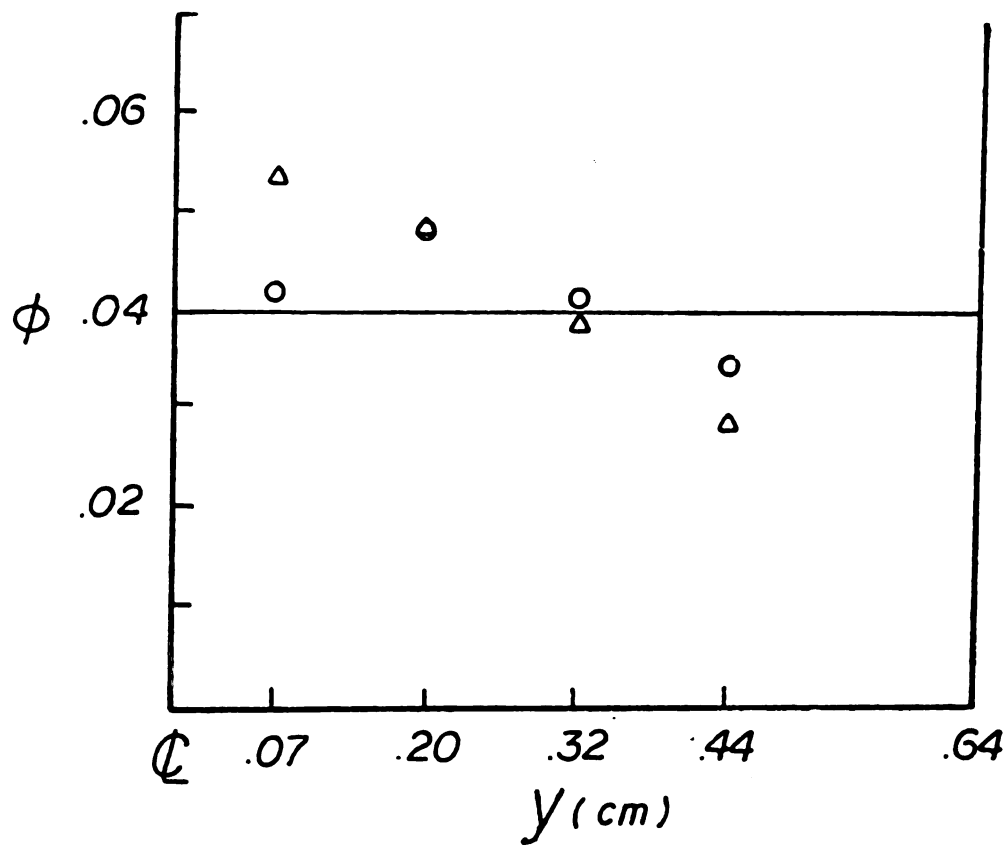


Figure 5.25 Void Fraction Profile With 3.5 wt Percent Separan Solution

$$\phi_b = .04 \quad , \quad \langle v \rangle = .82 \text{ cm/sec}$$

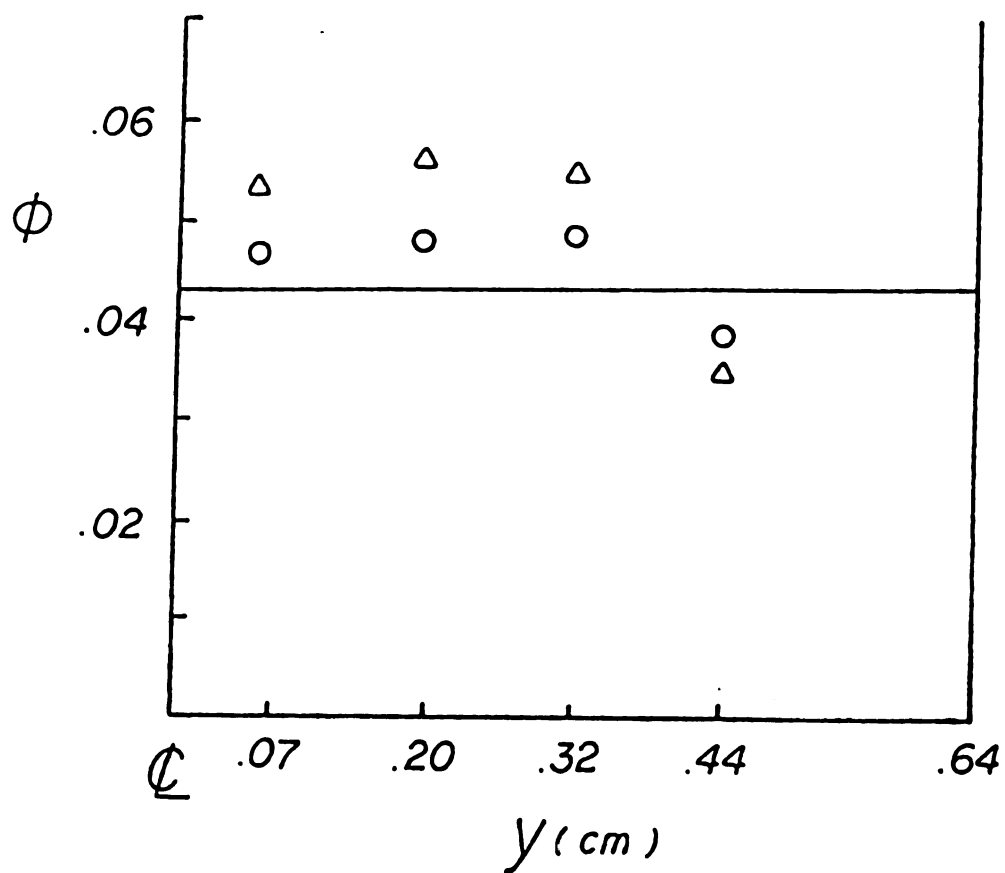


Figure 5.26 Void Fraction Profile With 3.5 wt Percent Separan Solution

$$\phi_b = .043 \quad , \quad \langle v \rangle = 1.29 \text{ cm/sec}$$

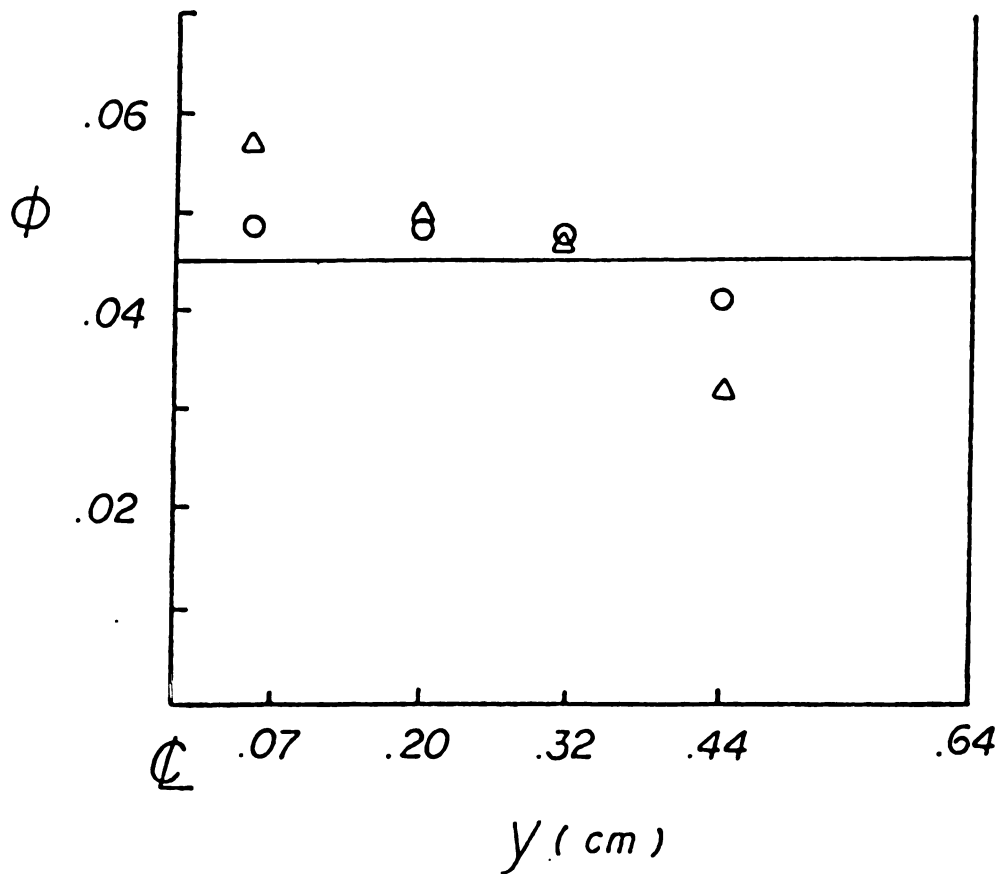


Figure 5.27 Void Fraction Profile With 3.5 wt Percent Separan Solution

$$\phi_b = .045 \quad \langle U \rangle = .71 \text{ cm/sec}$$

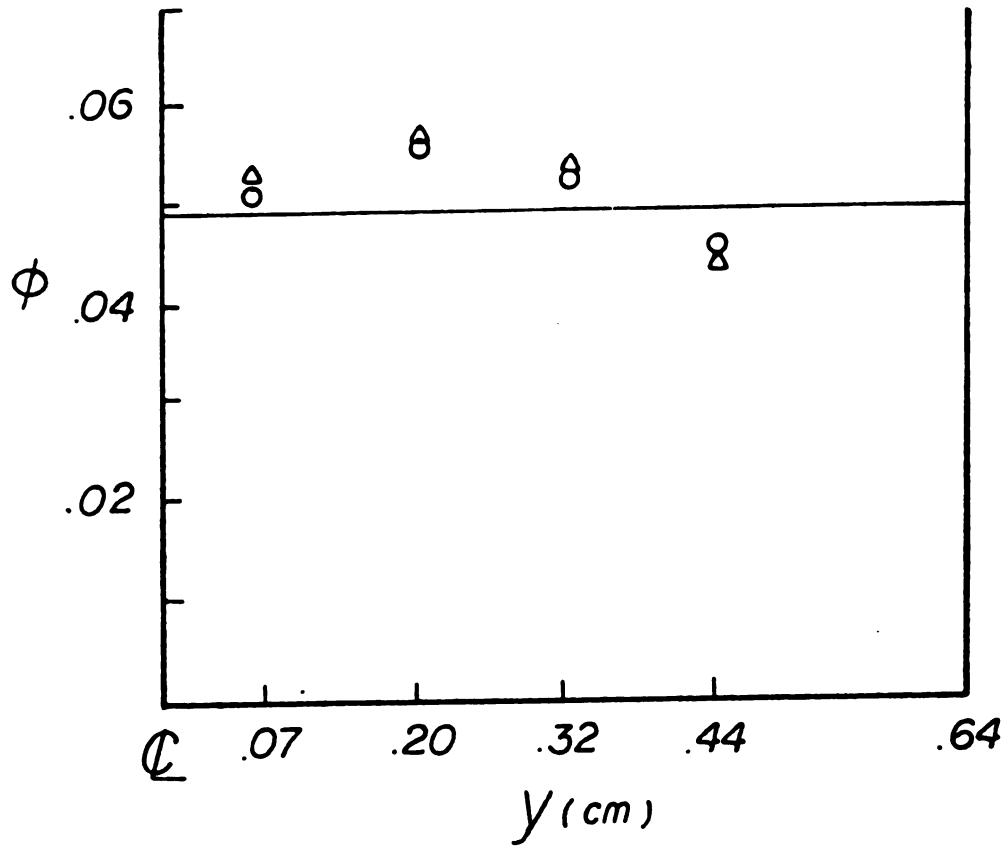


Figure 5.28 Void Fraction Profile With 3.5 wt Percent Separan Solution

$$\phi_b = .049, \quad \langle u \rangle = .5 \text{ cm/sec}$$

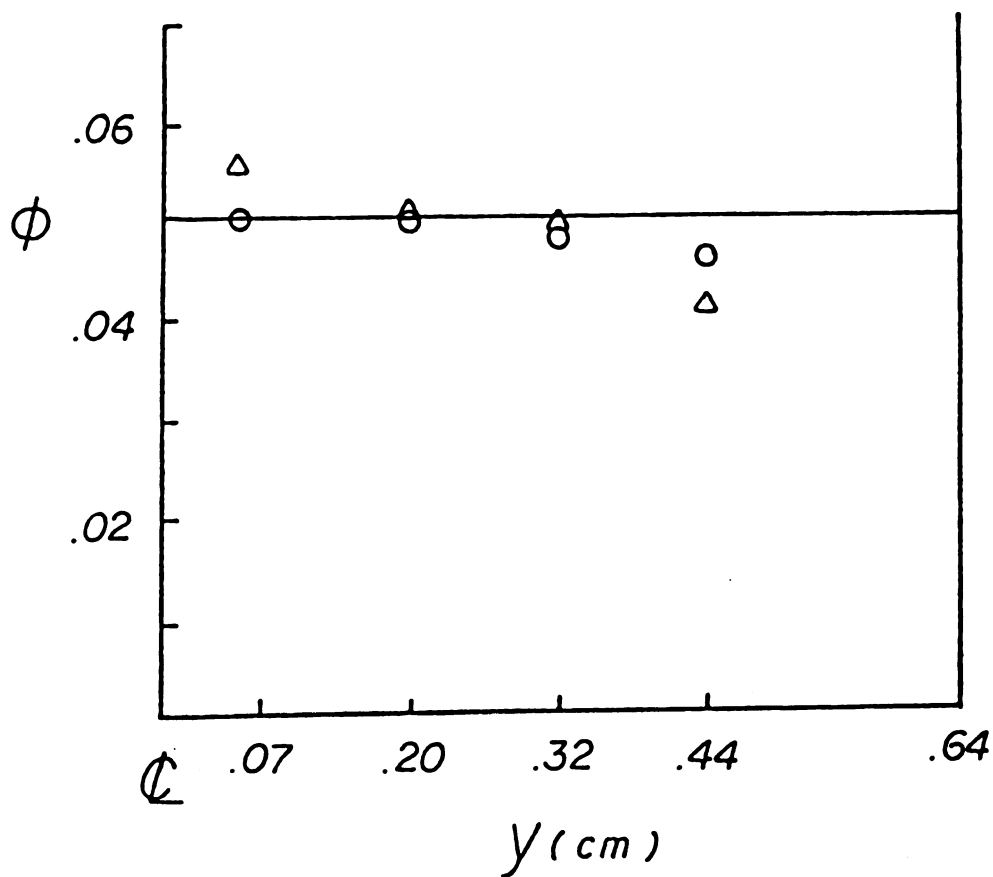


Figure 5.29

Void Fraction Profile With 3.5 wt
Percent Separan Solution

$$\phi_b = .05, \quad \langle U \rangle = .4 \text{ cm/sec}$$

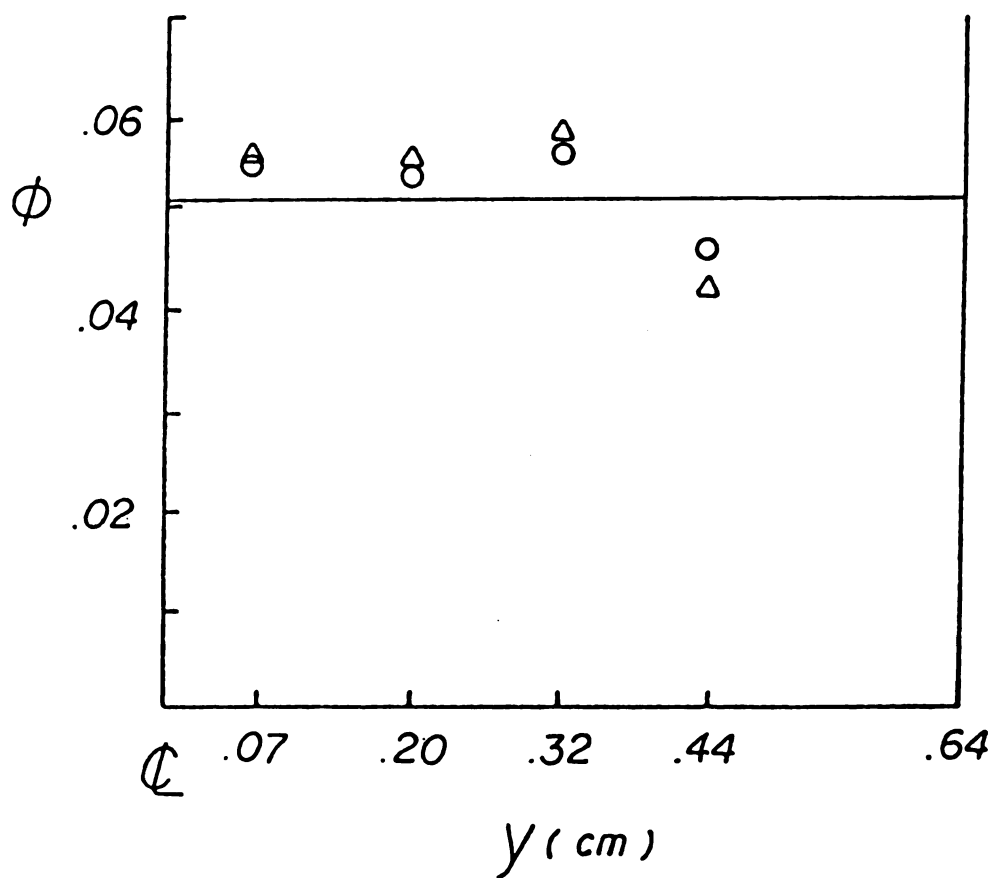


Figure 5.30 Void Fraction Profile With 3.5 wt Percent Separan Solution

$$\phi_b = .05, \quad \langle U \rangle = 1.18 \text{ cm/sec}$$

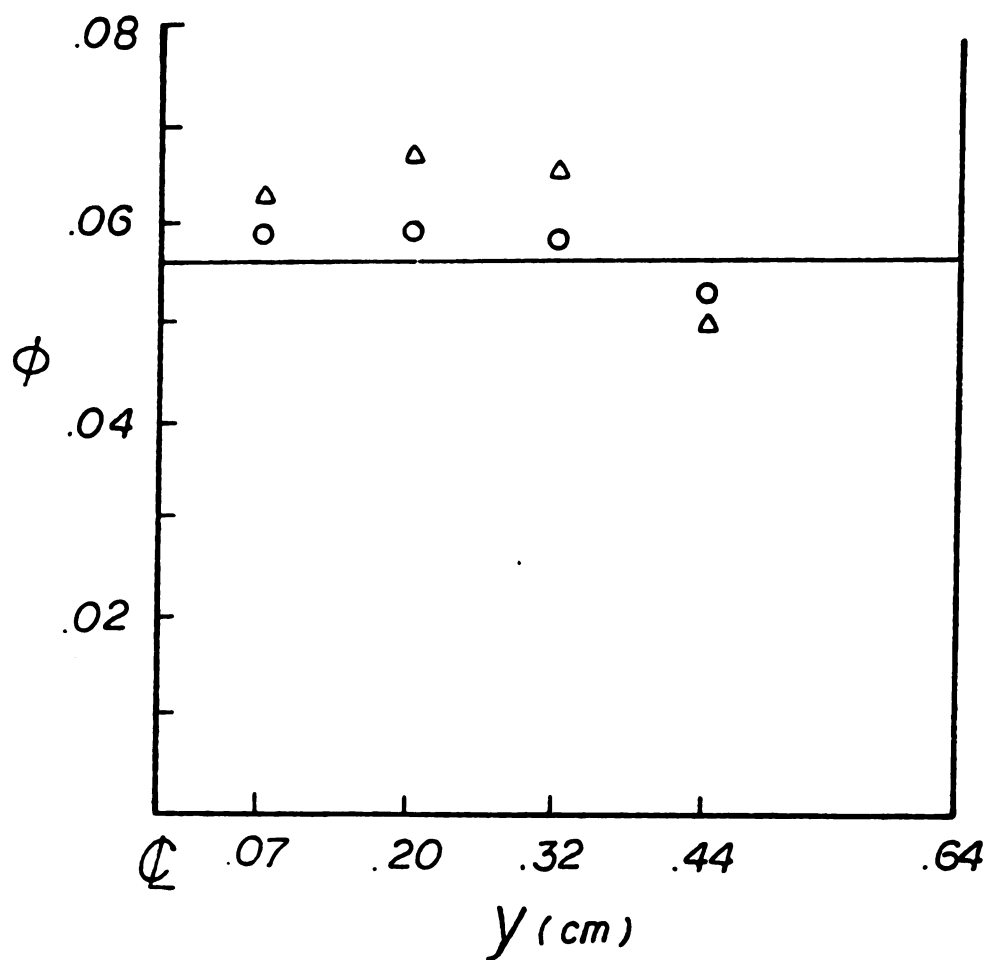


Figure 5.31 Void Fraction Profile With 3.5 wt Percent Separan Solution

$$\phi_b = .056, \langle U \rangle = .73 \text{ cm/sec}$$

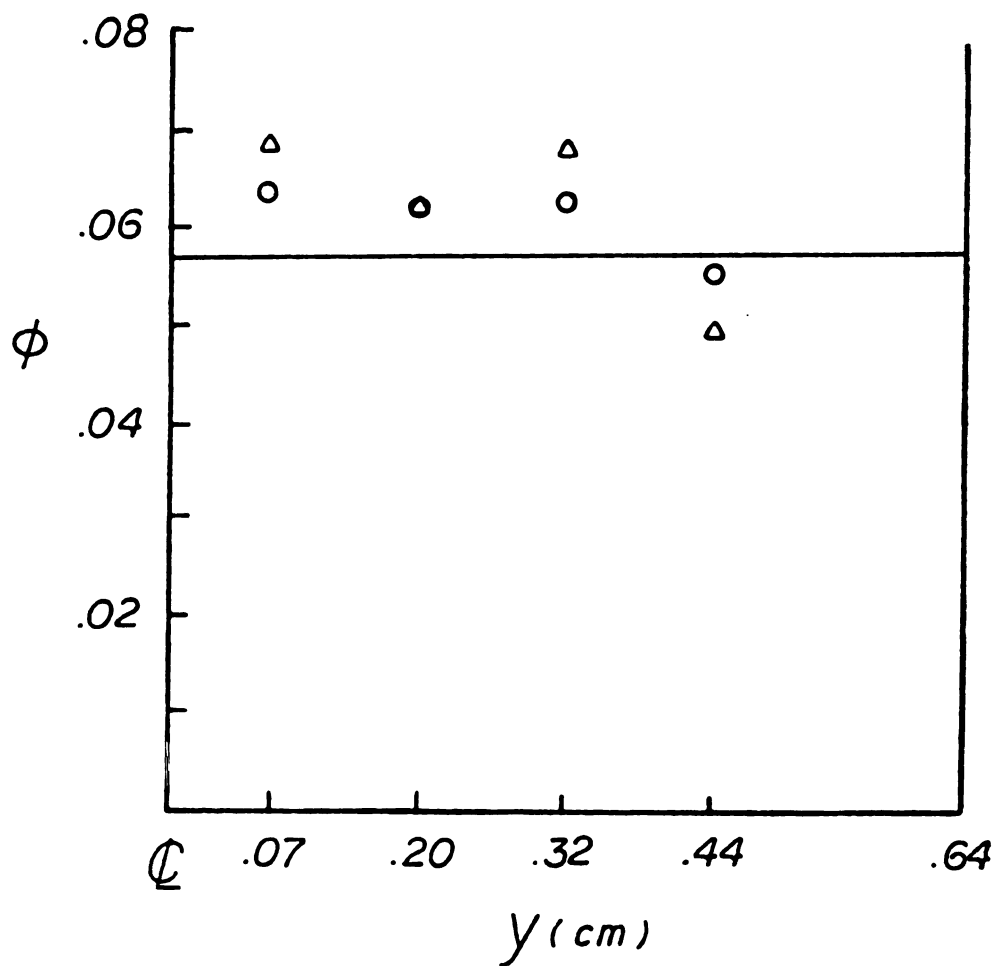


Figure 5.32 Void Fraction Profile With 3.5 wt Percent Separan Solution

$$\phi_b = .057, \quad \langle U \rangle = .65 \text{ cm/sec}$$

at a lower flow rate ($\langle U \rangle \sim 0.7$) in 3.5 wt percent Separan than ($\langle U \rangle \sim 1.0$) in 2.5 wt percent Separan solution. The formation of uniform bubbly core is affected more by flow rate than the bulk void fraction. It would seem that high elasticity of the medium is responsible for greater nonhomogeneity and quicker core formation in this medium.

5.D Correlation of Two-Phase Structure With Medium Properties

Previous studies (Gauthier et al. (1971a,b)) have established that particle migration is toward the flow axis in viscoelastic fluids and toward the wall in pseudoplastic (i.e. only shear-thinning) fluids. Separan solutions are highly elastic but they also have characteristics of a pseudoplastic fluid. Although normal stresses gradients and shear-thinning effects on bubble migration cannot in general be separated easily, the trends discussed above may be correlated by means of a recoverable shear ratio - i.e. $N_1/2\tau$, where N_1 is the primary normal stress difference and τ is the shear stress.

Chan and Leal (1979) derived the migration velocity of a deformable droplet in a second order fluid undergoing a unidirectional flow. For an inviscid drop, the migration velocity can be written as

$$V = -\left(\frac{dU}{dy}\right)\left(\frac{d^2U}{dy^2}\right)\frac{a^2}{\eta}\left[.508(\psi_1 + \psi_2) - .587\psi_1\right] \quad (5.1)$$

which indicates the migration velocity is a function of shear rate, the gradient of shear rate, drop size, medium viscosity and elasticity. In general, the secondary normal stress coefficient ψ_2 is usually about 10% of primary normal stress coefficient ψ_1 , and is negative. So assuming $\psi_2 = -.1\psi_1$, the migration velocity can be simplified to

$$\begin{aligned} V &= .13 \frac{\psi_1 a^2}{\eta} \left(\frac{dU}{dy} \right) \left(\frac{d^2 U}{dy^2} \right) \\ &= .26 a^2 \left(\frac{N_1}{2\tau} \right) \left(\frac{d^2 U}{dy^2} \right) \\ &= .26 a^2 S_R \left(\frac{d^2 U}{dy^2} \right) \end{aligned} \quad (5.2)$$

The migration velocity is proportional to the recoverable shear ratio S_R . This was derived only for a single bubble in a second order fluid. It is worthwhile to note that recoverable shear ratio S_R is maximum at the wall, where bubbles are quickly depleted. The value of this recoverable shear ratio at the wall,

$$S_{R,w} = N_1 / 2\tau_w$$

may be obtained from measurements of the wall shear stress, using the curves for pure polymer solutions of N_1 and τ vs $\dot{\gamma}$ in Figures 3.5 and 3.6. Thus, a qualitative correlation between the recoverable shear ratio at the wall $S_{R,w}$ and the profile development is attempted in Table 5.1. In cases where a uniform central core is formed, the core thickness

TABLE 5.1

COMPARISON OF VOID FRACTION PROFILES

2.5 wt Percent Separan Solution

Figure		cm/sec	N/m ²	S _{R,v}	Upstream (18 cm)	Downstream (47 cm)
5.10	.018	.7	44.26	.329	no variation	uniform core
5.11	.02	.82	44.57	.329	no variation	peaked
5.12	.022	.4	38.2	.292	peaked	peaked
5.13	.024	.58	44.57	.329	peaked	peaked
5.14	.25	.54	40.1	.268	no variation	uniform core
5.15	.032	.78	44.0	.276	peaked	peaked
5.16	.032	1.17	49.7	.396	peaked	peaked
5.17	.031	1.18	49.7	.396	peaked	uniform core
5.18	.234	.81	44.4	.396	no variation	uniform core
5.19	.035	.6	40.1	.268	no variation	uniform core
5.20	.077	1.33	50.9	.341	uniform core	uniform core

TABLE 5.1

COMPARISON OF VOID FRACTION PROFILES

3.5 wt Percent Separan Solution

Figure		cm/sec	N/m ²	S _{R,v}	Upstream (18 cm)	Downstream (47 cm)
5.21	.026	.93	51.3	.443	no variation	no variation
5.22	.032	.32	20.	.27	no variation	no variation
5.23	.035	.91	49.7	.441	uniform core	uniform core
5.24	.035	1.5	49.7	.441	uniform core	uniform core
5.25	.04	.82	39.7	.36	peaked	peaked
5.26	.043	1.29	43.0	.375	uniform core	uniform core
5.27	.045	.71	36.4	.345	no variation	peaked
5.28	.049	.5	33.1	.328	uniform core	uniform core
5.29	.05	.4	24.6	.282	no variation	peaked
5.30	.051	1.18	38.	.35	uniform core	uniform core
5.31	.056	.73	35.	.338	uniform core	uniform core
5.32	.057	.65	39.7	.36	uniform core	uniform core

Δc , may be estimated from the core concentration with the knowledge that expansion during the experiment is negligible. It is to be noted that the residence times corresponding to the two locations are different in different runs, as shown in Table 5.1. The recoverable shear ratios at wall (.28 to .47) of 3.5 wt percent Separan solution are in general higher than those of 2.5 wt percent Separan solution (.26 to .39), which account for quicker formation of void fraction profile in the former solutions. Higher values of $S_{R,w}$ (> 0.35) lead to quicker formation of uniform central bubbly core, and a narrower core or a thicker bubble free layer. At bulk void fractions of 0.05 or less, the effect of $S_{R,w}$ dominates. At bulk fractions greater than 0.05, the formation of uniform core and wall layer is enhanced by the increasing bubble void fraction. The effect of bulk void fraction on the profile dominates the medium effect in concentrated suspensions has been observed by Karnis and Mason (1967) which may even change the velocity profile into a blunt one. However, in this study, the bulk void fraction is much less than that in the concentrated system, the effect of elasticity seems to be the predominate one.

CHAPTER 6

BULK RHEOLOGY OF DILUTE SUSPENSIONS IN VISCOELASTIC LIQUIDS

6.A Introduction

The experimental studies of suspensions of rigid or deformable, neutrally buoyant particles in viscoelastic liquids demonstrate that such suspensions are often macroscopically nonhomogeneous even in extremely low Reynolds number flow as a consequence of the medium elasticity. Our observations indicate that flow may still be divided into a few macroscopically homogeneous regions so that a bulk stress relation for a homogeneous suspension is useful in each of the subregions. A relative viscosity relation for the suspension is required to explain the increase in flow rate with increasing void fraction in such situations.

The relative shear viscosity of suspensions of rigid, spherical particles in polymer solutions as well as polymer melts has been measured by several investigators including Highgate and Whorlow (1970) and Kataoka et al. (1978). They conclude that for dilute suspensions at low shear rates, the relative viscosity increases with concentration but decreases with shear rate; however the effect of medium properties on this dependence was not clear from these studies. Han and King (1980) report that the relative shear viscosity of suspensions containing 10 percent of spherical (Newtonian) poly-

butene droplets in a 2 wt. percent aqueous solution of Separan is lower than one and decreases with concentration at shear stresses of 50-100 N/m² over the low concentration range. The primary normal stress difference is reported to increase with concentration of disperse phase in suspensions of rigid spheres as well as droplets.

The object of work presented in this chapter is to derive a theoretical relation for the bulk stress in dilute suspensions of neutrally buoyant, uniform size, spherical inclusions -- rigid or deformable -- with a viscoelastic medium under simple shear. The inclusions are assumed to be small enough to remain spherical, and large enough for exclusion of Brownian motion in the analysis. The viscoelastic medium may be described by the second order fluid model if the fluid motion is "rheologically slow", that is the fluid relaxation time is small but finite compared to the time scale of fluid motion. The disturbance velocity and pressure fields interior and exterior to a spherical drop suspended in a second order fluid undergoing steady shear far from the drop were derived by Peery (1966) for small Weissenberg numbers, omitting inertia. These fields are used to derive an average stress over a volume small compared to the dimension along the shear gradient direction, yet containing many particles, following the discussion of Batchelor (1972). The result is a third order fluid model for the suspension, which shows that the dependence of relative

shear viscosity on shear rate is associated with the elasticity of the medium.

This chapter starts with a statement of the microrheological problem involved here and a summary of Peery's solution to this problem. This is followed by a discussion of the integrals that arise on applying the averaging procedure to dilute suspensions in the second order fluid medium. The resulting third order fluid model is then discussed in the light of available data from viscometers.

6.B Microrheology

The microrheological problem here involves creeping flow of an incompressible, second order fluid around a single spherical drop of an incompressible, Newtonian fluid in the absence of external force or torque, with a steady shear flow imposed far from the drop. The relevant equations of continuity and motion are

$$\nabla \cdot \underline{U} = 0 \quad , \quad \nabla \cdot \underline{\underline{G}} = 0 \quad (6.1)$$

$$\underline{\underline{G}} = -p \underline{\underline{I}} + \eta_0 \underline{\underline{L}}_1 - \frac{\psi_0}{2} \underline{\underline{L}}_2 + (\psi_0 + \psi_{20}) \underline{\underline{L}}_1 \cdot \underline{\underline{L}}_1 \quad (6.2)$$

for the continuous phase with constant viscosity η_0 and constant primary and secondary normal stress coefficients ψ_0, ψ_{20} . $\underline{\underline{L}}_1, \underline{\underline{L}}_2$ are Rivlin-Erickson tensors given by

$$\underline{\underline{L}}_1 = \nabla \underline{U} + \nabla \underline{U}^T \quad (6.3)$$

$$\underline{\underline{L}}_2 = \underline{U} \cdot \nabla \underline{\underline{L}}_1 + \underline{\underline{L}}_1 \cdot \nabla \underline{U} + \nabla \underline{U}^T \cdot \underline{\underline{L}}_1 \quad (6.4)$$

The fields inside the Newtonian drop obeys the equations

$$\nabla \cdot \underline{U}' = 0 \quad , \quad \nabla \cdot \underline{\sigma}' = 0 \quad (6.5)$$

$$\underline{\sigma}' = -p' \underline{I} + \eta' (\nabla \underline{U}' + \nabla \underline{U}'^T) \quad (6.6)$$

where the primed variables corresponds to the disperse phase. The above equations may be nondimensionalized using the radius of drop "a" as the length scale, Ga as the velocity scale, where G is the bulk rate of shear strain, and $\eta_0 G$ as the (viscous) stress scale. The resulting dimensionless equations including boundary conditions are summarized below.

Exterior flow field

$$\nabla \cdot \underline{u} = 0 \quad , \quad \nabla \cdot \underline{\pi} = 0 \quad (6.7)$$

$$\underline{\pi} = -p \underline{I} + \underline{A}_1 + \lambda \epsilon_1 \underline{A}_2 + \lambda (\underline{A}_1 \cdot \underline{A}_1^T) \quad (6.8)$$

λ is the index of the medium elasticity -- a modified Weissenberg number, and $\epsilon_1 = -\psi_{10}/2(\psi_{10} + \psi_{20})$ is a ratio of normal stress coefficients typically between -0.5 and -0.85. \underline{A}_1 and \underline{A}_2 are defined similar to \underline{L}_1 and \underline{L}_2 as

$$\underline{A}_1 = \nabla \underline{u} + \nabla \underline{u}^T \quad (6.9)$$

$$\underline{A}_2 = \underline{u} \cdot \nabla \underline{A}_1 + \underline{A}_1 \cdot \nabla \underline{u} + \nabla \underline{u}^T \cdot \underline{A}_1 \quad (6.10)$$

Interior flow field

$$\nabla \cdot \underline{u}' = 0 \quad ; \quad \nabla \cdot \underline{\pi}' = 0 \quad (6.11)$$

$$\underline{\pi}' = -p' \underline{I} + K(\nabla \underline{u}' + \nabla \underline{u}'^T) \quad (6.12)$$

K is the ratio of drop viscosity to medium viscosity. The origin of the coordinate system coincides with the center of the drop, the disturbance due to the presence of the sphere is zero far from the sphere.

$$\underline{r} \rightarrow \infty \quad \underline{u} = \underline{\alpha} \cdot \underline{r} \quad (6.13)$$

$$p = 0 \quad (6.14)$$

where $\underline{\alpha}$ is a constant and from the incompressible fluid conditions $\nabla \cdot (\underline{\alpha}) = 0$. At the drop-medium interface, the no-slip condition is imposed and so is the continuity of tangential stress. Assuming the drop is spherical, its surface is therefore given permanently by $r=1$. Thus

$$\underline{u} = \underline{u}' \quad (6.15)$$

$$r=1 \quad \underline{n} \times (\underline{\pi} - \underline{\pi}') \cdot \underline{n} = 0 \quad (6.16)$$

$$\underline{n} \cdot \underline{u} = \underline{n} \cdot \underline{u}' \quad (6.17)$$

Assuming zero Reynolds number, the governing equations for

creeping motion are

$$\nabla^2 \underline{u} - \nabla p + \nabla \cdot \underline{\underline{\tau}} = 0 \quad (6.18)$$

$$\nabla^2 \underline{u}' - \nabla p' = 0 \quad (6.19)$$

where $\underline{\underline{\tau}}$ represents the non-Newtonian part of second order fluid. A perturbation scheme can be used to solve the non-linear exterior creeping motion equation by assuming the velocity and pressure fields may be expressed as an expansion in power of

$$\begin{bmatrix} \underline{u} \\ p \\ \underline{u}' \\ p' \end{bmatrix} = \begin{bmatrix} \underline{u}_0 \\ p_0 \\ \underline{u}'_0 \\ p'_0 \end{bmatrix} + \lambda \begin{bmatrix} \underline{u}_1 \\ p_1 \\ \underline{u}'_1 \\ p'_1 \end{bmatrix} + \dots \quad (6.20)$$

Here the zeroth order terms solve the problem with a Newtonian medium. Expressions for the zeroth and first order terms in various fields have been derived by Peery (1966) and are summarized in appendix C.

6.C The Bulk Stress

The bulk (macroscopic) properties can now be described in terms of averages over corresponding microrheological quantities. Associated with the volume average method, there are four characteristic length scales depicted in

Figure 6.1: 1) a , the radius of a drop; 2) d , the average distance between the centers of adjacent drops; 3) the largest linear dimension $\ell (\gg d)$ of a representative volume V containing a significant number of drops and over which the microrheological properties vary with simple shear appreciably; 4) H , the length scale over which the suspension is undergoing a simple shear. With $a \ll d$, only noninteracting spherical drops are considered; with $\ell \ll H$, we may evaluate average quantities at a "macroscopic point" -- that is, on the scale of the flow, the neighborhood of averaging may be treated as a point. This is useful in discussion quantities such as $\langle \underline{A}, \underline{A} \rangle$ and $\langle \underline{A}_s \rangle$.

The dimensionless bulk stress \underline{T} may be written at very low Reynolds number, following Batchelor (1970) as

$$\underline{T} = \frac{1}{V} \left[\int_{V-\Sigma v_0} \underline{\pi} dV + \sum \int_{v_0} \underline{\pi}' dV \right] \quad (6.21)$$

where v_0 and S_0 denote the volume and surface area of a single drop. With the help of a tensor identity and the equation of motion, $\underline{\pi}'$ can be written as

$$\begin{aligned} \underline{\pi}' &= \nabla \cdot (\underline{\pi}' \underline{r}) - (\nabla \cdot \underline{\pi}') \underline{r} \\ &= \nabla \cdot (\underline{\pi}' \underline{r}) \end{aligned} \quad (6.22)$$

Using the divergence theorem on the second volume integral and incorporating stress continuity at the interface, we

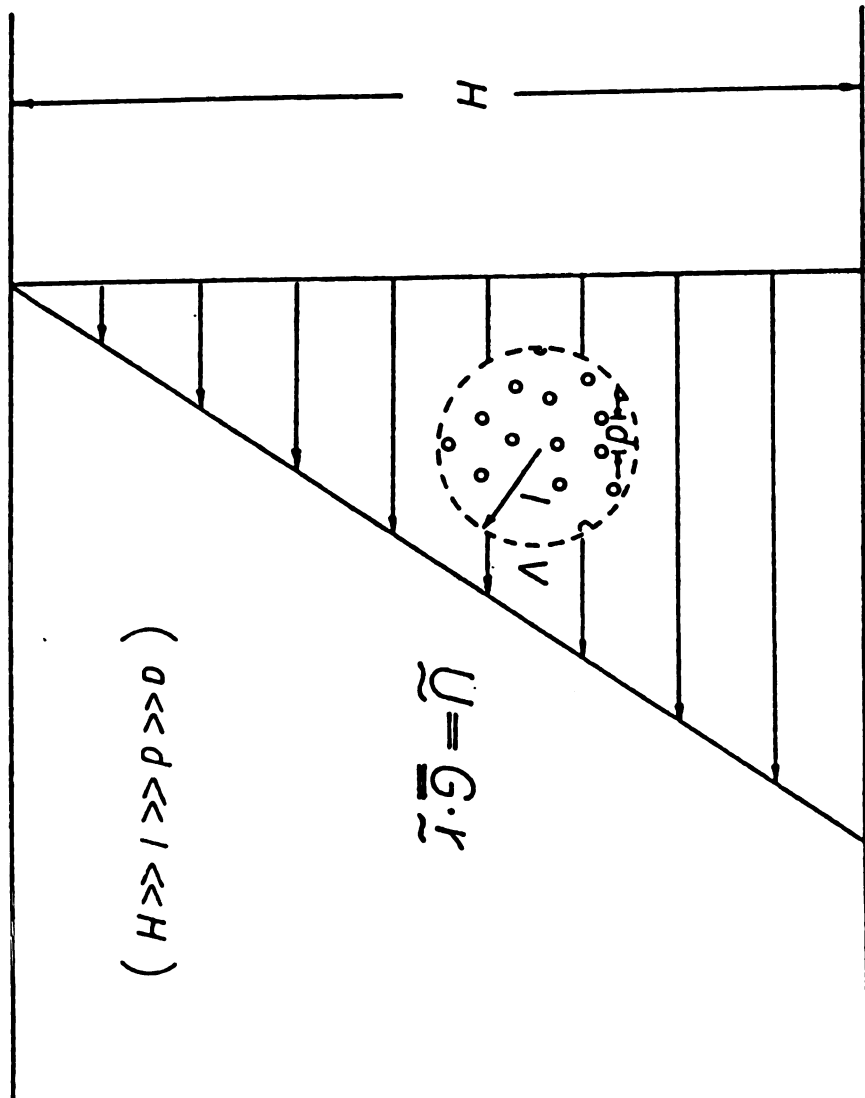


Figure 6.1 Characteristic Dimension of Dilute Suspension in Simple Steady Shear

obtain

$$\underline{T} = \frac{1}{V} \left[\int_{V-ZV_0} \underline{\pi} dV + \sum \int_{S_0} \underline{n} \cdot (\underline{\pi}^T \underline{L}) dS \right] \quad (6.23)$$

The first volume integral can be related to average quantities by the following identities

$$\begin{aligned} \langle \underline{A}_1 \rangle &= \frac{1}{V} \left[\int_{V-ZV_0} \underline{A}_1 dV + \sum \int_{V_0} \underline{A}_1' dV \right] \\ &= \frac{1}{V} \left[\int_{V-ZV_0} \underline{A}_1 dV + \sum \int_{S_0} (\underline{u} \underline{n} + \underline{n} \underline{u}) dS \right] \end{aligned} \quad (6.24)$$

$$\begin{aligned} \langle \underline{A}_2 \rangle &= \frac{1}{V} \left[\int_{V-ZV_0} \underline{A}_2 dV + \sum \int_{V_0} \underline{A}_2' dV \right] \\ \langle \underline{A}_1 \cdot \underline{A}_1 \rangle &= \frac{1}{V} \left[\int_{V-ZV_0} \underline{A}_1 \cdot \underline{A}_1 dV + \sum \int_{V_0} \underline{A}_1' \cdot \underline{A}_1' dV \right] \end{aligned}$$

Substituting from (6.7), (6.11) and (6.24) into (6.23) and separating the isotropic terms (as qI), we obtain for the bulk deviation stress

$$\underline{T} + \beta \underline{I} = \langle \underline{A}_1 \rangle + \lambda \epsilon_1 \langle \underline{A}_2 \rangle + \lambda \langle \underline{A}_1 \cdot \underline{A}_1 \rangle + \underline{T}_E \quad (6.25)$$

The extra stress due to the disperse phase, \underline{T}_E involves surface and volume integrals taken over a drop.

$$\begin{aligned} \underline{T}_E &= \frac{1}{V} \sum \left\{ \int_{S_0} \left[\underline{n} \cdot (\underline{\pi}^T \underline{L} - \lambda \epsilon_1 \underline{u} \underline{A}_1) - (\underline{n} \underline{u} + \underline{u} \underline{n}) \right] \right. \\ &\quad \left. dS - \int_{V_0} \left[\lambda \epsilon_1 (\underline{A}_1' \cdot \nabla \underline{u}' - \nabla \underline{u}'^T \cdot \underline{A}_1') \right. \right. \\ &\quad \left. \left. + \lambda \underline{A}_1' \cdot \underline{A}_1' \right] dV \right\} \end{aligned} \quad (6.26)$$

The identity $\nabla \cdot (\underline{u} \underline{A}_1) = \underline{u} \cdot \nabla \underline{A}_1 + (\nabla \cdot \underline{u}) \underline{A}_1$, with $\nabla \cdot \underline{u} = 0$

has been incorporated into equation (6.26). The terms $\langle \underline{A}_1 \cdot \underline{A}_1 \rangle$ and $\langle \underline{A}_2 \rangle$ in equation (6.25) deserve some attention here, for example, writing \underline{A}_1 , as the sum of the average $\langle \underline{A}_1 \rangle$ and a fluctuation $\underline{\tilde{A}}_1$, we obtain

$$\langle \underline{A}_1 \cdot \underline{A}_1 \rangle = \langle \underline{A}_1 \rangle \cdot \langle \underline{A}_1 \rangle + \langle \underline{\tilde{A}}_1 \cdot \underline{\tilde{A}}_1 \rangle \quad (6.27)$$

If one looks at these averages at a "macroscopic point", the fluctuating quantities when averaged, $\langle \underline{\tilde{A}}_1 \cdot \underline{\tilde{A}}_1 \rangle$ should be of order ϕ^2 , where ϕ is the volume fraction of disperse phase. Since we are considering dilute suspensions, it should be reasonable to omit $\langle \underline{\tilde{A}}_1 \cdot \underline{\tilde{A}}_1 \rangle$, so that

$$\langle \underline{A}_1 \cdot \underline{A}_1 \rangle \simeq \langle \underline{A}_1 \rangle \cdot \langle \underline{A}_1 \rangle \quad (6.28)$$

Similarly, fluctuating quantities involving second order terms in $\langle \underline{A}_2 \rangle$ can be omitted, so that

$$\langle \underline{A}_2 \rangle \simeq \langle \underline{U} \rangle \cdot \nabla \langle \underline{A}_1 \rangle + \langle \underline{A}_1 \rangle \cdot \langle \nabla \underline{U} \rangle + \langle \nabla \underline{U}^T \rangle \cdot \langle \underline{A}_1 \rangle \quad (6.29)$$

Substituting for \underline{T}_E in equation (6.26) and recognizing that the disperse phase volume fraction is related to the number of drops N in the volume V by

$$\phi = \left(\frac{4\pi a^3}{3} \right) N / V \quad (6.30)$$

we obtain

$$\underline{T}_E = \frac{3\phi}{4\pi} (\underline{T}_1 + \underline{T}_2) \quad (6.31)$$

where $\underline{\mathcal{T}}$ is a surface integral

$$\underline{\mathcal{T}} = \int_{\Sigma} dS \underline{n} \cdot \left[(-p \underline{I} + \underline{A}' + \lambda \epsilon_i \underline{A}_i + \lambda \underline{A}' \cdot \underline{A}') \underline{I} - \lambda \epsilon_i \underline{u} \underline{A}_i \right] \quad (6.32)$$

and $\underline{\mathcal{T}}_v$ is a volume integral

$$\underline{\mathcal{T}}_v = \int_{V_0} dV \left[\lambda \epsilon_i (\underline{A}' \cdot \nabla \underline{u}' + \nabla \underline{u}' \cdot \underline{A}') + \lambda \underline{A}' \cdot \underline{A}' \right] \quad (6.33)$$

Since the velocity and pressure fields occurring in equations (6.32) and (6.33) are available up to $O(\lambda)$ from Peery (1966), the extra stress tensor \underline{T}_E in our work includes all terms up to $O(\lambda^2)$.

$$\begin{aligned} \underline{\mathcal{T}} = \int_{\Sigma} dS \left\{ \left[\underline{n} \cdot (-p \underline{I} + \underline{A}'_0) \underline{I} - (\underline{n} \underline{u}_0 + \underline{u}_0 \underline{n}) + \lambda \left[\underline{n} \cdot (-p_1 \underline{I} + \underline{A}'^T_1 \right. \right. \right. \\ \left. \left. + \underline{A}'_0 \cdot \underline{A}'_0 + \epsilon \underline{A}'_{20} \right) \underline{I} - (\underline{n} \underline{u}_1 + \underline{u}_1 \underline{n}) - \epsilon_1 \underline{n} \cdot (\underline{u}_0 \underline{A}'_{10}) \right] + \lambda^2 \left[\right. \\ \left. \underline{n} \cdot (\underline{A}'_0 \cdot \underline{A}'^T_1 + \underline{A}'^T_1 \cdot \underline{A}'_0 + \epsilon \underline{A}'_{21}) \underline{I} - \epsilon_1 \underline{n} \cdot (\underline{u}_1 \underline{A}'_0 - \underline{u}_0 \underline{A}'_{11}) \right] \right\} \quad (6.34) \end{aligned}$$

$$\begin{aligned} \underline{\mathcal{T}}_v = \int_{V_0} dV \left\{ \lambda \left[-(\underline{A}'_0 \cdot \underline{A}'_0) - \epsilon_1 (\nabla \underline{u}'_0 \cdot \underline{A}'_0 + \underline{A}'_0 \cdot \nabla \underline{u}'_0^T) \right] \right. \\ \left. + \lambda^2 \left[-(\underline{A}'_0 \cdot \underline{A}'^T_1 + \underline{A}'^T_1 \cdot \underline{A}'_0) - \epsilon_1 (\nabla \underline{u}'_0 \cdot \underline{A}'_1 - \nabla \underline{u}'_1 \cdot \underline{A}'_0 \right. \right. \\ \left. \left. + \underline{A}'_1 \cdot \nabla \underline{u}'_0^T + \underline{A}'_0 \cdot \nabla \underline{u}'_1^T) \right] \right\} \quad (6.35) \end{aligned}$$

Subscripts 0 and 1 denote zeroth and first order terms in λ , e.g. \underline{A}'_1 is \underline{A}' evaluated with the first order interior velocity field. In evaluating $\underline{\mathcal{T}}$ and $\underline{\mathcal{T}}_v$ for this simple shear flow, only the symmetric part (the stresslet) will be considered to obtain \underline{T}_E . This is sufficient since there is no external torque on the system. The terms in $\underline{\mathcal{T}}$ and $\underline{\mathcal{T}}_v$

are up to order α^3 and λ^2 as may be seen from the following example

$$\lambda \epsilon_i \mathcal{L} \underline{A}_i = \lambda \epsilon_i \left[\mathcal{U}_0 \underline{A}_{i0} + \lambda (\mathcal{U}_0 \underline{A}_{i0} - \mathcal{U}_0 \underline{A}_{i1}) \right] \quad (6.36)$$

The first term on the right hand side of equation is of order λ and quadratic in $\underline{\alpha}$ noting that \mathcal{U}_0 is linear in $\underline{\alpha}$ and \underline{A}_{i0} is linear in $\underline{\alpha}$. The second term is then of order λ^2 and cubic in $\underline{\alpha}$ noting that \mathcal{U} , \underline{A}_i are quadratic in $\underline{\alpha}$ and \underline{A}_{i0} , \mathcal{U}_0 are linear in $\underline{\alpha}$. The surface integrals over a sphere can be evaluated with identities given by Brenner (1964)

$$\begin{aligned} \int n_i n_j d\Omega &= \frac{4}{3} \pi \delta_{ij} \\ \int n_i n_j n_k n_l d\Omega &= \frac{4\pi}{15} (\delta_{ij} \delta_{kl} + \delta_{ik} \delta_{jl} + \delta_{il} \delta_{jk}) \\ \int n_i n_j n_k n_l n_p n_q d\Omega &= \frac{4\pi}{105} (\delta_{ij} \delta_{kl} \delta_{pq} + 14 \text{ similar combinations}) \end{aligned} \quad (6.37)$$

The volume integrals in \underline{J}_2 can be evaluated only when the integral terms are expanded in terms of $\underline{\alpha}$ and \mathcal{L} for example

$$\begin{aligned} \int_{V_0} \frac{1}{r^n} (\underline{\alpha} \cdot \underline{\alpha} \cdot \mathcal{L}) dV &= \frac{1}{4-n} \int_{V_0} \nabla \cdot (\mathcal{L} \underline{\alpha} \cdot \underline{\alpha} \cdot \mathcal{L}) dV \\ &= \frac{1}{4-n} \int_{S_0} \underline{\alpha} \cdot \underline{\alpha} \cdot \mathcal{L} dS \end{aligned} \quad (6.38)$$

where the identity

$$\nabla \cdot \left(\frac{1}{r^n} \underline{\underline{\alpha}} \cdot \underline{\underline{\alpha}} \cdot \underline{\underline{r}} \right) dV = (4-n) \frac{1}{r^n} (\underline{\underline{\alpha}} \cdot \underline{\underline{\alpha}} \cdot \underline{\underline{r}}) \quad (6.39)$$

is used applying the same approach, all the volume integrals may be evaluated. The terms besides $\underline{\underline{T}}_E$ in equation (6.25) are of order λ at most and quadratic in $\underline{\underline{\alpha}}$. So, starting with a second order fluid model for the medium, the third order fluid model is obtained for the dilute suspension; this does not account for any departure from sphericity of the drop surface.

6.D Third Order Model For Suspension

In order to obtain the parameters of this third order model, the expressions involving $\underline{\underline{\alpha}}$ resulting from all the integration are first evaluated in unidirectional shear flow, i.e.

$$\underline{\underline{\alpha}} = \begin{bmatrix} 0 & 1 & 0 \\ 0 & 0 & 0 \\ 0 & 0 & 0 \end{bmatrix} \quad (6.40)$$

and

$$\underline{\underline{\gamma}} = \underline{\underline{\alpha}} + \underline{\underline{\alpha}}^T \quad (6.41)$$

This will allow us to evaluate the viscosity function and the normal stress coefficients which may be used to set up the general third order fluid model for steady shear.

The bulk stress may be written

$$\begin{aligned} \underline{T} + \delta \underline{T} = & (\underline{\alpha} + \underline{\alpha}^T) + \lambda \epsilon_1 (\underline{\alpha} \cdot \underline{\alpha} + 2 \underline{\alpha}^T \cdot \underline{\alpha} + \underline{\alpha}^T \cdot \underline{\alpha}^T) \\ & + \lambda (\underline{\alpha} + \underline{\alpha}^T) \cdot (\underline{\alpha} + \underline{\alpha}^T) + \underline{T}_E \end{aligned} \quad (6.42)$$

This relation can be reduced as

$$\begin{aligned} \underline{T} + \delta \underline{T} = & \left[1 + \lambda^2 \phi F \left(\frac{1}{2} \underline{\dot{\gamma}} : \underline{\dot{\gamma}} \right) \right] \underline{\dot{\gamma}} \\ & + \lambda \epsilon_1 \left[1 + \phi \left(\frac{b_{11} - b_{22}}{2 \epsilon_1} \right) (\underline{\dot{\gamma}} \cdot \underline{\alpha} + \underline{\alpha}^T \cdot \underline{\dot{\gamma}}) \right. \\ & \left. + \lambda \left[1 + \phi (b_{11} - b_{33}) \right] \underline{\dot{\gamma}} \cdot \underline{\dot{\gamma}} \right] \end{aligned} \quad (6.43)$$

where b_{11} , b_{22} , b_{33} and F are obtained as functions of ϵ_1 and κ by summing \underline{J}_1 , and \underline{J}_2 (cf. Appendix D). The result for unidirectional shear is

$$\begin{aligned} \underline{T} + \delta \underline{T} = & \begin{bmatrix} \lambda & 1 + \frac{5\kappa+2}{2(\kappa+1)} \phi & 0 \\ 1 + \frac{5\kappa+2}{2(\kappa+1)} \phi & \lambda + 2\lambda \epsilon_1 & 0 \\ 0 & 0 & 0 \end{bmatrix} \\ & + \phi \lambda \begin{bmatrix} b_{11} & 0 & 0 \\ 0 & b_{22} & 0 \\ 0 & 0 & b_{33} \end{bmatrix} + \phi \lambda^2 \begin{bmatrix} 0 & F & 0 \\ F & 0 & 0 \\ 0 & 0 & 0 \end{bmatrix} \end{aligned} \quad (6.44)$$

where b_{11} , b_{22} , b_{33} and F depend on ϵ_1 and κ as follows

$$b_{11} = \frac{1}{(\kappa+1)} \left[(4.74\kappa^2 + 1.86\kappa + 2.38) + \epsilon_1 (22.75\kappa^2 + 11.83\kappa + 8) \right] \quad (6.45)$$

$$b_{22} = \frac{1}{(\kappa+1)} \left[(-7.51\kappa^2 + 8.71\kappa - 1.69) + \epsilon_1 (28.35\kappa^2 + 13.37\kappa + 8) \right] \quad (6.46)$$

$$b_{33} = \frac{1}{(\kappa+1)} \left[(3.51\kappa^2 + 0.78\kappa + 2.22) + \epsilon_1 (23.28\kappa^2 + 16.21\kappa + 7.7) \right] \quad (6.47)$$

$$F = \frac{1}{(K+1)^3} \left[(-6.75K^3 - 17.04K^2 + 10.34K - 10.16) + E_1(2.6K^3 + 13.64K + 26.8K - 6.56) + E_1^2(1.17K^2 + 14.19K + 13.57K + 28.1) \right] \quad (6.48)$$

Reverting to dimensional terms, the shear viscosity η and normal stress coefficients ψ_1 and ψ_2 of the dilute suspension may be identified as follows

$$\eta = \eta_0 \left[1 + \frac{5K+2}{2(K+1)} \phi + \phi \frac{\psi_0^2 \dot{\gamma}^2}{4e_1^2 \eta_0^2} F \right] \quad (6.49)$$

This relation includes in addition to the "Taylor correction" for suspensions in Newtonian media, a shear rate dependent term involving the Weissenberg number ($We = \psi_0 G / \eta_0$) which is a ratio of fluid relaxation time to fluid flow time. The higher the Weissenberg number, the stronger the shear rate dependence of suspension viscosity. Further, as the volume fraction ϕ is increased, this dependence is once again enhanced. The normal stress coefficients of the suspension are

$$\psi_1 = \psi_{10} \left[1 + \phi \left(\frac{b_{11} - b_{22}}{-2e_1} \right) \right] \quad (6.50)$$

$$\psi_2 = \psi_{20} + \phi (\psi_{10} + \psi_{20}) (b_{22} - b_{33}) \quad (6.51)$$

6.E Discussion

We proceed to evaluate the above material functions for two limiting cases of rigid spheres and inviscid drops selecting ψ_{20}/ψ_{10} to be -0.1 (or $\epsilon = -0.56$). For a suspension of rigid spheres ($\kappa \rightarrow \infty$), we obtain

$$\eta = \eta_0 (1 + 2.5\phi - 6.83\phi G^2 \psi_0^2 / \eta_0^2) \quad (6.52)$$

$$\psi_1 = \psi_{10} (1 + 13.7\phi) \quad (6.53)$$

$$\psi_2 = \psi_{20} (1 + 61\phi) \quad (6.54)$$

For a suspension of inviscid drops ($\kappa \rightarrow 0$), we obtain

$$\eta = \eta_0 (1 + \phi - 3 G^2 \psi_0^2 \phi / \eta_0^2) \quad (6.55)$$

$$\psi_1 = \psi_{10} (1 + 3.43\phi) \quad (6.56)$$

$$\psi_2 = \psi_{20} (1 + 38.5\phi) \quad (6.57)$$

For both cases, the viscosity decreases with shear strain rate at a rate proportional to We^2 . It is worth noting that the microrheological properties were solved for $We \ll 1$, and medium viscosity is shear-rate independent, hence the utility of these results is in indicating trends, viz.

- 1) as the volume fraction ϕ or the shear strain rate is increased the bulk viscosity is decreased.
- 2) as the volume fraction ϕ is increased, both normal stress coefficients are increased in magnitude.

For rigid spheres, the viscometric data of methacrylate spheres in 3.5% aqueous carboxymethylcellulose solution (SCMC) reported by Highgate and Whorlow (1970) can be used to test this model. Sodium Carboxymethylcellulose solution has low Weissenberg numbers, from 0.2 to 0.47 over the shear rate range 1 sec^{-1} to 10 sec^{-1} . The experimental relative viscosity decreases with shear rate as well as void fraction as shown in Figure 6.2 to 6.5. The relative viscosity matches the Einstein relation approaching zero shear rate and volume fraction. As shear rate increases or as volume fraction increases, the gap between the experimental result and the Einstein relation becomes larger; the suspension becoming strongly shear-thinning. At high shear rate, all data show limiting relative viscosities; 1.01, 1.03, 1.05, 1.06 for volume fractions of 0.02, 0.05, 0.07 and 0.10 respectively. The relative viscosity limit is attained at shear rate of about 5 sec^{-1} at low volume fraction of . The predicted relative viscosity follows the same trend as experimental data from volume fraction 0.02 to 0.10. However, the predicted relative viscosities are higher than the observed ones for all the volume fractions. At $\phi \ll 0.05$, referred to as dilute suspension, the theoretical results are satisfactory. At $\phi > 0.05$, the largest deviations from data occur at shear rate of 2 sec^{-1} , the error is about 6%. The departure at low shear rate may be due to the particle aggregation and disaggregation (cf. Matsumoto (1978)), which

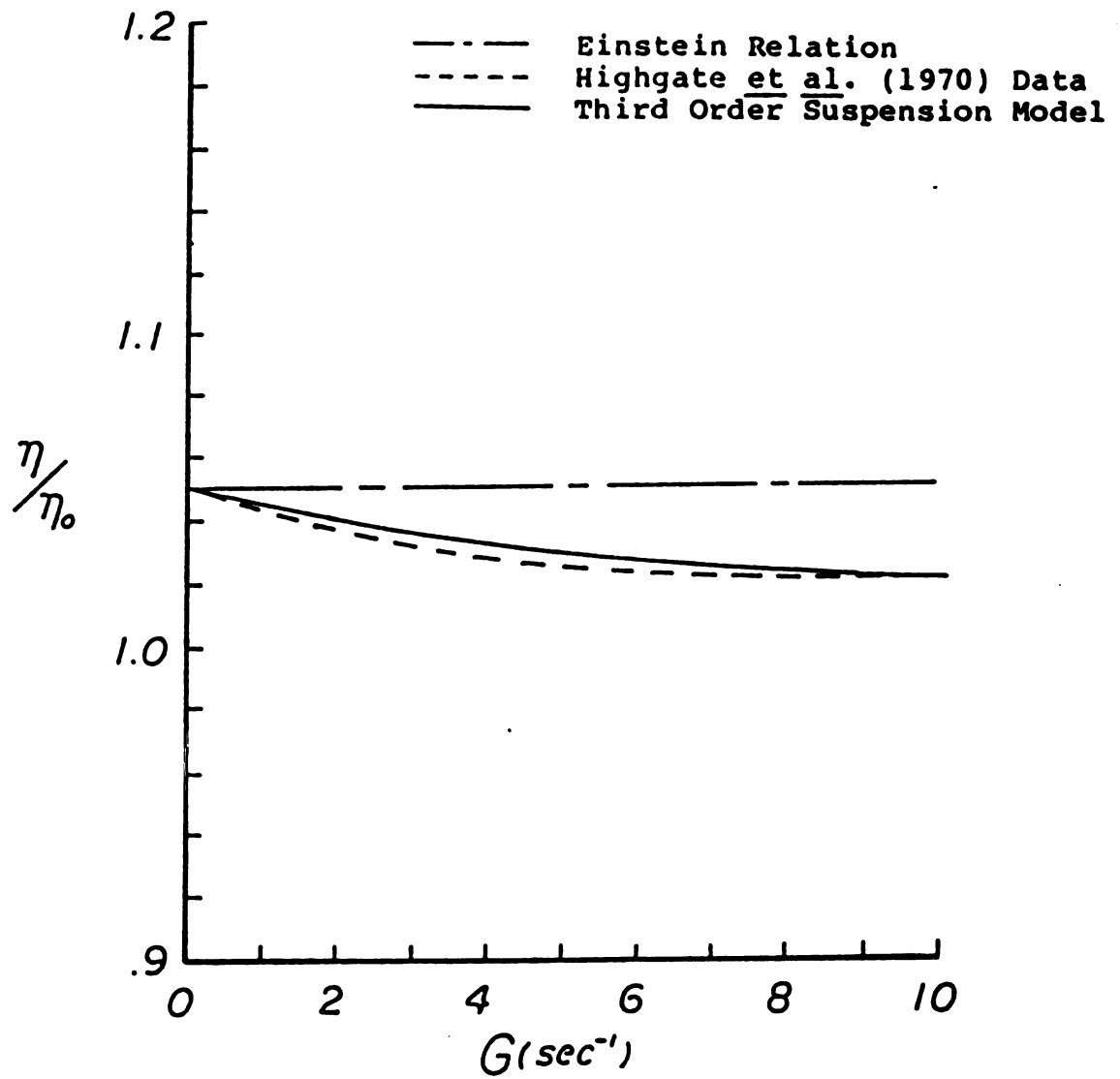


Figure 6.2 Relative Viscosity vs Shear Rate
for Rigid Sphere Suspensions

$$\phi_b = .02$$

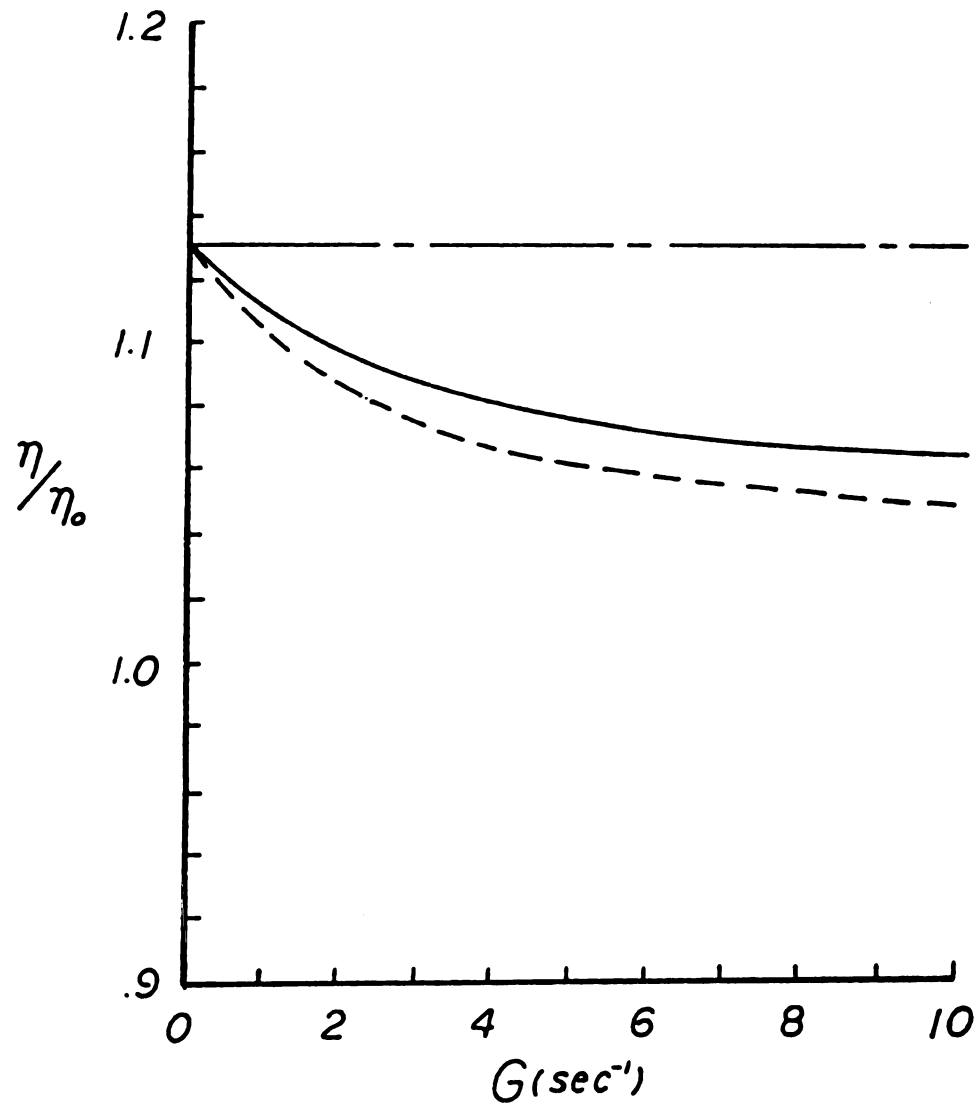


Figure 6.3

Relative Viscosity vs Shear Rate
for Rigid Sphere Suspensions

$$\phi_b = .05$$

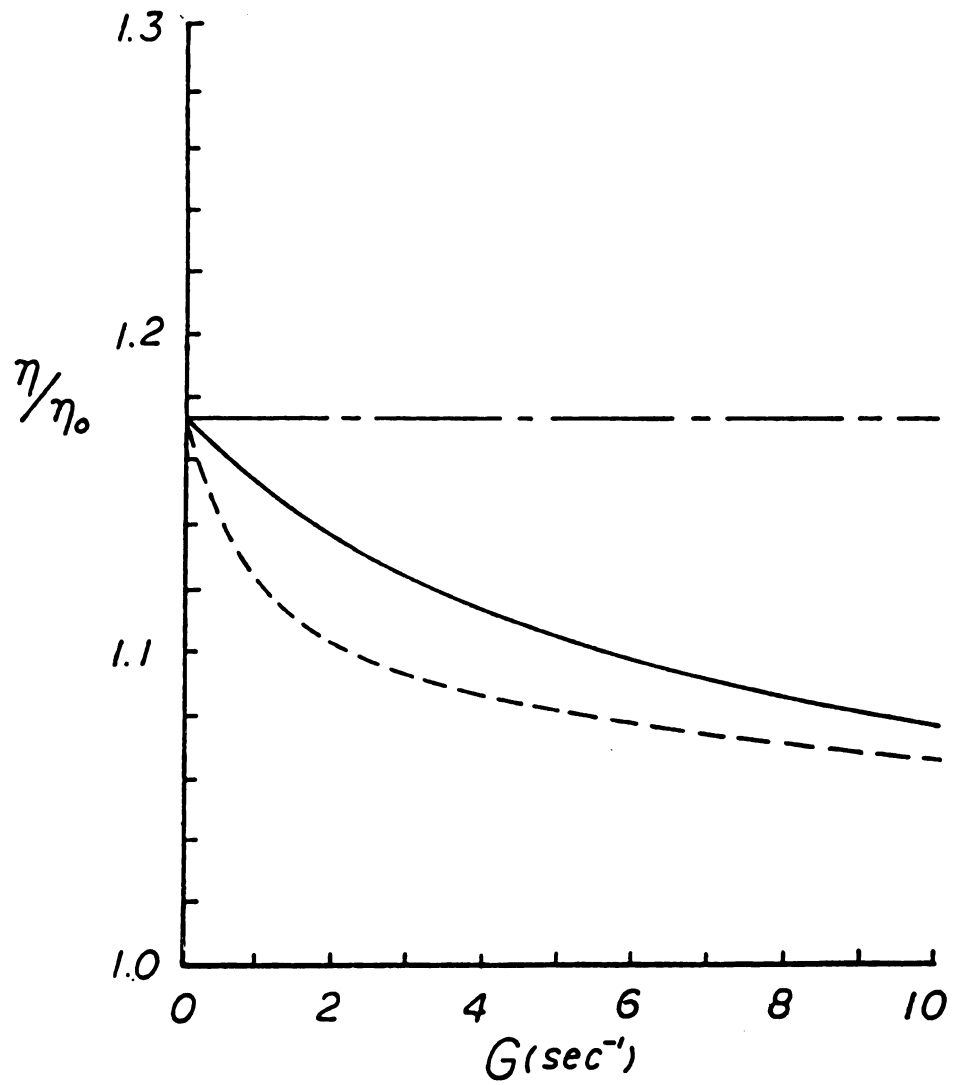


Figure 6.4

Relative Viscosity vs Shear Rate
for Rigid Sphere Suspensions

$$\phi_b = .07$$

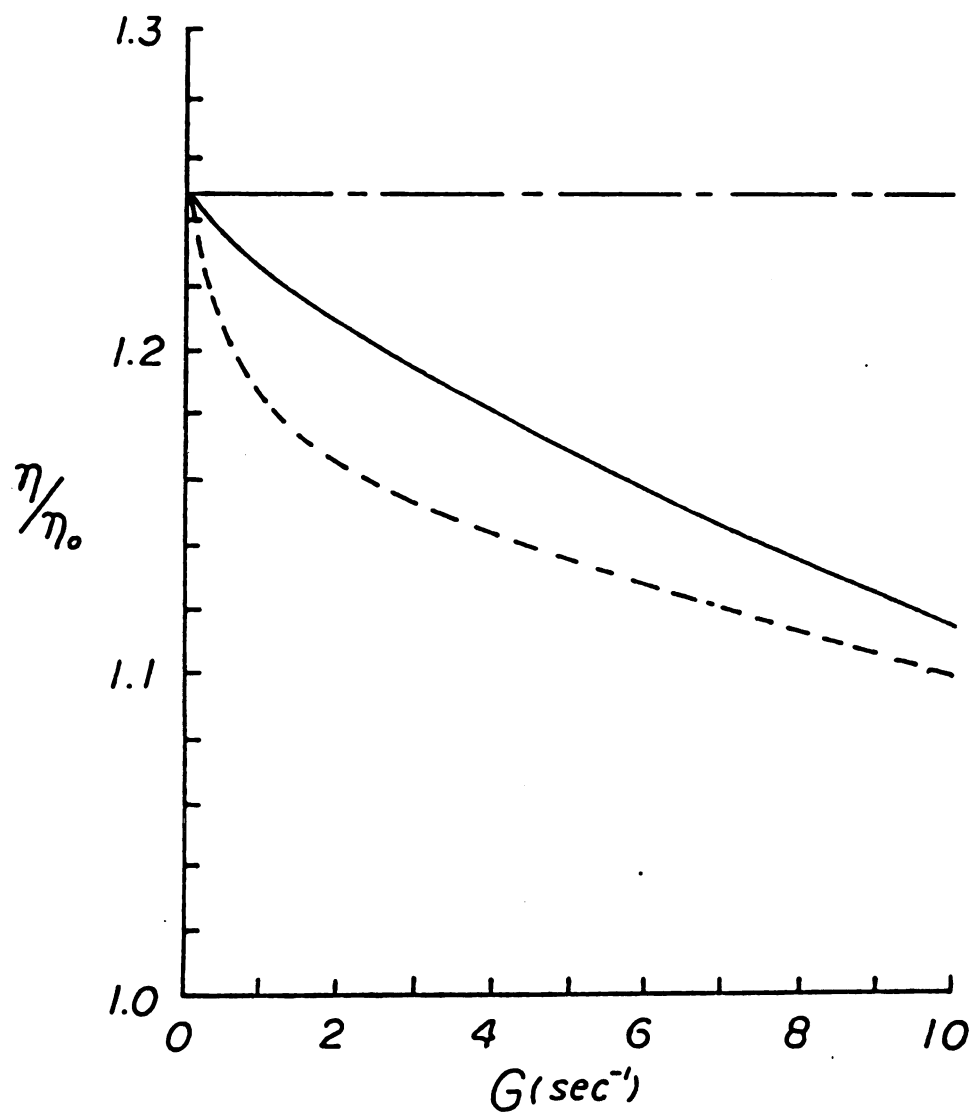


Figure 6.5

Relative Viscosity vs Shear Rate
for Rigid Sphere Suspensions

$$\phi_0 = .10$$

have been neglected in our derivation.

The relative primary normal stress difference obtained from our model is only a function of void fraction, their relation is plotted in Figure 6.6, the slope of ψ_1/ψ_{10} vs ϕ is the constant coefficient. However, Highgate's data show the relative primary normal stress difference is also a function of shear rate. This can be understood because our model is derived to $O(We^2)$, the shear rate dependent normal stress correction only comes if $O(We^3)$ is taken into consideration. Including one higher order of We means doubled terms have to be evaluated, it is not our major concern at present, since our attention is on the apparent viscosity problem. Three experimental primary normal stress ratios at zero shear rate are used to verify our coefficient, the errors are within thirteen percent. Both suspension viscosity and normal stress different relations are proved to be capable of predicting suspension rheological properties under reasonable circumstances.

For viscous droplets, the viscometric data of Newtonian polybutene drops in 2 wt. percent aqueous Separan solution were presented by Han and King (1980). The reported relative viscosity ratio κ is 0.74 for 10 percent of droplets at a shear stress of 10N/m^2 . At this shear stress, the calculated η/η_0 is 0.8 by using relation (6.48) with component viscosity ratio k , 0.015 and Weissenberg number, 1. As for normal stress coefficients, the available data have too large

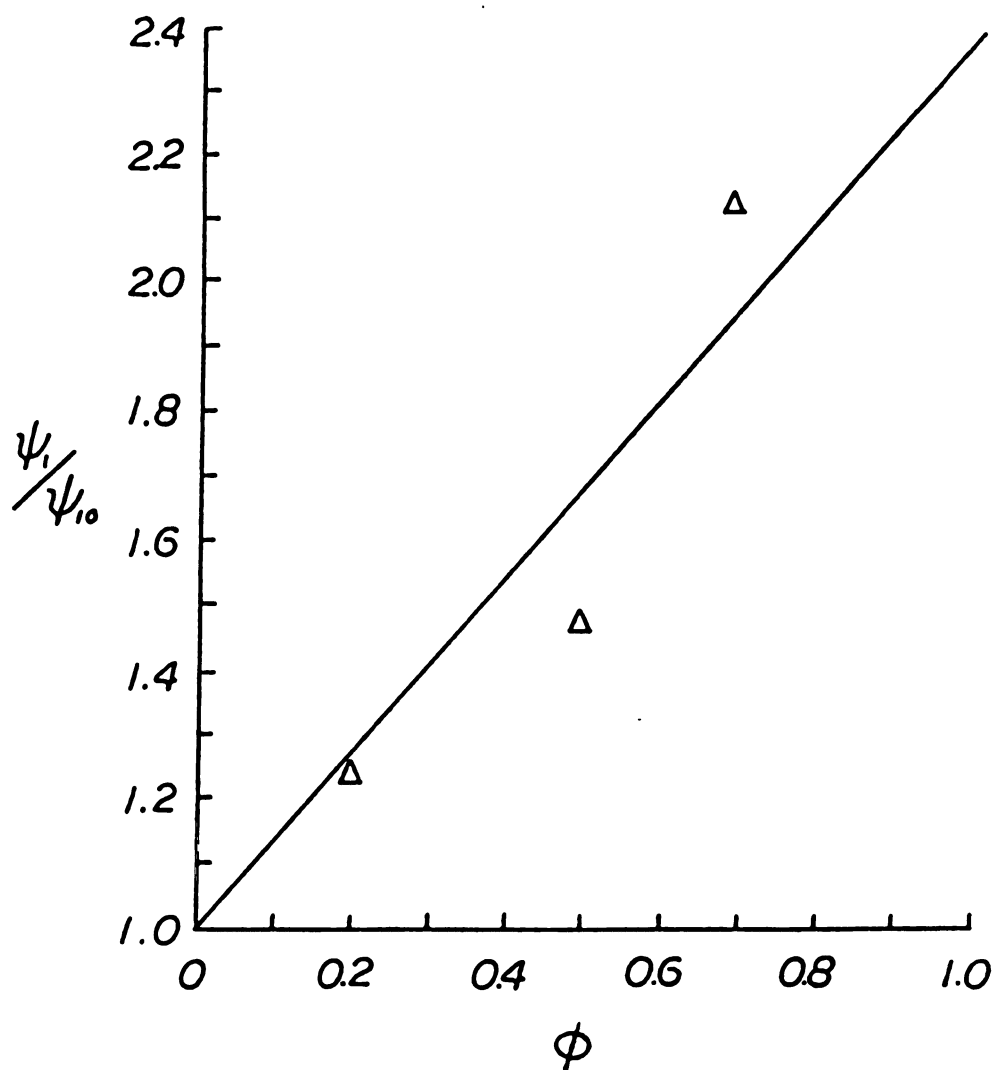


Figure 6.6

Relative Normal Stress Coefficient
vs Volume Fraction for Rigid Sphere

Δ : Highgate et al. (1970) Data
(at zero shear rate)

Weissenberg numbers to be verified by our model.

The important aspect of this study is to show that shear-dependent behavior of dilute suspension in non-Newtonian medium can be attributed to the elasticity of medium in the absence of drop deformation.

CHAPTER 7

PREDICTION OF APPARENT VISCOSITY IN TWO-PHASE FLOW

We turn now to evaluate the utility of bulk stress relations such as those in chapter six, for predicting trends in apparent viscosity of gas bubble suspensions in viscoelastic liquids flowing through a plane slit. This will be done for cases where a uniform bubbly core and a bubble free wall layer are obtained. The velocity profile for such a core annular flow may be obtained with selected expressions for the suspension viscosity and the medium viscosity, using observed values of wall shear stress τ_w , core volume fraction and core thickness Δ_c . An average flow rate over the entire gap may then be computed to yield an apparent viscosity with equation (2.1). It is appropriate to note here that there is a thin transition region, a bubble diameter, over which the void fraction changes from the core value to that in the outer layer. We shall assume that the two layers are much thicker than the bubble size and carry out the analysis as through two immiscible fluids were flowing together. Some analysis with a linear variation of void fraction in a transition region indicates that the above assumption leads to answers matching within experimental error.

In the following discussion, first, for a qualitative understanding, we explore the effect of medium elasticity on

the apparent viscosity by using the third order suspension model. Then a power law model is used to correlate observed apparent viscosity data.

7.A Third Order Suspension Model

The shear viscosity for a dilute, uniform bubbly core with low (particle) Weissenberg numbers, and a constant medium viscosity, η_0 is given by

$$\eta_c = \eta_0 \left[1 + \phi_c - F \phi_c (\psi_0 G / \eta_0)^2 \right] \quad (7.1)$$

where ψ_0 is the constant primary normal stress difference of the medium, ϕ_c is the volume fraction of bubbles in the core and F is a number of order 1 depending on the ratio of normal stress coefficients. The computations here were done only for the 2.5 wt percent Separan solution, wherein the particle Weissenberg numbers are 0.1 to 0.4 for this solution.

$$\eta_c = \eta \left[1 + \phi_c (1 - 2.5 \dot{\gamma}^2) \right] \quad (7.2)$$

$$\eta = \eta_0 \quad (7.3)$$

where η_0 is 36.8 N/m² at shear rate of 1 sec⁻¹. The velocity profile $u_z(y)$ in the outer bubble-free layer is immediately obtained with equation (7.3) as

$$u_z(y) = - \frac{\tau_w y^2}{\eta_0 h} \quad \frac{\Delta c}{2} \leq y \leq \frac{h}{2} \quad (7.4)$$

The other profile $u(y)$ in the core region is obtained by solving for $\partial u / \partial y$ from the nonlinear equation (7.5).

$$2.5 \phi_c \left| \frac{\partial u}{\partial y} \right|^3 - (1 + \phi_c) \left| \frac{\partial u}{\partial y} \right| - \frac{2\tau_w y}{\eta_0 h} = 0 \quad (7.5)$$

The roots of this cubic equation may be found in a straight forward manner, using a computer program (MODEL I, given in the Appendix E). The root selected at any y is the one closest to velocity gradient obtained with the pure medium in the entire gap. Throughout the calculation, the other two roots were very different so that the selection was unambiguous.

The results of these calculations are presented in Figure 7.1 and 7.2. Figure 7.1 shows the variation of apparent viscosity with wall shear stress at bulk void fractions about 3%. It is seen from this plot that at very low shear rates, the shear-thinning factor is not important and the apparent viscosity is higher for the suspension according to Taylor's result. At higher shear rates, the shear-thinning factor associated with medium elasticity becomes significant and leads to decreasing apparent viscosity even to lower values than that for the medium. Figure 7.2 presents a comparison of this theory and experimental data over a range of void fractions at higher wall shear stresses. The theoretical study here is qualitative correct; however,

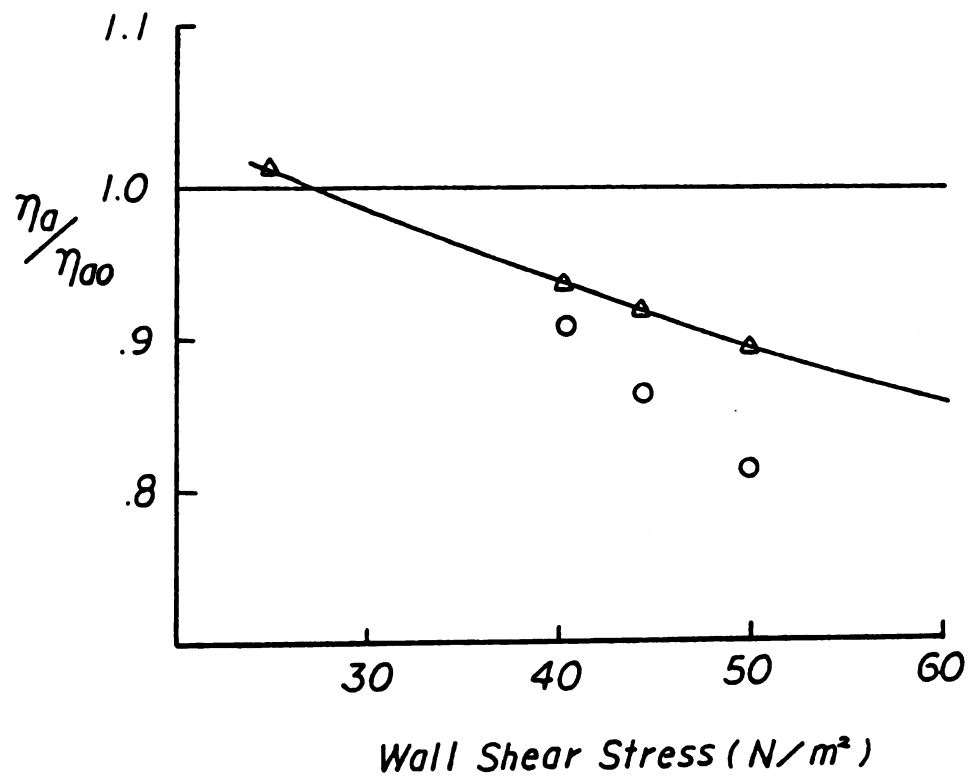


Figure 7.1 Apparent Viscosity Ratio vs
Wall Shear Stress

- Δ Theoretical Data
- \circ Experimental Data

there is a discrepancy of about 10%. It is understandable since the medium used is itself shear-thinning. The results of the computation thus far indicate that the shear-thinning factor in the suspension viscosity associated with the elastic parameters of the medium lead to a reduction in apparent viscosity which displays the trends observed in experimental data.

7.B Power Law Suspension Model

In order to obtain a close quantitative fit of the apparent viscosity data, one must take into account the shear-thinning characteristics of the medium used. This is done with the following expressions:

$$\eta_c = \eta(1 + \phi_c)(1 - b\phi_c\dot{\gamma}^m) \quad (7.6)$$

$$\eta = K\dot{\gamma}^{n-1} \quad (7.7)$$

It might be noted here that the expression in equation (7.6) is patterned on that in equation (7.2) with the exponent m and the coefficient b in the second bracket being adjustable. In the absence of medium elasticity, m and b are zero, equation (7.6) reduces to Taylor's expression. The parameters in equation (7.7) are measured directly, $k = 36.8 \text{ N sec}^{n-1}/\text{m}$ and $n = .364$ as given in Chapter 3. The velocity profile $u_2(y)$ in the outer bubble-free layer is

obtained as

$$u_2(y) = -\left(\frac{2\tau_w}{K\dot{\gamma}}\right)^{1/n} \left(\frac{n}{n+1}\right) \left[y^{1+n} - \left(\frac{h}{2}\right)^{1+n} \right] \quad (7.8)$$

and $u_1(y)$ in the core is obtained by solving the shear rate in the following equation

$$(1 + \phi_c) \left(1 - b \phi_c \left| \frac{\partial u_1}{\partial y} \right|^m \right) \left| \frac{\partial u_1}{\partial y} \right|^n - \frac{2\tau_w y}{K\dot{\gamma}} = 0 \quad (7.9)$$

The shear rate can be solved by Newton-Raphson iteration, using a computer program (MODEL II, given in the Appendix E). The best fit values of the constants b and m was found to be 2.78 and 0.4, respectively. The resulting ratio of apparent viscosity is also plotted in Figure 7.2. The trends predicted are still the same; but the qualitative fit to data is close. This set of calculations indicates that the choice of power law viscous models for both medium and suspension with an additional shear-thinning factor for the suspension reproduces observed data for the apparent viscosity in two-phase flow of these suspensions.

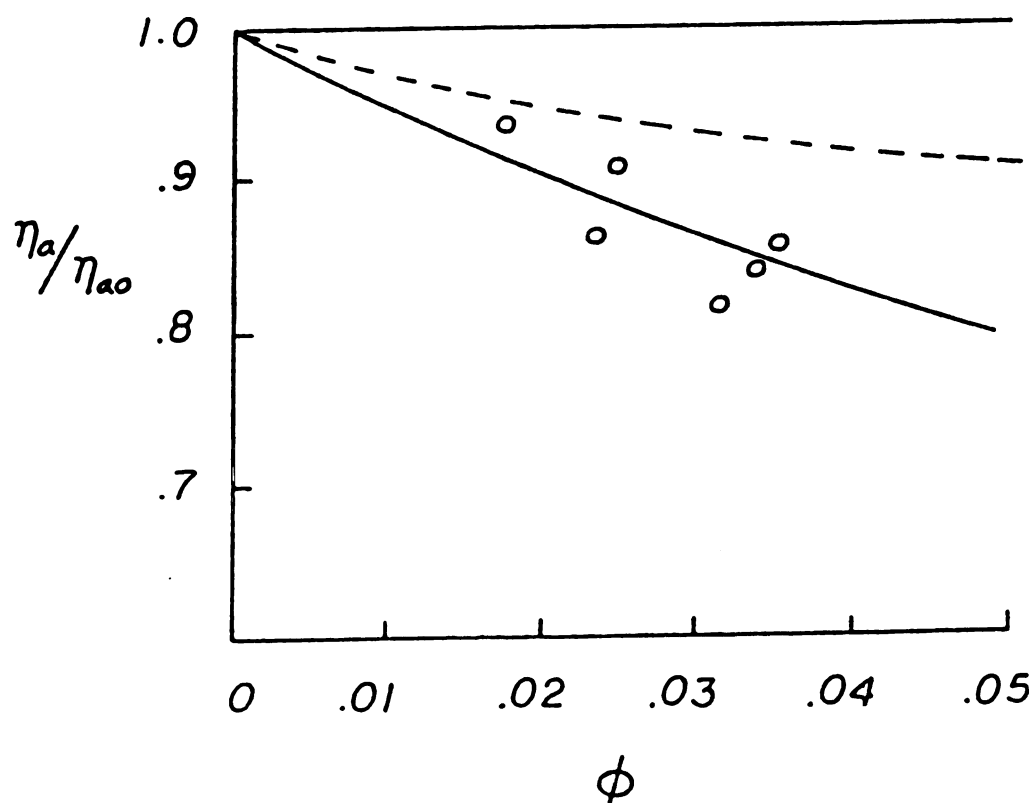


Figure 7.2 Apparent Viscosity Ratio
vs Volume Fraction

- Third Order Suspension Model
- Power Law Suspension Model
- o Experimental Data

CHAPTER 8

CONCLUSIONS AND RECOMMENDATIONS

8.A Conclusion

This investigation has focused on the isothermal development of two-phase flow structure due to bubble migration in a plane gap at Reynolds number of 10^{-3} and on the apparent viscosity associated with the flow structure. The bubble concentration profile over a 1.27cm gap containing 0.04cm gas bubble suspensions in both Newtonian and viscoelastic fluids, with bulk void fractions of 0.05 or less, is measured by a radiation attenuation technique. Although the effort involved in calibration and averaging of measurements is considered, the radiation gauge yields a resolution of less than 0.01 g/cc, provides more reliable concentration data than techniques of previous studies, i.e. light scanning or counting on photographs (without depth). The Reynolds numbers and capillary numbers based on bubble size of order 10^{-4} for all three media. Similarly, the capillary number, i.e., the ratio of viscous to surface tension forces is small (about 10^{-1}) for all three media. Measurements with a Newtonian corn syrup as a medium confirm that inertia and viscous deformation are insignificant in these experiments; so any nonhomogeneity observed in the polymer solutions may be attributed to their non-Newtonian behavior - elasticity

and shear-thinning. Gauthier et al. (1971 a,b) observed that particles migrated towards the wall of flow channel in pseudoplastic fluids. Our experimental data show that bubbles migrate towards the flow axis in the polymer solutions at the shear-thinning region. This observation confirms that the elastic effect dominates over the shear-thinning effect which leads to particle migration towards the centerline of the channel as predicted by Chan and Leal (1979). A uniform bubbly core and a bubble free layer near the wall was observed in the channel at average velocity above 1.0 cm/sec. Increasing flow rate and increasing void fraction both lead to a faster development of a uniform bubbly core and bubble free layers. The development of such flow structure is correlated well with the effect of medium elasticity and bulk void fraction. It appears that with higher recoverable shear ratios at the wall, ($S_{R,w}$), the core develops more quickly and is narrower. Higher values of bulk void fraction lead to a wider central bubbly core or thinner bubble free layers. The two-phase flow may be described by a two fluid model comprising a bubble free layer (shear-thinning) fluid and a uniform bubbly core for $S_{R,w} > 0.35$.

Next, to characterize the bubbly core, a theoretical relation was derived for the bulk stress in dilute suspensions of neutrally buoyant, uniform size, spherical Newtonian drops in a second order fluid medium. As a result

of this derivation including terms up to order We^2 , the shear viscosity of a suspension of Newtonian droplets in a second order fluid given by

$$\eta_{susp} = \eta \left[1 + \frac{5\kappa+2}{2(\kappa+1)} \phi + F(\kappa, \epsilon_1) \phi \frac{\psi_{10}^2 \dot{\gamma}^2}{4\epsilon_1^2 \eta_0^2} \right] \quad (8.1)$$

This relation includes in addition to the Taylor result, a shear-thinning factor with $F < 0$ over all the κ 's. The primary and secondary normal stress coefficients of the suspension are given by

$$\psi_{1,susp} = \psi_{10} \left[1 + f_1(\kappa, \epsilon_1) \phi \right] \quad (8.2)$$

$$\psi_{2,susp} = \psi_{20} \left[1 + f_2(\kappa, \epsilon_1) \phi \right] \quad (8.3)$$

Both normal stress coefficients are increased with volume fraction ϕ i.e. $f_1 > 0$ and $f_2 > 0$ for all the κ 's. These trends are borne out qualitatively by available viscometric data on rigid spheres and droplets. This model indicates that the shear-thinning factor for the suspension arises from the elasticity of the medium; however, the normal stress coefficients are shear-rate-dependent if the averaging procedure includes terms up to order We^3 . The relative shear viscosity expression was tested further indirectly with data from this study on the two-phase flow structure comprising a stationary uniform bubbly core and wall layers. The core thickness and core volume fraction observed for this structure in a 2.5 wt

percent Separan solution were used to calculate an apparent viscosity. The apparent viscosity observed for the suspension was up to 20 percent lower than that for the medium at a bulk volume fraction of 0.05. The predicted apparent viscosity reduction using relation (8.1) is only 10 percent below the medium value. This discrepancy is understandable since the medium used is itself shear-thinning rather than shear-rate-independent like a second order fluid. An empirical relation was proposed to correlate data

$$\eta_c = \eta(1 + \phi)(1 + b\phi_c\dot{\gamma}^n) \quad (8.4)$$

$$\eta = K\dot{\gamma}^{n-1} \quad (8.5)$$

The expression in equation (8.4) is patterned on that in equation (8.1) with the exponent n and the coefficient b being adjustable with the elasticity of the medium.

8.B Recommendations

Although there is some indication that the effects reported on two-phase structure as well as apparent viscosity are more strongly influenced by medium elasticity, the resolution into separate effects of shear-thinning and elasticity is not available. Therefore, Boger fluids (Chhabra, et al., (1980), Boger and Nguyen, (1978)) which has a constant viscosity over a wide range of shear rates, 0.5 sec^{-1} to 50 sec^{-1} , have to be used for future theoretical research in

this area. More viscometric measurements of bulk properties on uniform dilute emulsions with such fluids at low Weissenberg number are needed to confirm relations (8.1) to (8.3).

Realistically, most polymer solutions are shear-thinning, derivation of bulk stress relation for such fluids has to use a third order fluid model. The interior and exterior flow fields to a spherical drop suspended in a simple shear flow of a third order fluid can be solved by the same approach that Peery (1966) employed for the second order fluid. By the same token, the effects of deformation and elasticity can also be included into the computation. For the concentrated suspension in viscoelastic liquids, the cell model (Frankel and Acrivos (1967), Goddard (1977)) can be employed to derive the bulk stress relation. The effect of medium elasticity on the rheological functions - shear-thinning or shear thickening (Han and King (1980)) can therefore be investigated in the nondilute region.

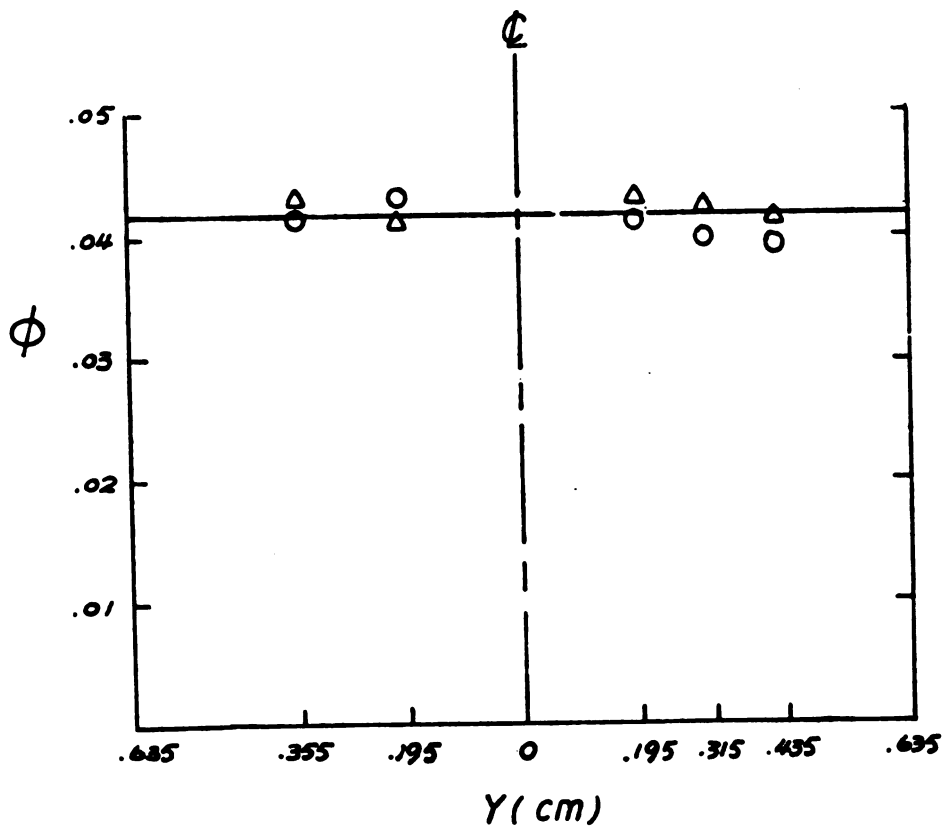
The effective viscosity of suspensions in viscoelastic fluids can be predicted by our proposed third order suspension model with data obtained from Couette viscometers. However, it is noted that migration occurs in Couette device in the presence of velocity profile curvature. The inhomogeneity existing in the wall layer near to the boundary would affect the measured viscosity. This can be correlated by incorporating the presence of the bounding walls. Tözeren

and Skalak (1977) have included the wall effect on viscosity of Newtonian suspension by considering the flow field around a sphere near a plane wall and using the surface averaging to evaluate the mean stress throughout the gap. Similar approaches can be carried out to correlate the third order suspension model by taking the wall layer into account.

APPENDIX A

SYMMETRY OF VOID FRACTION

The symmetry of void fraction profile was tested in Newtonian and polymeric suspension flows. One case is presented below.



2.5 wt Percent Separan Solution

$$\phi_b = .042, \langle v \rangle = .1 \text{ cm/sec } (tr = 63 \text{ sec})$$

The uniform core is observed around the flow axis, the concentrations above the centerline are the same as the ones below, within the resolution of radiation gauge.

APPENDIX B

EXAMPLE OF DATA ANALYSIS FOR DENSITY MEASUREMENT

The following density calculation is based on the data collected for 3.5 wt percent Separan solution with $\phi_b = .035$ and $\langle V \rangle = .91 \text{ cm/sec}$ (Figure 5.23). Radiation counts recorded at entrance at two axial locations are listed in the tables.

Number	SLOT 1			SLOT 2		
	Entrance	Upstream	Downstream	Entrance	Upstream	Downstream
1	7953	8125	8161	7521	7512	7480
2	7918	8053	7872	7434	7505	7492
3	8010	7982	8169	7449	7549	7443
4	7871	7392	8116	7472	7399	7622
5	8025	8077	7930	7484	7468	7625
6	7897	8071	8161	7402	7496	7434
7	7988	8080	8060	7494	7479	7484
8	8049	7927	8076	7540	7684	7581
9	7955	8110	7985	7540	7442	7521
10	8114	8147	8033	7534	7471	7534
11	7992	8007	8044	7614	7805*	7440
12	7994	7989	7962	7552	7617	7645
13	7924	8018	8119	7592	7634	7590
14				7494	7465	7514
Mean	7976	8037.1	8052	7507	7537.5	7528.9
Standard Deviation	66.7	75.6	98.7	56.6	110.4	72.4
Mean	7976	8037.1	8052	7507	7517	7528.9

* Datum has to be rejected according to Chauvenet criterion

Number	SLOT 3			SLOT 4		
	Entrance	Upstream	Downstream	Entrance	Upstream	Downstream
1	6880	7102	6941	7750	7854	7810
2	6813	6858	6886	7826	7772	7690
3	6842	6953	6769	7737	7740	7750
4	7017	6883	6997	7731	7869	7830
5	6901	6949	6977	7871	7827	7719
6	6894	6713	6974	7891	7721	7741
7	7051	6869	6851	7758	7868	7796
8	6949	7006	6936	7725	7623	7830
9	6971	6954	6839	7719	7841	7756
10	6882	6842	6861	7914	7554	7820
11	6763	6955	6908	7755	7698	7722
12	6948	6847	6984	7714	7783	7622
13	6853	6803	6903	7865	7609	7726
Mean	6905	6903	6909	7788.9	7751.3	7754.8
Standard Deviation	30.9	97.3	67.5	75.2	104.3	61.6

From the mean and standard deviation, we can reject the datum deviates too much from the mean. Using equation (4.12) and linear mass attenuation coefficients measured from the calibration, the density variations can be computed from the intensity difference between the downstream locations and entrance.

Slot 1	Upstream	$\Delta\rho = -\ln(8037.1/7976)/.659 = -.0116$
	Downstream	$\Delta\rho = -\ln(8052/7976)/.659 = -.0144$
Slot 2	Upstream	$\Delta\rho = -\ln(7517/7507)/.557 = -.0024$
	Downstream	$\Delta\rho = -\ln(7528.9/7507)/.557 = -.005$
Slot 3	Upstream	$\Delta\rho = -\ln(6903/6905)/.655 = .0004$
	Downstream	$\Delta\rho = -\ln(6909/6905)/.655 = -.001$
Slot 4	Upstream	$\Delta\rho = -\ln(7751.3/7788.9)/.704 = .007$
	Downstream	$\Delta\rho = -\ln(7754.8/7788.9)/.704 = .006$

The void fractions can then be evaluated by equation (4.7) and plotted.

APPENDIX C

FLOW FIELD OF A NEWTONIAN SPHERICAL DROP IN A SECOND ORDER FLUID UNDERGOING A SIMPLE SHEAR FLOW

External Flow Field

Zeroth Order Solution

$$u_0 = \left[\left(\frac{5}{2r^2} - \frac{5}{2r^3} \right) (\underline{\alpha} : \underline{r} \underline{r}) \underline{r} + \left(-\frac{1}{2r^3} + 1 \right) \underline{\alpha} \cdot \underline{r} + \left(-\frac{1}{2r^3} \right) \underline{\alpha}^T \cdot \underline{r} \right]$$

$$p_0 = -\frac{5}{r^3} (\underline{\alpha} : \underline{r} \underline{r})$$

First Order Solution

$$\begin{aligned} u_1 = \frac{1}{4(k+1)^2} & \left[\left(\frac{20C_0}{r^{12}} - \frac{C_2}{2r^{11}} - \frac{8C_3}{r^{10}} - \frac{7C_4}{18r^9} \right) (\underline{\alpha} : \underline{r} \underline{r}) \underline{r} + \left(-\frac{5C_1}{r^{10}} + \frac{C_5}{9r^9} \right. \right. \\ & - \frac{3C_3}{2r^8} + \frac{C_4}{18r^7} \bigg) (\underline{\alpha} : \underline{r} \underline{r}) (\underline{\alpha} \cdot \underline{r} + \underline{\alpha}^T \cdot \underline{r}) + \left(-\frac{C_1}{r^{10}} + \frac{C_2}{18r^9} - \frac{3C_3}{2r^8} + \frac{C_4}{42r^7} \right. \\ & + \frac{C_6}{70r^6} \bigg) (\underline{\alpha} \cdot \underline{r} \cdot \underline{\alpha} \cdot \underline{r}) \underline{r} + \left(-\frac{2C_1}{r^{10}} + \frac{C_2}{9r^9} - \frac{3C_3}{r^8} + \frac{C_4+C_7}{42r^7} + \frac{C_8+C_9}{70r^6} \right) \\ & (\underline{\alpha}^T \cdot \underline{r} \cdot \underline{\alpha} \cdot \underline{r}) \underline{r} + \left(-\frac{C_1}{r^{10}} + \frac{C_2}{18r^9} - \frac{3C_3}{2r^8} + \frac{C_4}{42r^7} + \frac{C_8}{70r^6} \right) (\underline{\alpha} \cdot \underline{r} \cdot \underline{\alpha} \cdot \underline{r}) \underline{r} + \\ & \left(-\frac{2C_3}{63r^7} + \frac{C_4}{r^6} + \frac{C_9+C_{10}}{630r^5} \right) (\underline{\alpha} \cdot \underline{\alpha} \cdot \underline{r}) + \left(-\frac{C_2}{63r^7} + \frac{C_3}{2r^6} - \frac{C_9}{630r^5} \right) (\underline{\alpha}^T \cdot \underline{\alpha} \cdot \underline{r}) + \\ & \left(-\frac{C_2}{63r^7} + \frac{C_3}{2r^6} - \frac{C_{10}}{630r^5} \right) (\underline{\alpha} \cdot \underline{\alpha}^T \cdot \underline{r}) + \left(-\frac{C_2}{126r^7} + \frac{C_3}{3r^6} - \frac{C_9+C_{10}}{630r^5} - \frac{C_2+C_9}{210r^6} \right) \\ & \left. (\underline{\alpha} : \underline{\alpha} + \underline{\alpha} : \underline{\alpha}^T) \underline{r} \right] \end{aligned}$$

$$\begin{aligned}
P_1 = & \frac{1}{4(k-1)^2} \left[\left(\frac{90C_1}{r^{14}} - \frac{10C_2}{r^{12}} + \frac{2C_3}{r^{10}} - \frac{7C_4}{9r^9} + \frac{40C_5}{r^7} \right) (\underline{\alpha} : \underline{r} \underline{r}) + \right. \\
& \left(\frac{30C_1}{r^{12}} - \frac{2C_2}{r^{10}} + \frac{C_6}{2r^8} + \frac{C_4}{9r^7} - \frac{C_7}{35r^5} \right) (\underline{\alpha} \cdot \underline{r} \cdot \underline{\alpha} \cdot \underline{r}) + \left(\frac{60C_1}{r^{12}} - \frac{4C_2}{r^{10}} \right. \\
& \left. + \frac{C_6}{r^8} + \frac{2C_4}{9r^7} - \frac{C_7 \cdot C_8}{35r^5} \right) (\underline{\alpha} \cdot \underline{r} \cdot \underline{\alpha}^T \cdot \underline{r}) + \left(\frac{30C_1}{r^{12}} - \frac{2C_2}{r^{10}} + \frac{C_6}{2r^8} + \frac{C_4}{9r^7} \right. \\
& \left. - \frac{C_8}{35r^5} \right) (\underline{\alpha}^T \cdot \underline{r} \cdot \underline{\alpha} \cdot \underline{r}) + \left(\frac{2C_1}{r^{10}} - \frac{2C_4}{45r^5} + \frac{2C_2}{35r^5} \right) (\underline{\alpha} : \underline{\alpha} + \underline{\alpha} : \underline{\alpha}^T) \Big]
\end{aligned}$$

Internal Flow Field

Zeroth Order Solution

$$\underline{u}_0 = \frac{1}{k+1} \left[-(\underline{\alpha} : \underline{r} \underline{r}) \underline{r} + \frac{1}{4}(5r^2 + 2k - 1) \underline{\alpha} \cdot \underline{r} + \frac{1}{4}(5r^2 - 2k - 5) \underline{\alpha}^T \cdot \underline{r} \right]$$

$$P_0 = \frac{21}{2(k-1)} (\underline{\alpha} : \underline{r} \underline{r})$$

First Order Solution

$$\begin{aligned}
\underline{u}_1 = & \frac{1}{4(k-1)^2} \left[\frac{C_1'}{9} (\underline{\alpha} : \underline{r} \underline{r}) \underline{r} + \left(\frac{2C_1' r^2}{36} - \frac{5C_1'}{36} \right) (\underline{\alpha} : \underline{r} \underline{r}) (\underline{\alpha} \cdot \underline{r} + \underline{\alpha}^T \cdot \underline{r}) + \left(\frac{C_3' r^2}{84} \right. \right. \\
& \left. \left. - \frac{C_4'}{1260} \right) (\underline{\alpha} \cdot \underline{r} \cdot \underline{\alpha} \cdot \underline{r}) \underline{r} + \left(\frac{C_1' r^2}{42} - \frac{C_4' + C_5'}{1260} \right) (\underline{\alpha}^T \cdot \underline{r} \cdot \underline{\alpha} \cdot \underline{r}) \underline{r} + \left(\frac{C_3' r^2}{84} - \frac{C_5'}{1260} \right) \right. \\
& \left(\underline{\alpha} \cdot \underline{r} \cdot \underline{\alpha} \cdot \underline{r} \right) \underline{r} + \left(\frac{C_6' r^2}{18} + \frac{(C_7' + C_8') r^2}{252} - \frac{3(C_6' + C_8')}{70} \right) (\underline{\alpha} \cdot \underline{\alpha} \cdot \underline{r}) + \left(\frac{C_6' r^2}{36} + \frac{C_7' r^2}{252} \right. \\
& \left. - \frac{3C_8'}{70} \right) (\underline{\alpha} \cdot \underline{\alpha} \cdot \underline{r}) + \left(\frac{C_6' r^2}{36} + \frac{C_7' r^2}{252} - \frac{3C_8'}{70} \right) (\underline{\alpha} \cdot \underline{\alpha} \cdot \underline{r}) + \left(-\frac{C_6' r^2}{126} + \frac{(C_7' + C_8') r^2}{1260} \right. \\
& \left. + \frac{C_6' + C_8'}{70} \right) (\underline{\alpha} : \underline{\alpha} + \underline{\alpha} : \underline{\alpha}) \underline{r} \Big]
\end{aligned}$$

$$P' = \frac{1}{4(\kappa-1)^2} \left[-\frac{C_1'}{36} (\underline{\alpha} \cdot \underline{r} \underline{r})^2 + \left(\frac{C_2' r^2}{252} - \frac{3C_3'}{10} \right) (\underline{\alpha} \cdot \underline{r} \cdot \underline{\alpha} \cdot \underline{r}) + \left(\frac{C_4' r^4}{126} - \frac{3(C_5' \kappa + C_6')}{10} \right) \right. \\ \left. (\underline{\alpha} \cdot \underline{r} \cdot \underline{\alpha} \cdot \underline{r}) + \left(\frac{C_7' r^4}{252} - \frac{3C_8'}{10} \right) (\underline{\alpha} \cdot \underline{r} \cdot \underline{\alpha} \cdot \underline{r}) + \left(-\frac{C_9' r^4}{252} - \frac{C_{10}' r^2}{5} \right) (\underline{\alpha} \cdot \underline{\alpha} + \underline{\alpha} \cdot \underline{\alpha}^T) \right]$$

Coefficients

$$C_1 = (5\kappa^2 + 2\kappa) + E_1(5\kappa^2 + 2\kappa)$$

$$C_2 = (500\kappa^2 + 320\kappa + 32) + E_1(500\kappa^2 + 180\kappa + 32)$$

$$C_3 = (25\kappa^2 + 20\kappa + 4) + E_1(25\kappa^2 + 20\kappa + 4)$$

$$C_4 = (130\kappa^2 + 112\kappa + 40) + E_1(130\kappa^2 + 252\kappa + 40)$$

$$C_5 = (550\kappa^2 + 434\kappa + 224) + E_1(350\kappa^2 + 504\kappa + 224)$$

$$C_6 = (50\kappa^2 + 130\kappa - 64) + E_1(260\kappa^2 + 340\kappa - 64)$$

$$C_7 = (550\kappa^2 + 434\kappa + 224) + E_1(770\kappa^2 + 924\kappa + 224)$$

$$C_8 = (50\kappa^2 + 130\kappa - 64) + E_1(-160\kappa^2 - 80\kappa - 64)$$

$$C_9 = (2390\kappa^2 + 1820\kappa + 1064) + E_1(1190\kappa^2 + 1260\kappa + 1064)$$

$$C_{10} = (90\kappa + 134) + E_1(3710\kappa^2 + 3780\kappa + 1064)$$

$$C_{11} = (2\kappa^2) + E_1(3\kappa^2)$$

$$C_{12} = (40\kappa^2 + 16\kappa) + E_1(55\kappa^2 + 22\kappa)$$

$$C_{13} = (150\kappa^2 + 120\kappa + 24) + E_1(125\kappa^2 + 100\kappa + 20)$$

$$C_{14} = (490\kappa^2 + 472\kappa + 40) + E_1(670\kappa^2 + 792\kappa + 40)$$

$$C_{15} = (5K^2 + 7K + 2) + E_1(10K^2 + 14K + 4)$$

$$C_{16} = (25K^2 + 20K + 4) + E_1(50K^2 + 40K + 8)$$

$$C_{17} = (1000K^2 + 1340K + 484) + E_1(1840K^2 + 2600K + 904)$$

$$C_{18} = (1000K^2 + 1340K + 484) + E_1(1560K^2 + 2040K + 624)$$

$$C_{19} = (100K^2 + 120K + 68) + E_1(100K^2 + 120K + 68)$$

and

$$C'_1 = (5K^2 - 32K + 4) + E_1(-5K^2 + 108K + 4)$$

$$C'_2 = (5K^2 + 172K - 4) + E_1(5K^2 - 108 - 4)$$

$$C'_3 = (5K^2 - 32K + 172) + E_1(-5K^2 + 108K + 4)$$

$$C'_4 = (775K^2 - 1420K + 2332) + E_1(3295K^2 + 8100K - 188)$$

$$C'_5 = (775K^2 - 1420K + 2332) + E_1(-1745K^2 + 3060K - 188)$$

$$C'_6 = (5K^2 - 32K - 122) + E_1(-5K^2 + 108K + 4)$$

$$C'_7 = (475K^2 + 2300K + 1166) + E_1(1735K^2 + 2160K - 164)$$

$$C'_8 = (25K^2 + 80K + 27) + E_1(95K^2 + 150K - 8)$$

$$C'_9 = (475K^2 + 2300K + 1166) + E_1(-785K^2 - 360K - 164)$$

$$C'_{10} = (25K^2 + 80K + 27) + E_1(-45K^2 + 10K - 8)$$

$$C'_{11} = (275K^2 - 1760K - 968) + E_1(-275K^2 + 5940K + 220)$$

$$G'_2 = (275K^2 - 1760K + 14584) + E_1(-275K^2 + 5940K + 220)$$

$$G'_3 = (25K^2 + 80K - 103) + E_1(95K^2 + 150K - 8)$$

$$G'_4 = (25K^2 + 80K - 103) + E_1(-45K^2 + 10K - 8)$$

$$G'_5 = (55K^2 - 352K - 4024) + E_1(-55K^2 + 1188K + 44)$$

$$G'_6 = (25K^2 + 80K + 107) + E_1(25K^2 + 80K - 8)$$

APPENDIX D

EVALUATION OF \underline{J}_1 and \underline{J}_2

Exterior Flow Field Terms

$O(\lambda^0)$

$$\int_{S_0} \underline{n} \cdot (-P_0 \underline{I}) \underline{r} dS = \frac{4\pi}{3} \left[\frac{5K+2}{5K+5} (\underline{\alpha} + \underline{\alpha}^T) \right]$$

$$\int_{S_0} \underline{A}_{10} \cdot \underline{n} \underline{r} dS = \frac{4\pi}{3} \left[\frac{5K+4}{10K+10} (\underline{\alpha} + \underline{\alpha}^T) \right]$$

$$\int_{S_0} (\underline{n} \underline{u}_0 + \underline{u}_0 \underline{n}) dS = \frac{4\pi}{3} \left[\frac{3}{5K+5} (\underline{\alpha} + \underline{\alpha}^T) \right]$$

$O(\lambda)$

$$\begin{aligned} \int_{S_0} \underline{n} \cdot (-P_1 \underline{I}) \underline{r} dS = \frac{4\pi}{3} \left\{ \frac{1}{(K+1)^2} \left[(2.95K^2 + 0.4K + 0.92) + \epsilon_1 (4.3K^2 + 0.68K + 0.84) \right] \right. \\ \left. (\underline{\alpha} : \underline{\alpha}^T) \underline{I} + [(0.39K^2 - 0.89K + 0.65) + \epsilon_1 (0.53K^2 - 2.11K \right. \\ \left. + 0.67)] (\underline{\alpha}^T \cdot \underline{\alpha}) - [(0.39K^2 - 0.89K + 0.65) + \epsilon_1 (1.33K \right. \\ \left. - 0.51K + 1.47)] (\underline{\alpha} \cdot \underline{\alpha}^T) \right\} \end{aligned}$$

$$\begin{aligned} \int_{S_0} \underline{A}_{11} \cdot \underline{n} \underline{r} dS = \frac{4\pi}{3} \left\{ \frac{1}{(K-1)^2} \left[(-1.23K^2 + 0.64K + 0.15) + \epsilon_1 (7.49K^2 + 8.36K \right. \right. \\ \left. \left. + 3.47) \right] (\underline{\alpha} : \underline{\alpha}^T) \underline{I} + [(0.43K^2 + 3.13K - 0.14) + \epsilon_1 (\right. \\ \left. 0.13K^2 - 0.8K - 0.14)] (\underline{\alpha}^T \cdot \underline{\alpha}) + [(-4.31K^2 - 0.28K - 1.98) \right. \\ \left. + \epsilon_1 (0.73K^2 - 0.26K - 0.14)] (\underline{\alpha} \cdot \underline{\alpha}^T) \right\} \end{aligned}$$

$$\int_{S_0} (\underline{A}_{10} \cdot \underline{A}_{10}) \cdot \underline{n} \, dS = \frac{4\pi}{3} \left\{ \frac{1}{(K+1)^2} \left[(1.79K^2 - K + 1.03)(\underline{\alpha} : \underline{\alpha}^T) \underline{I} + (1.79K^2 + 2.5K + 2.06)(\underline{\alpha}^T \underline{\alpha} + \underline{\alpha} \cdot \underline{\alpha}^T) \right] \right\}$$

$$\int_{S_0} \underline{A}_{20} \cdot \underline{n} \, dS = \frac{4\pi}{3} \left\{ \frac{1}{(K+1)^2} \left[(3.57K^2 - 1.29K + 0.63)(\underline{\alpha} : \underline{\alpha}^T) \underline{I} + (3.64K^2 + 8.13K + 1.26)(\underline{\alpha}^T \underline{\alpha}) + (0.64K^2 - 0.87K - 1.14)(\underline{\alpha} \cdot \underline{\alpha}^T) \right] \right\}$$

$$\int_{S_0} (\underline{n} \underline{u} + \underline{u} \underline{n}) \, dS = \frac{4\pi}{3} \left\{ \frac{1}{(K+1)^2} \left(\left[(-0.74K - 0.36) + E_1(-7.93K^2 - 8.46K - 3.33) \right] (\underline{\alpha} : \underline{\alpha}^T) \underline{I} + \left[(1.37K^2 + 3.67K - 0.37) + E_1(4.83K^2 + 9K - 0.37) \right] (\underline{\alpha}^T \underline{\alpha}) + \left[(8.95K^2 + 9.27K + 2.59) + E_1(-2.37K^2 + 1.8K - 0.37) \right] (\underline{\alpha} \cdot \underline{\alpha}^T) \right) \right\}$$

$$\int_{S_0} \underline{n} \cdot (\underline{u}_0 \underline{A}_{10}) \, dS = 0$$

$$\int_{S_0} (\underline{A}_{10} \cdot \underline{A}_{11} + \underline{A}_{11} \cdot \underline{A}_{10}) \cdot \underline{n} \, dS = \frac{4\pi}{3} \left\{ \frac{1}{(K+1)^3} \left[(-6.75K^3 - 12.42K^2 + 21.19K - 3.79) + E_1(6.39K^3 + 18.87K^2 + 28.1K + 3.52) \right] G^2(\underline{\alpha} + \underline{\alpha}^T) \right\}$$

$$\int_{S_0} \underline{n} \cdot (\underline{u}_0 \underline{A}_{11}) \, dS = 0$$

$O(\lambda^2)$

$$\int_{S_0} \underline{A}_{20} \cdot \underline{n} dS = \frac{4\pi}{3} \left\{ \frac{1}{(\kappa+1)^3} \left[(-3\kappa^3 + 1.26\kappa^2 + 24.97\kappa - 8.28) + \epsilon_1(-1.94\kappa^3 + 8\kappa^2 + 20\kappa + 7.8) \right] G^2(\underline{\alpha} + \underline{\alpha}^T) \right\}$$

$$\int_{S_0} (\underline{U}_1 \cdot \underline{A}_{10}) dS = \frac{4\pi}{3} \left\{ \frac{1}{(\kappa+1)^3} \left[(0.64\kappa^3 + 1.5\kappa^2 + 0.83\kappa + 0.3) + \epsilon_1(-2.92\kappa^3 - 5.92\kappa^2 - 4.29\kappa - 1.27) \right] G^2(\underline{\alpha} + \underline{\alpha}^T) \right\}$$

Internal Flow Field Terms

$O(\lambda^0)$

$$\int_{V_0} (\underline{A}'_{10} \cdot \underline{A}'_{10}) dV = \frac{4\pi}{3} \left\{ \frac{1}{(\kappa+1)^3} \left[(0.24)(\underline{\alpha} : \underline{\alpha}^T) \underline{I} + (2.04)(\underline{\alpha}^T \cdot \underline{\alpha} + \underline{\alpha} \cdot \underline{\alpha}^T) \right] \right\}$$

$$\int_{V_0} (\underline{A}'_{10} \cdot \nabla \underline{U}_0^T + \nabla \underline{U}_0 \cdot \underline{A}'_{10}) dV = \frac{4\pi}{3} \left\{ \frac{1}{(\kappa+1)^3} \left[(0.54)(\underline{\alpha} : \underline{\alpha}^T) \underline{I} + (0.6\kappa + 1.11)(\underline{\alpha}^T \cdot \underline{\alpha}) + (-0.6\kappa - 0.09)(\underline{\alpha} \cdot \underline{\alpha}^T) \right] \right\}$$

$O(\lambda)$

$$\int_{V_0} (\underline{A}'_{10} \cdot \underline{A}'_{11} + \underline{A}'_{11} \cdot \underline{A}'_{10}) dV = \frac{4\pi}{3} \left\{ \frac{1}{(\kappa+1)^3} \left[(4.62\kappa^2 + 10.76\kappa + 9.79) + \epsilon_1(3.22\kappa^2 + 25.63\kappa - 0.73) \right] G^2(\underline{\alpha} + \underline{\alpha}^T) \right\}$$

$$\begin{aligned}
& \int_{V_0} (\underline{A}'_{10} \cdot \nabla \underline{U}'_i + \nabla \underline{U}'_i \cdot \underline{A}'_{10} + \underline{A}'_{11} \cdot \nabla \underline{U}'_0 + \nabla \underline{U}'_0 \cdot \underline{A}'_{11}) dV \\
&= \frac{4\pi}{3} \left\{ \frac{1}{(K+1)^3} [(0.15K^3 + 1.77K^2 - 0.19K + 2.23) + \epsilon_1(-0.2K^3 - 0.27K^2 + 10.73K \right. \\
&\quad \left. + 0.25)] G^2(\underline{\alpha} + \underline{\alpha}^T) \right\}
\end{aligned}$$

Summation of $O(\lambda^0)$:

$$\begin{aligned}
& \frac{1}{V} \sum \left\{ \int_{S_0} \underline{n} \cdot (-P \underline{I}) \underline{r} dS + \int_{S_0} \underline{A}_{10} \cdot \underline{n} \underline{r} dS - \int_{S_0} (\underline{n} \underline{u}_0 + \underline{u}_0 \underline{n}) dS \right\} \\
&= \frac{\Phi}{K+1} \left(\frac{5K+2}{2} \right) (\underline{\alpha} + \underline{\alpha}^T)
\end{aligned}$$

Summation of $O(\lambda)$:

$$\begin{aligned}
& \frac{\lambda}{V} \sum \left\{ \int_{S_0} \underline{n} \cdot (-P \underline{I}) \underline{r} dS + \int_{S_0} \underline{A}_{11} \cdot \underline{n} \underline{r} dS + \int_{S_0} (\underline{A}_{10} \cdot \underline{A}_{10}) \cdot \underline{n} \underline{r} dS \right. \\
&\quad + \epsilon_1 \int_{S_0} \underline{A}_{20} \cdot \underline{n} \underline{r} dS - \int_{S_0} (\underline{n} \underline{u}_1 + \underline{u}_1 \underline{n}) dS - \epsilon_1 \int_{S_0} \underline{n} \cdot (\underline{u}_0 \underline{A}_{10}) dS \\
&\quad \left. - \int_{V_0} \underline{A}'_{10} \cdot \underline{A}'_{10} dV - \epsilon_1 \int_{V_0} (\underline{A}'_{10} \cdot \nabla \underline{U}'_0 + \nabla \underline{U}'_0 \cdot \underline{A}'_{10}) dV \right\} \\
&= \frac{\lambda \Phi}{(K+1)^2} \left\{ [(3.505K^2 - 7.835K - 2.22) + \epsilon_1(22.28K^2 + 16.21 + 7.73)(\underline{\alpha} : \underline{\alpha}^T)] \underline{I} \right. \\
&\quad + [(1.24K^2 + 1.07K + 0.16) + \epsilon_1(-0.53K^2 - 4.38K + 1.05)(\underline{\alpha}^T \cdot \underline{\alpha}) \\
&\quad \left. + [(-11.08K^2 - 7.93K - 3.91) + \epsilon_1(5.07K^2 - 2.84K + 0.65)(\underline{\alpha} \cdot \underline{\alpha}^T)] \right\}
\end{aligned}$$

Summation of $O(\lambda^2)$

$$\begin{aligned}
& \frac{\lambda^2}{2} \sum \left\{ \int_{S_0} (\underline{A}_{10} \cdot \underline{A}_{11} + \underline{A}_{11} \cdot \underline{A}_{10}) \cdot \underline{n} \, dS + \epsilon_1 \int_{S_0} \underline{A}_{11} \cdot \underline{n} \, dS - \epsilon_1 \int_{S_0} \underline{n} \cdot (\underline{u}_0 \underline{A}_{10} \right. \\
& \quad + \underline{u}_0 \underline{A}_{11}) \, dS - \int_{V_0} (\underline{A}'_{10} \cdot \underline{A}'_{11} + \underline{A}'_{11} \cdot \underline{A}'_{10}) \, dV - \epsilon_1 \int_{V_0} (\nabla \underline{u}_0 \cdot \underline{A}'_{11} + \nabla \underline{u}_1 \cdot \underline{A}'_{10} + \underline{A}'_{11} \cdot \nabla \underline{u}_0 \\
& \quad \left. + \underline{A}'_{10} \cdot \nabla \underline{u}_1) \, dV \right\} \\
& = \frac{\lambda^2 \phi}{(\kappa+1)^3} \left[(-6.747\kappa^3 - 17.04\kappa^2 + 10.34\kappa - 10.16) + \epsilon_1 (2.6\kappa^3 + 13.64\kappa^2 + 26.8\kappa \right. \\
& \quad \left. - 6.56) + \epsilon_1^2 (1.17\kappa^3 + 14.19\kappa^2 + 13.57\kappa + 8.81) \right] G^2(\underline{\alpha} + \underline{\alpha}^T)
\end{aligned}$$

APPENDIX E

COMPUTER PROGRAMS FOR SOLVING VISCOSITY RATIO

Program Model 1 is for solving shear rate with suspension
model(equations 7.7, 7.8)

```

100=      PROGRAM MODEL1(INPUT,OUTPUT)
110=      DIMENSION XX(500),V(500)
120=      REAL M,N,H
130=C N IS THE POWER LAW INDEX
140=C VSO IS THE POWER LAW PARAMETER, K
150=C PG IS THE PRESSURE GRADIENT
160=C CO IS THE BULK VOID FRACTION
170=C D IS THE CORE THICKNESS
180=C W IS THE WIDTH OF CHANNEL
190=C H IS THE HEIGHT OF CHANNEL
200=C R IS THE BUBBLE RADIUS
210=C BP,BM ARE THE BOUNDARIES OF CONCENTRATION TRANSITION
220=C DY IS THE INCREMENT IN Y DIRECTION
230=C QO IS THE VOLUMETRIC FLOW RATE WITHOUT BUBBLE SUSPENSIONS
240=C X IS THE SHEAR RATE
250=C V IS THE VELOCITY
260=C VOLUME IS THE VOLUMETRIC FLOW RATE WITH BUBBLE SUSPENSION.
270=C
280=      N=.364
290=      B=.278
300=      M=.4
310=1     READ*,PG,CO,D
320=      PRINT*,PG,CO,D
330=      PRINT*,B,M
340=      VSO=36.8
350=      KK=101
360=      VEL=0.
370=      W=3.5*2.54
380=      VOLUME=0.
390=      H=1.27
400=      R=.025
410=      DY=.01
420=      Y=.1
430=      BP=(B+R)*2./H
440=      BM=(B-R)*2./H
450=      QO=2.*W*(PG/VSO)**(1./N)*(H/2.)**((1.+2.*N)*N/(1.+2.*N))
460=      DO 100 I=1,KK
470=      Y=1.-DY*(I-1)
480=      YY=Y*H/2.
490=      X=(PG*YY/VSO)**(1.+N)
500=      IF(Y.LE.BM)GOTO5
510=      IF(Y.LT.BP)GOTO22
520=      GOTO25
530=5     C=CO
540=      CPR=0.
550=      GOTO10
560=22    C=.75*(-(H*Y/2.))**3./3.+D*(H*Y/2.))**2.+(R**2.-D**2.)*(H*Y/2.)
570=      +D**3./3.-R**2.*D-2.*R**3./3.)*(-1./R**3.)
580=      C=CO
590=      CPR=.75*(-(H*Y/2.))**2.+D*H*Y+R**2.-D**2.)*(-1./R**3.)
600=      CPR=CPR*CO
610=      GOTO10

```

```

620=25      C=0.
630=        CPR=0.
640=        GOTO18
650=10      CONTINUE
660=C NEWTON RAPHSON ITERATION OF SHEAR RATE
670=9       XEW=(D*C*X** (H+N)+PG*YY/VSO/(1.+C))** (1./N)
680=        RE=ABS(XEW-X)
690=        IF (RE.LT.1.E-5) GOTO43
700=        X=XEW
710=        GOTO9
720=18      XEW=(PG*YY/VSO)** (1./N)
730=        X=XNEW
740=43      CONTINUE
750=        XX(I)=XEW
760=100     CONTINUE
770=        V(1)=0.
780=        DO 8 I=2, KK
790=        K=I-1
800=        VEL=VEL+XX(K)*DY*H/2.
810=        V(I)=VEL
820=        VOLUME=VOLUME+(V(I)+V(K))/2.*DY*H*W
830=8       CONTINUE
840=        PRINT 60, (V(I), I=1, KK)
850=C EVALUATION OF APPARENT VISCOSITY RATIO
860=        AVSR=QO/VOLUME
870=        PRINT 70, VOLUME, AVSR
880=12      FORMAT(6(E12.6, 2X))
890=40      FORMAT(6X, *Y*, 14X, *X*, 11X, *VISCO*, 11X, *STRESS*, 11X, *C*)
900=50      FORMAT(5(E12.6, 3X))
910=60      FORMAT(10(E12.6, 1X))
920=70      FORMAT(*0*, *FLOW RATE=*, F12.5, 10X, *APP VISCOSITY RATIO=*, F12.5)
930=        STOP
940=        END

```


Program Model 2 is for solving shear rate with suspension model (equations 7.19, 7.20)

```

100=      PROGRAM MODEL2(INPUT,OUTPUT)
110=      DIMENSION A(4),Z(3),XX(500),V(500)
120=      REAL H
140=C VSO IS THE VISCOSITY
150=C PG IS THE PRESSURE GRADIENT
160=C A'S ARE THE COEFFICIENTS OF POLYNOMIAL EQUATION
170=C Z'S ARE THE ROOTS OF THE POLYNOMIAL EQUATION
180=C D IS THE CORE THICKNESS
190=C W IS THE WIDTH OF CHANNEL
200=C H IS THEN HEIGHT OF CHANNEL
210=C R IS THE BUBBLE RADIUS
220=C BP,BM ARE THE BOUNDARIES OF CONCENTRATION TRANSITION
230=C DY IS THE INCREMENT IN Y DIRECTION
240=C QO IS THE VOLUMETRIC FLOW RATE WITHOUT BUBBLE SUSPENSIONS
250=C X IS THE SHEAR RATE
260=C V IS THE VELOCITY
270=C VOLUME IS THE VOLUMETIRC FLOW RATE WITH BUBBLE SUSPENSION.
280=C
290=      A(1)=1.
300=      A(2)=0.
310=1     READ*,PG,CO,D
320=      PRINT*,PG,CO,D
330=      VSO=36.8
340=      KK=101
350=      VEL=0.
360=      W=3.5*2.54
370=      VOLUME=0.
380=      H=1.27
390=      R=.025
400=      DY=.01
410=      Y=.1
420=      BP=(B+R)*2./H
430=      BM=(B-R)*2./H
440=      QO=W*(PG/VSO)*H
450=      DO 100 I=1,KK
460=      Y=1.-DY*(I-1)
470=      YY=Y*H/2.
480=      X=(PG*YY/VSO)**(1.+N)
490=      IF(Y.LE.BM)GOTO5
500=      IF(Y.LT.BP)GOTO22
510=      GOTO25
520=5     C=CO
530=      CPR=0.
540=      GOTO10
550=22    C=.75*(-(H*Y/2.))**3./3.+D*(H*Y/2.))**2.+(R**2.-D**2.)*(H*Y/2.)
560=      ++D**3./3.-R**2.*D-2.*R**3./3.)*(-1./R**3.)
570=      C=CO
580=      CPR=.75*(-(H*Y/2.))**2.+D*H*Y+R**2.-D**2.)*(-1./R**3.)
590=      CPR=CPR*CO
600=      GOTO10

```

```

610=25      C=0.
620=        CPR=0.
630=        GOTO18
640=10      CONTINUE
650=C SOLVE FOR SHEAR RATE
660=        A(3)=(-1.*C0*C)/(D*(2.*PG/(8.*H*VSO))**2.*C0*C)
670=        A(4)=(-PG*H*Y/(VSO*2.)/(D*(2.*PG/(8.*H*VSO))**3.*C0*C)
680=C ZPOLR IS THE INSL SUBROUTINE FOR SOLVING ROOTS OF THE NTH ORDER
690=C POLYNOMIAL EQUATION
700=        CALL ZPOLR(A,NDEG,Z,IER)
710=        PRINT 12,(Z(J),J=1,3)
720=        XEW=Z(3)
730=        GOTO43
740=18      XEW=PG*Y*VSO
750=        X=XNEW
760=43      CONTINUE
770=        XX(I)=XEW
780=100     CONTINUE
790=        V(1)=0.
800=        DO 8 I=2,KK
810=        K=I-1
820=        VEL=VEL+XX(K)*DY*H/2.
830=        V(I)=VEL
840=        VOLUME=VOLUME+(V(I)+V(K))/2.*DY*H*W
850=8       CONTINUE
860=        PRINT 60,(V(I),I=1,KK)
870=C EVALUATION OF APPARENT VISCOSITY RATIO
880=        AVSR=Q0/VOLUME
890=        PRINT 70,VOLUME,AVSR
900=12      FORMAT(6(E12.6,2X))
910=40      FORMAT(6X,*Y*,14X,*X*,11X,*VISCO*,11X,*STRESS*,11X,*C*)
920=50      FORMAT(5(E12.6,3X))
930=60      FORMAT(10(E12.6,1X))
940=70      FORMAT(*0*,*FLOW RATE=*,F12.5,10X,*APP VISCOSITY RATIO=*,F12.5)
950=        STOP
960=        END

```

LIST OF REFERENCES

LIST OF REFERENCES

- Adams, F., and R. Dams, "Applied Gamma-Ray Spectrometry," Pergamon Press, 1970.
- Barthes-Biesel, D., and A. Acrivos, "The Rheology of Suspensions and Its Relation to Phenomenological Theories for Non-Newtonian Fluids," Intern. J. Multiphase Flow, 1, 1-24 (1973).
- Batchelor, G. K., "The Stress System in a Suspension of Force-Free Particles," J. Fluid Mech., 41, 545-570 (1970).
- Batchelor, G. K., "The Stress Generated in a Non-Dilute Suspension of Elongated Particles by Pure Strain Motion," J. Fluid Mech., 46, 813-829 (1971).
- Batchelor, G. K., and J. T. Green, "The Determination of the Bulk Stress in a Suspension of Spherical Particles to Order C^2 ," J. Fluid Mech., 56, 401-427 (1972).
- Bigg, D. M., and P. R. Preston, "An Experimental Technique for Predicting Foam Processability and Physical Properties," Polym. Eng. & Sci., 16(10), 706-711 (1976).
- Blyler, L. L., Jr., and T. K. Lwei, "Flow Behavior of Polyethylene Melts Containing Dissolved Gases," J. Poly. Sci., 35, 165-176 (1971).
- Boger, D. V., and H. Nguyen, "A Model Viscoelastic Fluid," Polym. Eng. & Sci., 18(13), 1037-1043 (1978).
- Brenner, H., "The Stokes Resistance of a Slightly Deformed Sphere," Chem. Eng. Sci., 19, 519-540 (1964a).
- Brenner, H., "Coupling Between the Translational and Rotational Brownian Motions of Rigid Particles of Arbitrary Shape: II. General Theory." J. Colloid. Interf. Sci., 23, 407-436 (1967).
- Brenner, H., "Suspension Rheology," Prog. in Heat and Mass Trans., 5, 89-129 (1972).

- Brenner, H., "Rheology of a Dilute Suspension of Axisymmetric Brownian Particles," Intern. J. Multiphase Flow, 1, 195-341 (1974).
- Brunn, P., "Interaction of Spheres in a Viscoelastic Fluid," Rheol. Acta, 16(5), 461-475 (1977).
- Brunn, P., "The Motion of a Slightly Deformed Sphere in a Viscoelastic Fluid," Rheol. Acta, 18, 229-243 (1979).
- Caswell, B., and W. H. Schwarz, "The Creeping Motion of a Non-Newtonian Fluid Past a Sphere," J. Fluid Mech., 13, 417-426 (1962).
- Caswell, B., "The Effect of Finite Boundaries on the Motion of Particles in Non-Newtonian Fluids," Chem. Eng. Sci., 25, 1167-1176 (1970).
- Caswell, B., "Sedimentation of Particles in Non-Newtonian Liquids," The Mechanics of Viscoelastic Fluids, Appl. Mech. Div., 22 ASME, (1977).
- Chan, P. C. H., and L. G. Leal, "The Motion of a Deformable Drop in a Second-Order Fluid," J. Fluid Mech., 92, part 1, 131-170 (1979).
- Chan, P. C. H., and L. G. Leal, "Experimental Study of Drop Migration in Shear Flow Between Concentric Cylinders," Intern. J. Multiphase Flow, 7, 83-89 (1981).
- Chhabra, R. P., P. H. T. Uhlherr, and Boger, D. V., "The Influence of Fluid Elasticity on the Drag Coefficient for Creeping Flow Around a Sphere," J. Non-Newtonian Fluid Mech., 6, 187-199 (1980).
- Chin, H. B., and C. D. Han, "Droplet Deformation," Trans. Soc. Rheol., 23, 557-590 (1979).
- Choi, S. J., and W. R. Schowalter, "Rheological Properties of Non-Dilute Suspensions of Deformable Particles," Phy. of Fluid, 18(4), 420-427 (1975).
- Cox, R. G., "The Deformation of a Drop in a General Time Dependent Fluid Flow," J. Fluid Mech., 37, 601-623 (1969).
- Einstein, A., Eine Neue Bestimmung der Molekuldimensionen, Ann. Physik 34, 591-592 (1911). Errata: Ann. Physik 34, 591-592 (1911).

- Fogler, H. S., and J. D. Goddard, "Collapse of Spherical Cavities in Viscoelastic Fluids," *Phy. of Fluid*, 13 (5), 1135-1141 (1970).
- Frankel, N. A., and A. Acrivos, "On the Viscosity of a Concentrated Suspension of Solid Spheres," *Chem. Eng. Sci.*, 22, 847-853 (1967).
- Frankel, N. A., and A. Acrivos, "The Constitutive Equation for a Dilute Emulsion," *J. Fluid Mech.*, 44, 65-78, (1970).
- Gauthier, F., H. L. Goldsmith, and S. G. Mason, "Particle Motions in Non-Newtonian Media I," *Rheol. Acta*, 10, 344-364 (1971).
- Gauthier, F., H. L. Goldsmith, and S. G. Mason, "Particle Motions in Non-Newtonian Media II," *Trans. Soc. Rheol.*, 15, 297-330 (1971).
- Gieskus, V. H., "Die Simultane Translations - und Rotationsbewegung Einer Kugel in Einer Elastoviskosen Flussigkeit," *Rheol. Acta*, 3, 59-71 (1962).
- Goddard, J. D., and C. Miller, "Nonlinear Effects in the Rheology of Dilute Suspensions," *J. Fluid Mech.*, 28, 657-673 (1967).
- Goddard, J. D., "An Elastohydrodynamic Theory for the Rheology of Concentrated Suspensions of Deformable Particles," *J. Non-Newtonian Fluid Mech.*, 2, 169-189 (1977).
- Han, C. D., and R. G. King, "Measurement of the Rheological Properties of Concentrated Emulsions," *Trans. Soc. Rheol.*, 24(2), 213-237 (1980).
- Happel, J., and H. Brenner, Low Reynolds Number Hydrodynamics, Prentice-Hall, Englewood Cliffs, NJ. (1965).
- Highgate, D. J., and R. W. Whorlow, "End Effects and Particle Migration Effects on Concentric Cylinder Rheometry," *Rheol. Acta*, 8, 142-151 (1969).
- Highgate, D. J., and R. W. Whorlow, "Rheological Properties of Suspensions of Spheres in Non-Newtonian Media," *Rheol. Acta*, 9, 569-576 (1970).
- Ho, B. P., and L. G. Leal, "Inertia Migration of Rigid Spheres in Two-Dimensional Unidirectional Flows," *J. Fluid Mech.*, 65, 365-400 (1974).

- Hoffman, R. L., "Discontinuous and Dilatant Viscosity Behavior in Concentrated Suspensions II, Observation of a Flow Instability," *Trans. Soc. Rheol.*, 16, 155-173 (1972).
- Hoffman, R. L., "Discontinuous and Dilatant Viscosity Behavior in Concentrated Suspensions II," *J. Colloid and Interf. Sci.*, 46, 491-506 (1974).
- Hooker, H. H., and G. F. Popper, "A Gamma-Ray Attenuation Method for Void Fraction Determination in Experimental Boiling Heat Transfer Test Facilities," ANL-5766, No. (1958).
- Jeffrey, D. J., and A. Acrivos, "The Rheological Properties of Suspensions of Rigid Particles," *AIChE J.* 22, 417-432 (1976).
- Karnis, A., and S. G. Mason, "Particle Motions in a Sheared Suspensions XIX Viscoelastic Media," *Trans. Soc. Rheol.*, 10, 571-592 (1966).
- Kataoka, T., T. Kitano, M. Sasahara, and K. Nishijima, "Viscosity of Particle Filled Polymer Melts," *Rheol. Acta*, 17, 149-155 (1978).
- Krieger, I. M., and M. Eguiluz, "The Second Electroviscous Effect in Polymer Latices," *Trans. Soc. Rheol.*, 20, 29-45 (1976).
- Landau, L. D., and E. M. Lifshitz, Fluid Mechanics, Addison-Wesley, Reading, MA, 1959.
- Leal, L. G., "Slow Motion of Slender Rod-Like Particles in a Second Order Fluid," *J. Fluid Mech.*, 69(2), 305-377 (1975).
- Leslie, F. M., and R. Z. Tanner, "Slow Flow of Visco-Elastic Liquid Past Sphere," 14, pt1, 36-48 (1961).
- Lin, C. J., J. H. Perry, and W. R. Schowalter, "Simple Shear Flow Round a Rigid Sphere: Inertial Effects and Suspension Rheology," *J. Fluid Mech.*, 44, 1-17 (1970).
- Mastumoto, T., O. Yamamoto, and S. Onagi, "Rheological Properties of Disperse Systems of Spherical Particles in Polystyrene Solution at Long Time Scales," *Trans. Soc. Rheol.*, 19, 541-55 (1975).
- Metzner, A. B., and M. Whitlock, "Flow Behavior of Concentrated (Dilatant) Suspensions," *Trans. Soc. Rheol.*, 2, 239-245, (1958).

- Michele, J., R. Patzold, and R. Donis, "Alignment and Aggregation Effects in Suspensions of Spheres in Non-Newtonian Media," *Rheol. Acta*, 16, 317-321 (1977).
- Middleman, S., Fundamentals of Polymer Processing, McGraw-Hill, 1977.
- Oyanagi, Y., and J. L. White, "Basic Study of Extrusion of Polyethylene and Polystyrene Foams," *J. App. Poly. Sci.*, 23, 1013-1026 (1979).
- Patrick, M., and B. S. Swanson, "Radiation Attenuation Method of Measuring Density of a Two-Phase Fluid," *Rev. Sci. Instr.*, 29 (12), 1079-1085 (1958).
- Pearson, G., and S. Middleman, "Elongational Flow Behavior of Viscoelastic Liquids, Part I. Modeling of Bubble Collapse," *AIChE*, 23(5), 712-726 (1977).
- Pearson, G., and S. Middleman, "Elongational Flow Behavior of Viscoelastic Liquids: Modeling Bubble Dynamics With Viscoelastic Constitutive Relations," *Rheol. Acta*, 17, 500-510 (1978).
- Peery, J. H., "Fluid Mechanics of Rigid and Deformable Particles in Shear Flow at Low Reynolds Numbers," Ph.D. Thesis, Princeton University, (1966).
- Prud'homme, R. K., and R. B. Bird, "The Dilatational Properties of Suspensions of Gas Bubbles in Incompressible Newtonian and Non-Newtonian Fluids," *J. Non-Newtonian Fluid Mech.*, 3, 261-279 (1977/78).
- Prud'homme, R. K., "The Flow of Non-Dilute Suspensions of Gas Bubbles in Non-Newtonian Fluids," Ph.D. Thesis, University of Wisconsin, Madison (1978).
- Quemada, D., "Rheology of Concentrated Disperse Systems and Minimum Energy Dissipation Principles," *Rheol. Acta*, 16, 82-94 (1977).
- Rivlin, R. S. and J. L. Ericksen, "J. Rational Mech. and Anal.", 4, 350-362, (1955).
- Roscoe, R., "On the Rheology of a Suspension of Visco-Elastic Spheres in a Viscous Liquid," *J. Fluid Mech.*, 28, 273-293 (1967).
- Russell, W. R., "Low Shear Limit of the Second Electroviscous Effect," *J. Colloid Interf. Sci.*, 55, 590-604 (1976).

- Saffman, P. G., "On the Motion of Small Spheroidal Particles in a Viscous Liquid," J. Fluid Mech., 1, 554-553 (1956).
- Sigli, D. and M. Coutanceau, "Effect of Finite Boundaries on the Slow Laminar Isothermal Flow of a Viscoelastic Fluid Around a Sphere Obstacle" J. Non-Newtonian Fluid Mech., 2, 1-21 (1977).
- Schowalter, W. R., C. E. Chaffey, and H. Brenner, "Rheological Behavior of a Dilute Emulsion," J. Colloid and Interf. Sci., 26, 152-160 (1968).
- Schowalter, W. R., Mechanics of Non-Newtonian Fluids, A.P., New York, (1978).
- Schrock, V. E., "Radiation Attenuation Techniques in Two-Phase Flow Measurement," 11th National ASME/AIChE Heat Transfer Conference, Aug., Minneapolis, Minnesota, (1969).
- Segre, G., and A. Silberberg, "Behavior of Macroscopic Rigid Spheres in Poiseuille Flow," J. Fluid Mech., 14, 115-135 (1962).
- Street, J. R., "The Rheology of Phase Growth in Elastic Liquids," Trans. Soc. Rheol., 12, 103-131 (1968).
- Street, J. R., A. L. Fricke, and L. P. Reiss, "Dynamics of Phase Growth in Viscous, Non-Newtonian Liquids," I & EC, Fund., 10(1), 54-64 (1971).
- Tozeren, A. and R. Skalak, "Stress in a Suspension Near Rigid Boundaries," J. Fluid Mech., 82, 289-307 (1977).
- Vader, F. V., and H. Dekker, "Measurement of Polymer Bridging Forces in Liquid-Liquid Systems," J. Colloid Interf. Sci., 83, 377-383 (1981).
- Villamizar, C. A., and C. D. Han, "Study of Structural Form Processing: II. Bubble Dynamics in Foam Injection Molding," Polym. Eng. & Sci., 18, 699-710 (1978).
- Wade, R. C., and C. Letendre, "Foaming Epoxy Resins and PVC Plastics with Sodium Borohydride Blowing Agent," J. of Cellular Plastics, Jan/Feb, 1980, 132-35.
- Wagner, M. G., and J. C. Slattery, "Slow Flow of a Non-Newtonian Fluid Past a Droplet," AIChE, 17(5), 1198-1207 (1971).

- Yang, W. J., and H. C. Yeh, "Theoretical Study of Bubble Dynamics in Purely Viscous Fluid," *AIChE J.*, 12, 927-931 (1966).
- Zana, E., and L. G. Leal, "Dissolution of a Stationary Gas Bubble in a Quiescent Visco-Elastic Liquid," *I & EC Fund.*, 14(3), 175-182 (1975).
- Zana, E., and L. G. Leal, "The Dynamics and Dissolution of Gas Bubbles in a Viscoelastic Fluid," *Intern. J. Multiphase Flow*, 4, 237-262 (1978).

MICHIGAN STATE UNIVERSITY LIBRARIES



3 1293 03146 1985